RELATIVE DAMAGING ABILITY OF GALACTIC COSMIC RAYS DETERMINED USING MONTE CARLO SIMULATIONS OF TRACK STRUCTURE

A Dissertation

by

BRADLEY WILLIAM COX

Submitted to the Office of Graduate Studies of
Texas A&M University
in partial fulfillment of the requirements for the degree of

DOCTOR OF PHILOSOPHY

August 2011

Major Subject: Nuclear Engineering

Relative Damaging Ability of Galactic Cosmic Rays Determined Using Monte Carlo

Simulations of Track Structure

RELATIVE DAMAGING ABILITY OF GALACTIC COSMIC RAYS

DETERMINED USING MONTE CARLO SIMULATIONS OF

TRACK STRUCTURE

A Dissertation

by

BRADLEY WILLIAM COX

Submitted to the Office of Graduate Studies of
Texas A&M University
in partial fulfillment of the requirements for the degree of

DOCTOR OF PHILOSOPHY

Approved by:

Co-Chairs of Committee,	Leslie A. Braby
	Stephen Guetersloh
Committee Members,	John Ford
	John W. Poston, Sr.
	Nancy Turner
Head of Department,	Raymond Juzaitis

August 2011

Major Subject: Nuclear Engineering

ABSTRACT

Relative Damaging Ability of Galactic Cosmic Rays Determined Using Monte Carlo Simulations of Track Structure. (August 2011)

Bradley William Cox, B.S., University of Texas

Co-Chairs of Advisory Committee: Dr. Leslie A. Braby
Dr. Stephen Guetersloh

The energy deposition characteristics of heavy ions vary substantially compared to those of photons. Many radiation biology studies have compared the damaging effects of different types of radiation to establish relative biological effectiveness among them. These studies are dependent on cell type, biological endpoint, radiation type, dose, and dose rate. The radiation field found in space is much more complicated than that simulated in most experiments, both from a point of dose-rate as well as the highly mixed field of radiative particles encompassing a broad spectrum of energies. To establish better estimates for radiation risks on long-term, deep space missions, the damaging ability of heavy ions requires further understanding. Track structure studies provide significant details about the spatial distribution of energy deposition events in and around the sensitive targets of a mammalian cell. The damage imparted by one heavy ion relative to another can be established by modeling the track structures of ions that make up the galactic cosmic ray (GCR) spectrum and emphasizing biologically relevant target geometries.

This research was undertaken to provide a better understanding of the damaging ability of GCR at the cellular level. By comparing ions with equal stopping power values, the differences in track structure will illuminate variations in cell particle traversals and ionization density within cell nuclei. For a cellular target, increased particle traversals, along with increased ionization density, are key identifiers for increased damaging ability.

Performing Monte Carlo simulations with the computer code, FLUKA, this research will provide cellular dosimetry data and detail the track structure of the ions. As shown in radiobiology studies, increased ionizations within a cell nucleus generally lead to increased DNA breaks and increased free radical production, resulting in increased carcinogenesis and cell death. The spatial distribution of dose surrounding ions' tracks are compared for inter- and intracellular regions. A comparison can be made for many different ions based upon dose and particle fluence across those different regions to predict relative damaging ability. This information can be used to improve estimates for radiation quality and dose equivalent from the space radiation environment.

DEDICATION

This dissertation is dedicated to my family and friends for their unwavering support during the last four years of my graduate program. Thank you for helping to make this a wonderful experience for me.

ACKNOWLEDGEMENTS

I would like to thank the U.S. Department of Veterans Affairs for the continual financial support over my entire four years in graduate school.

I would like to thank the National Space Biomedical Research Institute's Space Life Sciences program for financial support and for introducing me into the space radiation biology community. The internship at Johnson Space Center and NASA Space Radiation Summer School were invaluable experiences.

Finally, I would like to thank my advisory committee for their guidance and the knowledge they've passed on to me.

NOMENCLATURE

GCR	Galactic Cosmic Ray
SPE	Solar Particle Event
LET	Linear Energy Transfer
LEO	Low Earth Orbit
DSB	Double (DNA) Strand Break
SSB	Single (DNA) Strand Break
ISS	International Space Station

TABLE OF CONTENTS

LIST OF FIGURES

FIGURE Page

FIGURE Page

LIST OF TABLES

CHAPTER I

INTRODUCTION

Galactic cosmic rays (GCR) pose a substantial health risk to astronauts in space. The primary risk of interest in space radiation biology studies is an increased chance of cancer induction later in life. Uncertainties in risk estimates, caused by the interaction of GCR in human tissue, stem primarily from uncertainties in radiation quality factors (NCRP 2006). Dose equivalent, calculated using a quality factor, is not specific enough to predict the differences in damaging ability of the components of the GCR spectrum. The ICRP notes the uncertainties involved by emphasizing that the quality factor and individual tissue weighting factors are designed for general radiation protection practices and serve only as rough indicators of risk, not actual risk assessment (ICRP 2003). The generally accepted methods for determining quality factor do not account for differences in particle tracks of different ions with equal linear energy transfer (LET). The LET can be equal for different particle species with different velocities, but radiobiological studies often indicate differing levels of damaging ability.

This research is designed to provide better estimates for the biological risks of GCR by improving the knowledge of the energy deposited in cell nuclei by GCR particle tracks. The damaging ability of an ion will be established relative to that of other ions of the GCR spectrum by comparing their particle tracks in a water medium.

This dissertation follows the style of Health Physics.

Variations in the particle trajectories of different ions cause a change in the spatial distribution of energy depositions in a target. Transport modeling that accounts for all processes along the path of the ion, rather than electromagnetic energy loss alone, will be used. This is performed by computational modeling using FLUKA. This Monte Carlo simulation approach details specific energy deposition events, while well-accepted theoretical methods, including amorphous track modeling, are used as a baseline for overall comparison. Detailed study of individual events is necessary because target effects are based on the spatial distribution of energy deposition events relevant to strand breaks and clustering instead of overall averaging. The effects of different ions can be compared as a function of atomic number (Z) and kinetic energy (MeV n^{-1}). This research takes two approaches:

1. Compare the track structure of different ions having equal stopping power, and
2. Compare the track structure of different ions having equal velocity.

In the first case, ions have different velocities but lose energy at the same rate when traversing a thin target. In this case, variations in track structure are due to the spatial distribution of energy imparted in small volumes within the total volume and are largely a function of primary particle velocities. The ions with higher velocity produce higher-energy secondary electrons that travel farther from the primary track. They affect a much larger number of targets via secondary electron tracks. The ions with lower velocity affect fewer targets but deposit higher dose near the center of the track.

For the second case, spatial distributions of energy imparted in small volumes will be similar because the knock-on collision process will produce a spectrum of delta rays with similar kinetic energy spectra. In this case, the number of delta rays produced will be less for lower Z ions, meaning the total energy deposited is also less. It is the goal of this project to determine how these variations in energy deposition will affect targets on the cellular scale.

CHAPTER II

BACKGROUND

Space Radiation Environment

Radiation dose received by astronauts on missions to space is a major topic of concern for planning future missions. During low-Earth orbit (LEO) missions, such as those conducted on the International Space Station (ISS) and Space Transport Shuttles, crews are exposed to GCR, solar particle events (SPE), and the protons and electrons that make up the Van Allen belts. The Earth's magnetosphere provides a high level of shielding from GCR and SPE by deflecting and fragmenting ions, offering some protection for astronauts in LEO. As one travels away from the Earth, radiation levels increase as the atmosphere and magnetosphere dissipate. Were a mission to travel beyond LEO, GCR and SPE become a greater concern, due to higher abundance of these particles. Dose rates are estimated to increase by a factor of two for deep space missions compared to LEO missions (NCRP 2006). As humankind looks to extend missions deeper into space, such as a manned mission to Mars, radiation levels become a significant concern for health risks. GCR and SPE are the focal point for radiation-induced cancer and risk estimates must be improved. To properly estimate radiation risk, detailed knowledge of the composition and energy spectra of GCR must be understood. Risk estimates currently in use are described in NCRP Report 132 (NCRP 2000) and pertain only to LEO. NCRP Report 153, <u>Information needed to make</u>

radiation protection recommendations for space missions beyond low-earth orbit (NCRP 2006), is intended to provide further guidance to include long term, deep space missions.

The GCR spectrum consists of heavy ions with a broad range of kinetic energy and penetrating ability. These ions traverse the spacecraft and human body, creating a complicated field of secondary radiations. Radiation dose received from GCR is associated with a large uncertainty, due to complicated interactions in target and shielding materials. Resulting biological effects from these complicated particle tracks pose additional uncertainties. Radiation shielding is mostly provided by the aluminum hull of the spacecraft, and its shallow thickness serves only to reduce the low-energy particle fluence. Mission cost is highly dependent on the amount of mass that is needed to be put into space. As a result, the amount of radiation shielding required to eliminate radiation exposure surpasses what is reasonably achievable for a mission. Rather than relying completely on shielding, improving radiation dose assessment techniques should prove to be an effective method for improving dose-risk assessment.

The GCR spectrum consists of many different charged particles, from protons to uranium, with energies from 10 MeV n^{-1} to 10^{12} MeV n^{-1} (NCRP 2006). Their abundances peak with kinetic energies of 300 – 700 MeV n^{-1}, and ions heavier than iron are of such low abundance that they are usually ignored for personnel dosimetry. Particle fluence and kinetic energy are important in determining radiation dose, and Table 1 provides a relation across the GCR spectrum.

Table 1. Relative GCR abundance at several kinetic energies. Ion abundance is presented relative to Si-28 which is set arbitrarily to 1000 (NCRP 2006). Ions shaded in blue are the object of study in this research.

Z	Element	0.2 Gev n^{-1}	1 GeV n^{-1}	5 GeV n^{-1}
1	H	2200000	2800000	4600000
2	He	340000	250000	230000
3	Li	1000	1400	960
4	Be	450	730	680
5	B	2100	2340	1600
6	C	8500	7100	6460
7	N	1940	2000	1610
8	O	7770	6430	6190
9	F	183	145	115
10	Ne	1120	1050	960
11	Na	273	224	188
12	Mg	1430	1330	1260
13	Al	252	229	207
14	Si	1000	1000	1000
15	P	40	47	37
16	S	164	206	190
17	Cl	36	45	37
18	Ar	63	90	68
19	K	51	66	51
20	Ca	135	147	119
21	Sc	29	33	22
22	Ti	107	98	74
23	V	57	44	38
24	Cr	109	98	83
25	Mn	72	55	56
26	Fe	602	607	685
27	Co	2	3	4
28	Ni	29	27	36

The radiations of interest in this research are the GCR that present a mostly constant exposure of charged particles, making up a spectrum comprised mainly of protons (87%), helium (12%), and HZE particles (1%) (Ballarini et al. 2008). To specifically study the effects of track structure of these ions, those highlighted in blue in Table 1 were chosen for an in-depth dosimetry analysis. The relative abundance of different ions and energies varies as the solar activity modulates the GCR field. The solar wind blows radially outward, and at its maximum, creates a GCR minimum. It is more effective in reducing the fluence of the lower-energy GCR, which are also of higher abundance. The solar cycle lasts, on average, about 11 years (Cucinotta et al. 2001).

Solar particle events are a second source of radiation risk for long-term deep space missions. Although SPE that are strong enough to present a serious risk are very unlikely; increasing mission duration increases the chance of experiencing one. The ion spectrum of an SPE consists primarily of protons and to a lesser extent, helium. There is a small portion of higher Z ions associated with most events, but these are of such small abundance compared to GCR that they have little impact on radiation dose. The vast majority of protons and helium ions are low enough in energy that they are stopped by the walls of the spacecraft before they reach an astronaut inside the ship. Risks pertain to an astronaut working outside the ship on extravehicular activity or on the surface of the Moon. Much of the work going into protection from SPE lies in prediction capabilities. If these events can be predicted with adequate short warning, the astronaut may have enough forewarning to plan to return to shelter before the SPE arrives. Due to the rigorous work schedule on most missions, forecasting the conclusion of SPE is also valuable, because it allows crewmembers advanced notice of when they would be able to return to work outside the spacecraft or shelter.

General radiation-protection practices utilize the factors of time, distance, and shielding to reduce radiation dose from external sources. Concerning GCR, exposure time is dependent on the mission, distance is not applicable, and the amount of shielding that can be carried to space is too minimal to significantly reduce the dose. To make accurate risk estimates, knowledge of the radiation field must be well understood. Effects due to GCR over long-term, deep space missions, are accompanied by a large source of uncertainty due to the interaction of the heavy ions with the spacecraft and other materials that significantly change and complicate the radiation spectrum. To analyze the impact of space radiation on a biological system, it is necessary to create models of the interactions of the radiation with shielding and target materials. Heavy ions with considerable kinetic energy create secondary particles from interactions while traversing a medium. Secondary radiations consist largely of photons, electrons, neutrons, and positively charged ion fragments that complicate a dose equivalent calculation. Fragments tend to retain a velocity similar to their parent giving them a much lower stopping power and a longer range. Target atoms can fragment as well, and these ions generally have very low velocity, very high stopping power, and very short range. The location of the astronaut, in conjunction with the variations in spacecraft walls and objects within the vessel impose additional difficulties in determining a realistic radiation field incident on an astronaut. The result is a radiation field inside the spacecraft that is quite different from the one outside it. Fragmentation of GCR leads to a broader spread of secondary particles that will interact with more targets. These secondaries will have decreased cumulative stopping power but may interact with more cells in the human body, increasing risks. Secondary fragments also have longer ranges, reducing shielding effectiveness.

As these particles traverse cell nuclei only sporadically and generally with intervals between hits of a day or longer, averaged values are meaningless (Curtis et al. 1995). Focusing on the heavier ions, cells will only receive one particle traversal every few weeks. This significantly changes the energy deposition patterns concerning LET and relative biological effectiveness (RBE). The occasional heavy ion traversal experienced by a cell is significant because the RBE of heavy ions is generally greater than 1. These values will be discussed in depth in the next section. The GCR included in this research were chosen based on the measured relative abundance and provides a broad range of atomic numbers and kinetic energies. These particles interact with spacecraft materials and the human body to create a much more complicated radiation environment, producing nearly all radiative particles through electromagnetic and nuclear interactions.

NASA policy specifies the maximum allowable risk, caused by GCR related health effects, as a 3 percent increase in developing a fatal cancer due to radiation exposure on a space mission. The risk is established by combining dose and dose-rate estimates with radiation quality. A crewmember on ISS typically receives from 0.5 – 1.2 mSv day^{-1} (NCRP 2006). Approximately 75% is from GCR and 25% from protons encountered in passages through the South Atlantic Anomaly regions of the Van Allan belts. When a mission leaves the Earth's magnetosphere, the dose is expected to roughly double, with a larger portion coming from heavy ions. For a six-month transit to Mars, effective doses as large as 1 Sv have been estimated from GCR. Absorbed doses and dose equivalents calculated using the current generation transport codes claim uncertainties under 25% (NCRP 2006). Uncertainty in the biological consequences of dose rate has been found to contribute about 40% of the uncertainty in radiation risk estimates although higher LET radiation exhibit decreased dose rate dependence for biological endpoints (Cucinotta et al. 2001). The improvement of radiation protection requires better knowledge of the space radiation field inside the spacecraft, interaction events in shielding and target materials, and biological endpoints based on the known radiation exposures. Much of the uncertainty in risk estimates stem from the unknown relationship between RBE and particle charge and velocity.

Dose and Risk Assessment

Radiation risk estimates are established for most types of radiation, but large uncertainties exist. Heavy ions impart their kinetic energy by densely ionizing tracks – much differently than sparsely ionizing electron tracks produced by photon radiation. This difference is accounted for in dose equivalent calculations using weighting functions that vary by radiation type and tissue type. These weighting factors are derived from the developing knowledge of biophysics and radiobiology and depend on both experimental and epidemiological data. Irradiation characteristics such as dose rate, radiation quality, and target types are the driving forces that determine weighting factors. The ICRP states that radiation weighting factors (w_r) are designed for the practice of radiological protection, and are not intended for specific risk assessment (ICRP 2003). The radiation weighting factor depends on the radiation type and its kinetic energy. It is strongly based on RBE data and is intended to represent stochastic effects following low doses. It must reflect an entire range of LET values for a particle and its secondaries.

Absorbed dose is an average value of the amount of energy deposited in a volume of material by radiation. Dose equivalent is a product of absorbed dose and a radiation quality factor (Q) and predicts the biological damaging ability. Effective dose equivalent is the product of dose equivalent and a tissue weighting factor to describe risk, specifically, to a tissue or organ. This research focuses on radiation quality and the uncertainties it generates for the dose equivalent value. Radiation weighting factor does not account for differences in LET, particle charge, or particle velocity. Quality factor is based on the LET of a radiation, providing detail for radiation protection over a broad range of LET values.

Ions in the GCR spectrum cover a very broad range of LET values. Q varies as a function of the unrestricted LET, representing an average energy lost by a particle as it traverses thin slices of target depth, strongly determined by particle charge and velocity. Unrestricted LET accounts for all energy deposited by a particle, as opposed to the restricted LET that uses a cut-off distance to neglect secondary-energy depositions that occur far away from the primary track. This method provides better analysis than the single value given by w_r. Figure 1 describes how Q varies with increasing LET, reaches a maximum at 100 keV μm^{-1}, and then drops off at higher LET values. The Q value is intentionally biased to be conservative when uncertainty exists in the data.

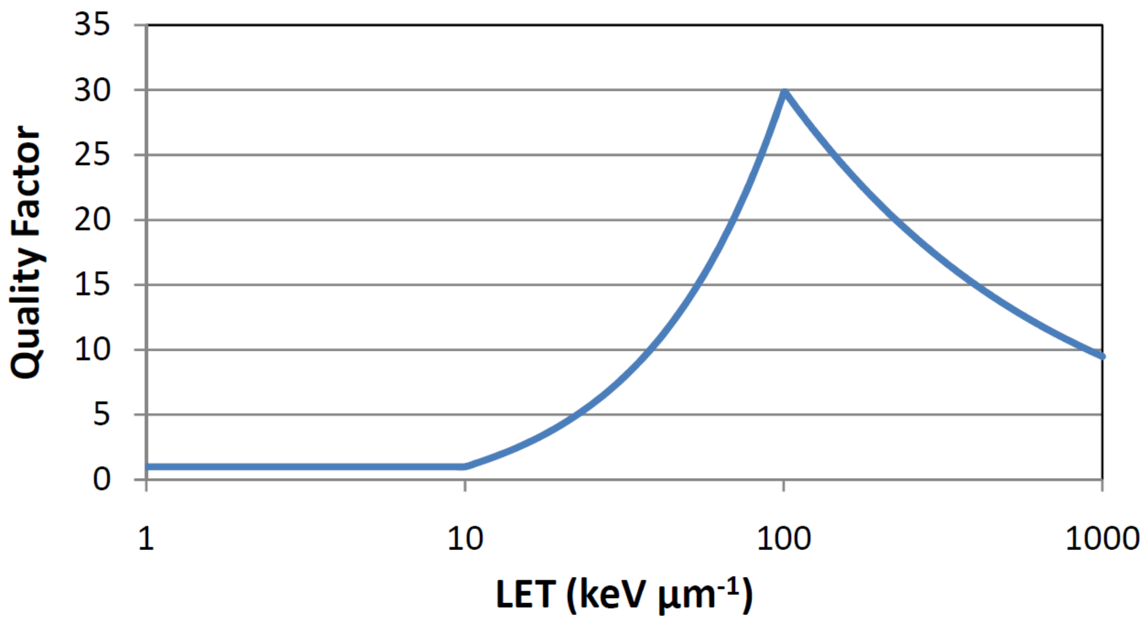

Figure 1. Radiation quality factor as a function of LET (ICRP 2003).

The reason Q drops off at very high LET is that such densely ionizing radiation tends to kill mammalian cells. This overkill effect increases the chance of experiencing acute radiation effects where non-surviving cells do not become cancerous.

Quality factor is roughly related to the RBE of a radiation, often related to LET. RBE can be studied as a function of stochastic or deterministic effects. It is a ratio of two absorbed doses of two different types of radiation that produce the same effect. For example, if twice as much radiation dose is required by radiation A to kill as many cells as radiation B, then the RBE of radiation B is 2 in regard to radiation A. Radiation A is generally a reference radiation of Co-60 or Cs-137 gamma or 250 kV x-rays. Cell-kill is associated with short-term, deterministic effects, while the yield of chromosome aberrations is often assumed to be associated with cell survival and stochastic, cancer risks. In radiobiology experiments, RBE can be designated to describe a variety of biological endpoints. RBE commonly describes the population of surviving cells following radiation exposure. RBE can also be used to describe other target effects, such as the population of chromosome aberrations present in cellular targets following irradiation. Figure 2 displays RBE as a function of LET for several different biological endpoints.

The trends in Figure 2 represent how experimental radiobiology data was used in the development of the Q vs. LET relationship. RBE for heavy ions tends to be largest at low dose; the relevant values are termed RBE_M (ICRP 2003). The RBE_M is the ratio of the initial slopes of the dose-effect curves between a radiation of study and a reference radiation. It describes the limit values where the RBE reaches low doses and effects become more difficult to identify. RBE_M was established to provide a baseline comparison between experiments using different absorbed doses and dose rates.

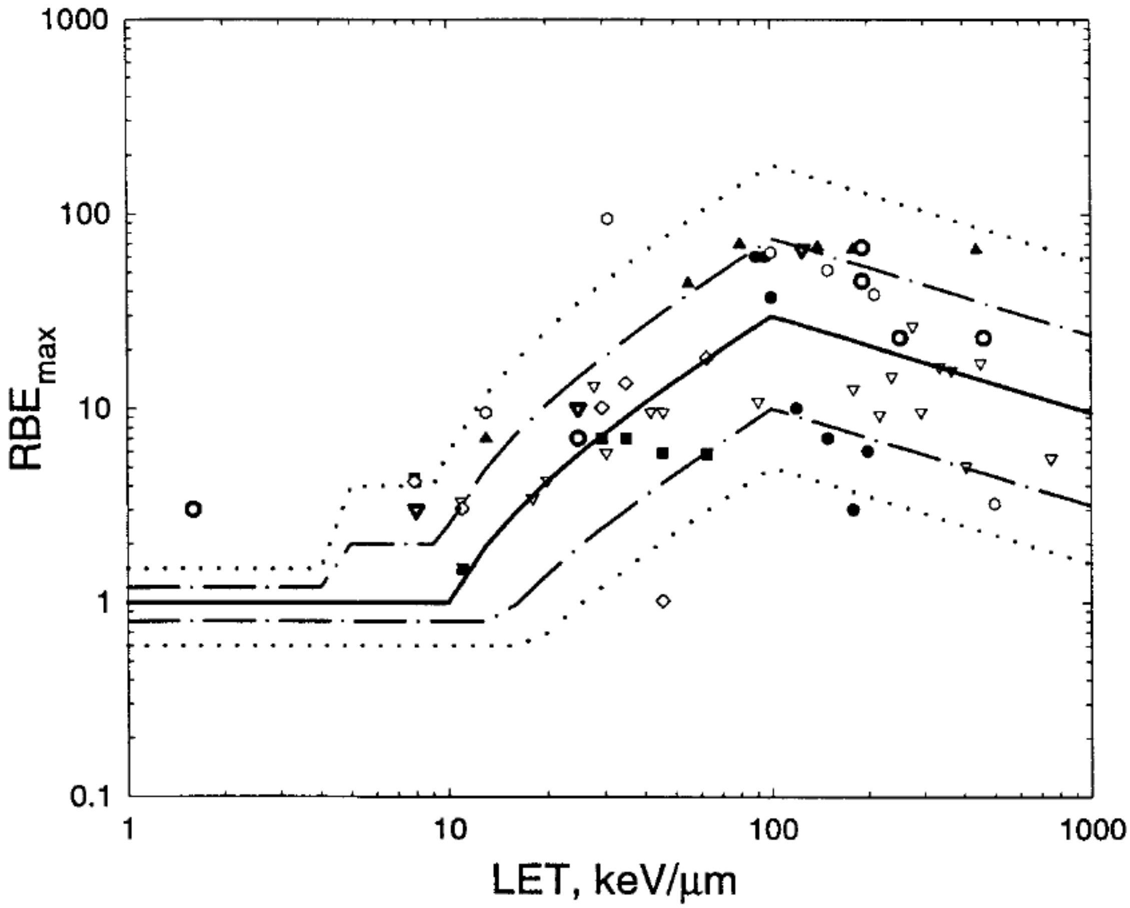

Figure 2. RBE as a function of LET for various biological targets and endpoints (Cucinotta et al. 2001). Data points represent target effects following exposure to ions of different charge and velocity and largely varying LET. Biological endpoints include cell transformation (●), HPRT Mutation (▽), Dicentrics (■), centric rings (◊), initial isochromatid breaks (▲), complex exchanges (o), harderian gland tumors (**o**), skin cancer in rats (▼). Quality factor (—) is displayed along with the most likely range (·—·) and maximum range (····).

Figure 3 shows RBE for a single biological endpoint by different ions having similar LET values. These results suggest that ion charge and velocity may be as important as rate of energy loss in determining biological effectiveness. Most RBE data are taken from irradiation experiments on mice, rats, and cell cultures. The data suggest as LET increases past 100 keV μm^{-1}, the stochastic risks decrease.

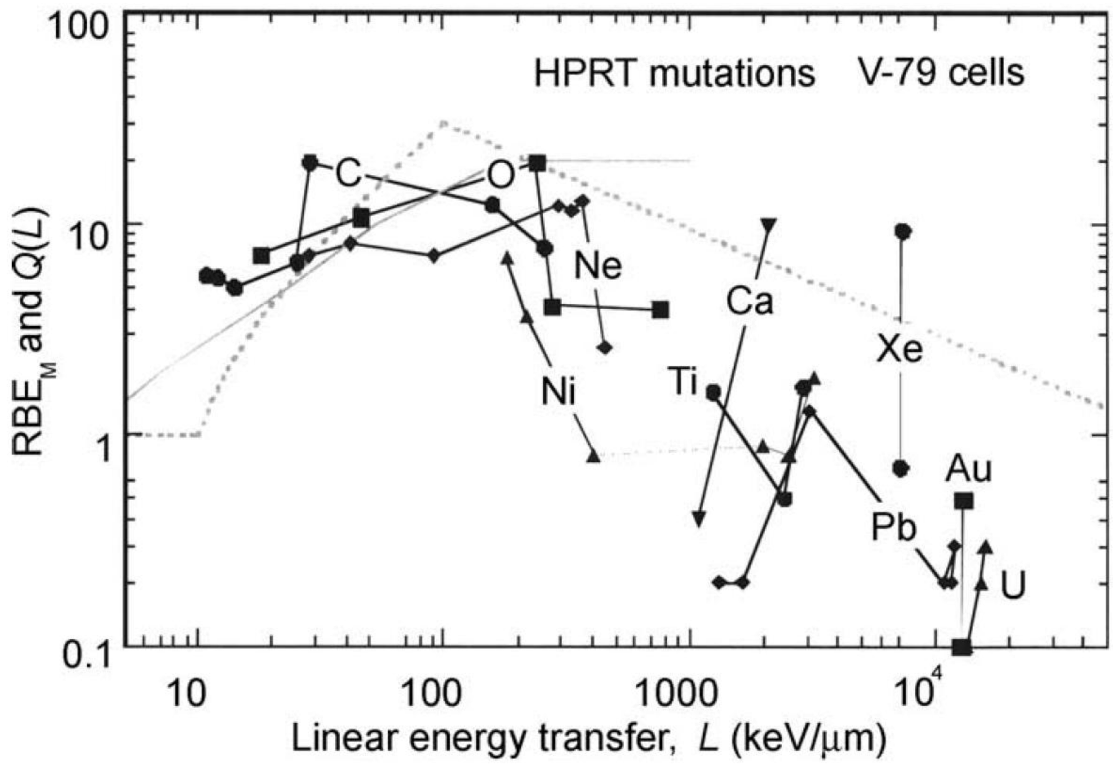

Figure 3. RBE and quality factor as a function of overlapping LET values for various heavy ions. (ICRP 2003). Data points represent RBE_M for each heavy ion at its corresponding LET. The quality factor is displayed (····) as a function of LET.

Dose-rate plays an important part in radiobiology because it allows for cellular repair processes that can occur between subsequent target ionizations. Dose rate effectiveness plays a more significant role for low-LET radiation than for high-LET radiation in cases of cell kill. Compared to the diffuse photon dose, the densely ionizing tracks of a heavy ion isolates its dose to a fewer number of targets, leading to increased cell kill. In the high-Z GCR environment, target traversals are few and far between, leading to very-low dose rate and low total dose compared to the exposures used in most RBE measurements. Carcinogenic effects are the prominent radiation risk factor for space missions. Fluence rates are estimated to be roughly 4 protons-cm^{-2}-s^{-1}, 0.4 helium ions-cm^{-2}-s^{-1} and 0.04 HZE particles-cm^{-2}-s^{-1} at solar minimum when GCR intensities are at their maximum values. This approximates a single mammalian cell being hit by protons once every three days, by helium ions once every month, and by HZE particles once every 300 days (Curtis et al. 1995). RBE ratios may not be as appropriate for understanding biological effects from space radiation. The type of damage, the particle track structure, fluence, and fluence-rate must be considered.

Dose-fractionation or low dose-rate effects on RBE are important topics when considering space radiation. RBE is specific to a cell type and can also show dependency on dose-rate. For low-LET irradiation, the survival curve often shows a shoulder effect at lower doses and this response is often described as sub-lethal damage repair. As LET increases, this effect diminishes. The LET value is an average of a broad range of possible energy deposition events by a traversing ion. Very high energy events are possible, but very unlikely. If an individual cell is only traversed by a heavy ion once every 300 days then the most probable energy loss value is more relevant than the mean. This effect varies for ions of different Z and velocity. Monte Carlo simulations can be used to determine a mean and most probable energy deposition for an ion traversing a target.

The Bethe-Bloch approximation of energy loss shows that ions of different atomic number and equal kinetic energy per nucleon interacting in the same material deposit their energy at different rates since their stopping powers are based on the square of their charge. This approach does not account for processes other than coulomb interactions, such as production of recoil particles and nuclear fragmentation. Based on the Bethe-Bloch approach, ions of equal LET but different Z must have different velocities. This approach describes energy lost over an incremental distance and can be compared to LET in a thin target. As kinetic energy increases, orbital electrons with a smaller velocity than the corresponding ion velocity will be stripped off, leaving an ion with no electrons and an effective charge equal to its number of protons. This resulting effective charge of the ion determines the magnitude of excitation and ionization of target atoms (Kraft et al. 1992).

The actual amount of energy lost by individual particles passing through a thin absorber can range over several orders of magnitude, and detector thickness strongly influences the shape of the distribution curve for energy loss. For thin target slices, such as the ones used in this research, the shape of the curve can be predicted with Monte Carlo simulations, and can account for range-energy straggling. Range-energy straggling describes the required target thickness for the traversing ion to undergo all probable interactions and energy-loss events.

Fragmentation and electromagnetic ionization and excitation vary for ions having different Z and velocity. Ion fragments and high-energy secondary electrons contribute to the possible energy deposition events. The structure of an ion path can be well described by the locations of the many energy depositions within small volumes representing sensitive cellular targets. Studying track structures of multiple ions at equal LET, or with equal velocity, introduces one possible approach for identifying physical parameters which may predict biological consequences.

As an ion traverses a target, most interaction events are with the target atom electrons and can result in soft, glancing collisions or hard, knock-on collisions. The distance between the traversing charged particle and the target atom is referred to as impact parameter. A soft collision occurs when a charged particle passes an atom at a large impact parameter, and the particle coulombic field excites or ionizes the target atom by the transfer of a few eV. A hard collision occurs when a charged particle passes by an atom at a small impact parameter, interacting with a single electron and imparting much more kinetic energy (Attix 2004). This target electron is called a delta ray and is energetic enough to create its own, separate track. For an ion with a high velocity and very small impact parameter, delta rays can be produced with enough kinetic energy to travel up to several millimeters away from the ion path in tissue or water targets. As ion velocity decreases, delta rays are produced with significantly shorter range. A very broad spectrum of kinetic energies and emission angles is imparted to delta rays, determining where they deposit their dose. Very low-energy delta rays (below 1 keV) remain near to the ion path, while delta rays of much higher-energy can travel much farther and can create other delta rays.

Ions having equal velocity produce the same spectrum of delta ray kinetic energies, although in different numbers, based on the square of the effective charge of the ion. The resulting delta ray tracks affect the same sized volumes. Figure 4 describes the production of low-energy delta rays for a heavy ion respective to angle of incidence. The electrons of interest in this research have more than 1 keV of kinetic energy, so they are produced primarily in smaller-angle interactions. In Figure 4, delta rays with greater than 1 keV kinetic energies are represented by the binary collisions with target atoms. These collisions are strongly dependent on impact parameter and produce delta rays by freeing electrons from the target atoms.

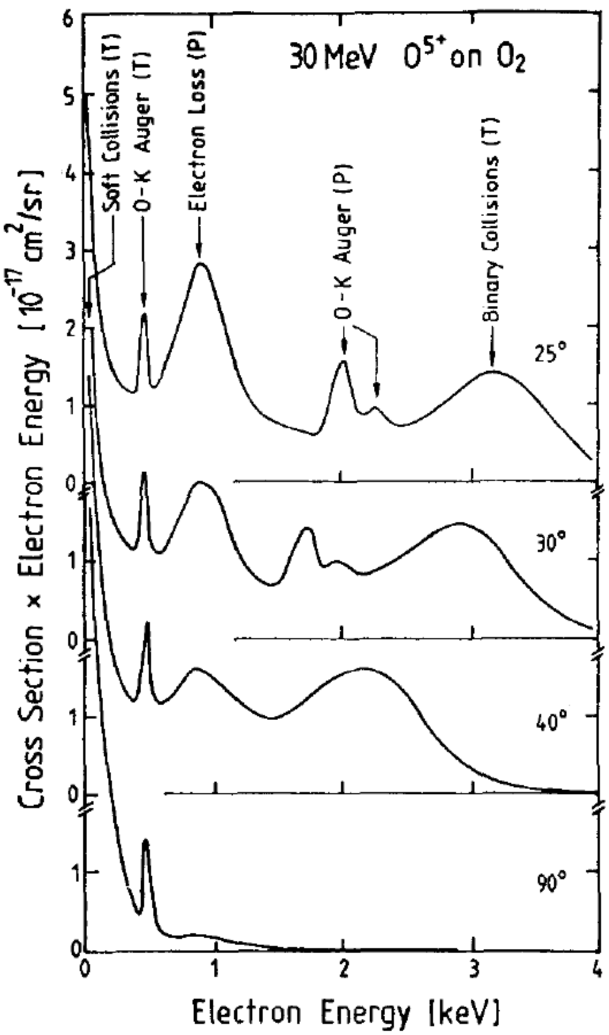

Figure 4. Delta rays are produced when the primary ion passes and receive kinetic energy based on the angle and impact parameter. The data presented here represent a 30 MeV oxygen ion traversing a water target (Kraft et al. 1992). Cross section curves are presented for increasing interaction angles of the traversing ion.

The sharp, discrete peaks are from Auger processes (for both the target and projectile atoms) where an excited atom emits an electron. Lower-velocity ions suffer some energy loss to electron pickup (and loss), as they approach their Bragg peak. This effect creates the auger and electron loss peaks seen in Figure 4. Higher-velocity ions yield only the binary, target auger, and soft collision peaks.

Dose surrounding the ion path is primarily due to the energy deposition by binary collision electrons. Electron energy, E_e, the emission angle, θ, and the particle energy, E_p, are correlated according to Equation 1for small impact parameter.

$$E_e = \frac{4m_e}{m_p} E_p \cos^2\theta \tag{1}$$

The terms, m_e and m_p, are the electron and projectile mass, respectively (Kraft et al. 1992). Higher-energy electrons are more forward directed, while lower-energy electrons are emitted at a larger angle from the ion path. Low-energy electrons are emitted isotropically for large impact parameters.

Delta rays with energies below 100 eV travel only a few nanometers from the primary ion track and create ionization regions, commonly referred to as ‘spurs’. Electrons with energies of 100 to 500 eV electrons can extend ~7 nm from to the primary track, creating a track known as a ‘blob’. Electrons with energies between 500 and 5000 eV have short tracks, and electrons with energies above 5000 eV have enough range to create tracks that take them away from the primary ion path. These high-energy electrons can go on to create additional delta rays producing the spur and blob ionization regions. Figure 5 displays electron energy vs. penetration distance in water. Electrons having less than 1 keV are expected to be contained within ~20 nm.

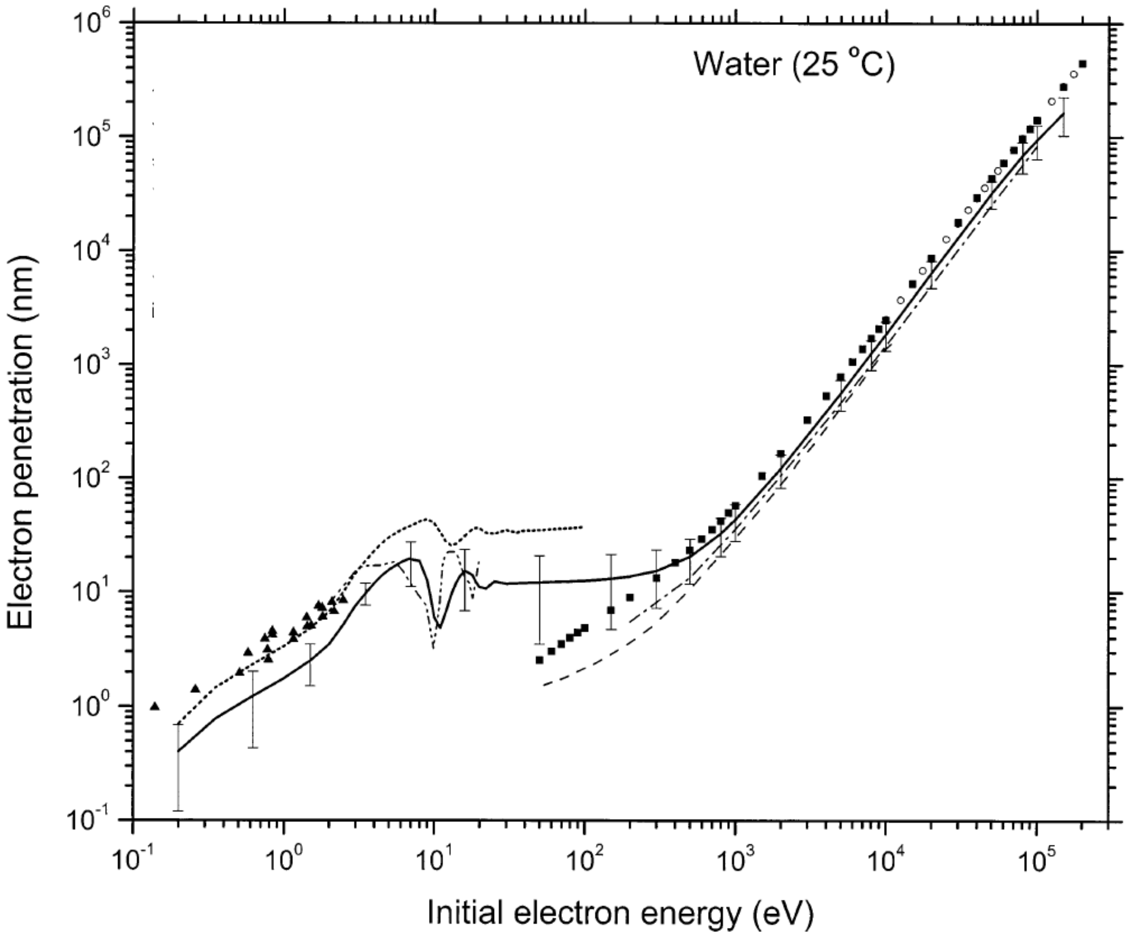

Figure 5. Electron penetration distance in water vs. kinetic energy (Meesungnoen et al. 2002). Monte Carlo-simulated work represented by solid line (—), with errors bars showing the 95% confidence intervals.

The different data points and trend lines represent different theoretical models and referenced experimental data. This information is only used as a guideline for setting up the appropriate dosimetry approaches utilized in this research.

Electron tracks establish the energy deposition and spatial distribution of initial water and DNA radicals. DNA single and double strand breaks are created either directly by ionization from charged particles or indirectly by the diffusion of free radicals produced by excited atoms. Water radiolysis is important for the indirect action of radiation. The damage produced by water-derived free radicals is chemically modifiable damage and accounts for ~70% of the damage from low-LET irradiation (Chatterjee and Holley 1992). The chemical track is modified over time by diffusion and reactions of chemical species. In living cells, the reactive species undergo diffusion and chemical reaction over 10^{-12} - 10^{-6} s and have a diffusion range of ~4 nm (Bolch et al. 1990).

Ionizing radiation is extraordinarily efficient in causing biological consequences compared to that caused by oxidizing chemicals and the body's own endogenous processes. The non-randomness of energy delivery to sensitive sites, such as DNA, causes that effect (Goodhead 2006). Ionization sites tend to be clustered at the end of electron tracks and diffusion of water radicals expands those clusters by a few nanometers. Low-LET radiation is sparsely ionizing, but about 25% of energy is deposited in clusters at the ends of delta ray tracks. Double strand breaks (DSB) are commonly produced from this clustering of ionizations resulting from direct and/or indirect effects. High-LET tracks consist of a densely ionizing core and a low-LET delta ray penumbra, each contributing roughly 50% of the total dose. Ionization density in the track core is extremely high, and some of this energy is carried away by delta rays. Very-low energy delta rays that create the 'blobs' and 'spurs' lie in the vicinity of the track core. These delta rays deposit their kinetic energy across very short distances and can create clustered lesions when the primary ion traverses a chromosome. Sensitive cellular-target volumes are described in Table 2.

Table 2. Dimensions of sensitive targets on the cellular scale (Goodhead 2006).

Scale	Biological Target
100 µm	Adjacent cells are damaged
10 µm	Cell nucleus. Large insult, or possibly none.
1 µm	Chromosomes. Correlated damage in separate chromosomes
100 nm	Chromatin. Correlated damage fragments
10 nm	Clustered damage, fragments
1 nm	Recombination, bi-radical reactions

The complexity of a lesion generally depends on the LET of the charged particle. Clustered damages are found when there is more than one break in a DNA strand within 2 – 10 base pairs (Goodhead 2006). Complex breaks can occur when there are multiple breaks on one or both strands of the DNA helix, producing single strand breaks (SSB) and DSB. These lesions are harder to repair and promote an increase in the biological effectiveness of ionizing radiation.

Heavy ions introduce a higher fraction of complex lesions, leading to chromosome breakage and possible rearrangement. This damage can progress to a point where no repair is possible and the cell dies. The number of residual DNA breaks in a surviving irradiated cell is one characteristic of radiosensitivity and varies by cell type and radiation type. The cell cycle also plays an important role, and dose rate or fractionation can interact with cell cycle changes to enhance or diminish biological response. Aberration type, such as complex and simple-type exchanges, must be considered to establish RBE values. Increasing LET usually increases the ratio of complex to simple-type exchanges. RBE for ions of equal LET is better established for a cell killing scenario than for chromosomal aberrations (Ritter and Durante 2010).

It is stated in NCRP Report No. 153 (2006) that very few experiments have studied the possible variation of biological effects of radiations with a fixed-LET value but different combinations of ion charge and velocity. Katz noted that such effects are masked at high doses where on average more than one particle traverses a cell (Katz et al. 1971). The full spectrum of secondary particles must be simulated and scored on a biologically relevant scale to effectively assess the effect of track structure on individual damaging events within single cells. The biological effectiveness of radiation also depends on dose-rate because cell cycle responses have more time to repair the cell during low-dose rate irradiation. This research analyzes the radiation dose for individual events for seven different GCR ions at prescribed kinetic energies and stopping powers. Cell type and time scales are not simulated and are not considered part of the track structure influence on damaging ability.

Analytical Approaches

To effectively describe the track of heavy ions through a target, interactions must be accounted for on nanometer to millimeter scales. Energy deposition events vary both longitudinally and radially from the primary ion path. LET along the path of the ion is characteristic of the immediate stopping power of the particle and the trajectories of secondary radiations. As mentioned in a previous section, higher-energy delta rays are more forward directed and follow straighter paths. The lower-velocity ions used in this research experience increasing stopping power because the target depths are large in relation to their total range. Those with higher velocities show no increase in stopping power when traversing a 1 mm thick target.

The radial dose surrounding an ion track is well described by an 'amorphous track' model. In this type of model, track structure is described by the radial distribution of local dose around the primary particle path due to the primary particle and its delta rays. The structure of the track lies inside coaxial cylindrical shells about the ion path and is traversed by secondary electrons ejected from the medium by the passing ion. The ion track consists of a core and a penumbra region. The core is a region of very high-energy density where many soft collisions transfer small amounts of energy (Chatterjee and Schaefer 1976). The core is estimated to have a radius, r_c, proportional to the velocity (β) of the particle and is described (Chatterjee and Schaefer 1976) by the equation:

$$r_c = 0.0116\beta \ \mu\text{m}. \tag{2}$$

Energy is deposited in the core by excitation of individual target atoms or in collective oscillations of electrons when the heavy particle passes. These soft-collision interactions are much more frequent than hard collisions but transfer much less energy (Chatterjee and Schaefer 1976). Based on the Chatterjee equation, most GCR have a core radius ranging from about 1 to 10 nm. The core radius is not exact and is only meant to establish a boundary between delta rays that essentially have no range with those that do. Some secondary electrons may be included within the core and have only a few eV of kinetic energy.

Knock-on collisions create the delta-ray field, known as the penumbra, that can be depicted as a cylindrical shell region along the axis of the primary particle direction. The penumbra encompasses a region of ionizations whose energy decreases exponentially with increasing distance from the primary particle path. A wider delta ray penumbra imparts a lower local ionization density for the same total dose (same LET) to a large enough target. The penumbra radius, r_p, is characterized in the following equation (Chatterjee and Schaefer 1976):

$$r_p = 0.768\mathrm{E} - 1.925\sqrt{E} + 1.257\ \mu\mathrm{m} \qquad (3)$$

where E is the kinetic energy of the particle in MeV n^{-1}. The penumbra radius does not extend to the maximum delta ray range because there are so few electrons reaching this distance, the dose is essentially zero. Figure 6 characterizes the core and penumbra regions by the black and white circles, respectively. Delta rays with ranges smaller than the core are not depicted and considered part of the core, while energy deposited outside of the penumbra is not considered.

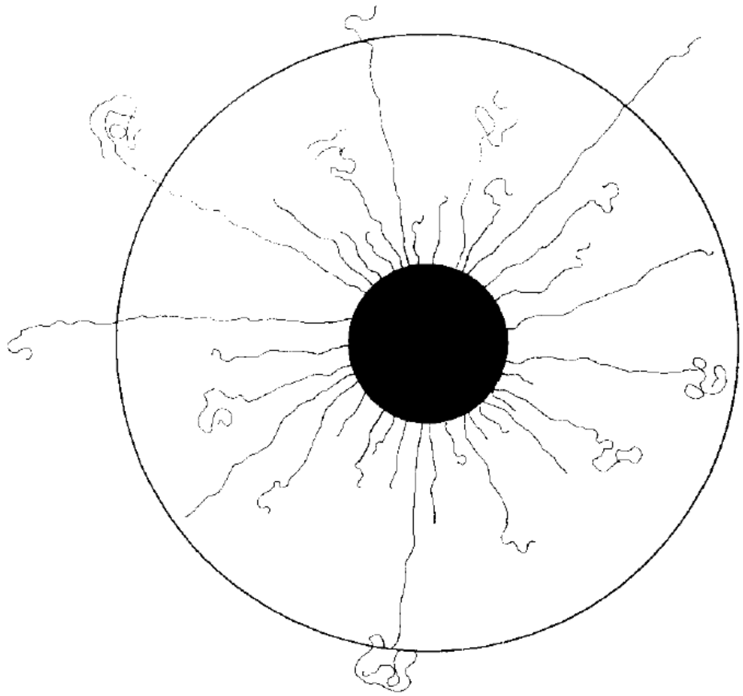

Figure 6. Cross-sectional view of the ion track with escaping delta rays that form a penumbra (Chatterjee and Holley 1991). The dark circle represents the track core.

The amorphous track model yields a radially-dependent dose that decreases as r^{-2} (r being the distance perpendicular from the primary particle path). This approach generates radial dose values that would be expected from the delta rays seen in Figure 6. Chatterjee presented Equations 4 and 5 for energy density (kev μm^{-2}) within the core (Q_c) and penumbra (Q_p) (Chatterjee and Schaefer 1976):

$$Q_c = \frac{LET_\infty/2}{\pi r_c^2} + \frac{LET_\infty/2}{2\pi r_c^2 ln(\sqrt{2.718}\ r_p/r_c)} \tag{4}$$

$$Q_p = \frac{LET_\infty/2}{2\pi r^2 ln(\sqrt{2.718}\ r_p/r_c)} \tag{5}$$

where r is an independent variable denoting radial distance from the center.

The delta ray distribution formula, discussed by Butts and Katz (1967), treats all electrons as free from target atom orbitals, and delta rays are considered to scatter at an angle dependent on their kinetic energy (w) relative to the maximum possible delta ray energy (w_{max}), following the equation (Butts and Katz 1967),

$$\cos^2 \theta = \frac{w}{w_{max}} \quad . \tag{6}$$

The Katz model provides a theoretical model for determining delta-ray energy fluence. This provides some added detail to the dosimetry within the amorphous track model by detailing individual delta-ray tracks within the cylindrical regions. The following equation:

$$dn = \frac{CZ^{*2}}{\beta^2} \cdot \frac{dw}{w^2} \tag{7}$$

can be used to determine the number of delta rays per unit path-length having kinetic energy within a spectrum of $w + dw$. In this equation, w represents electron kinetic energy, Z^* is the effective charge of the ion, and C is described in the reference as having a value of 0.0085 keV μ^{-1} (Butts and Katz 1967).

The amorphous track model simplifies the Butts and Katz theory by assuming all delta-rays travel perpendicularly to the primary particle direction. This model does not predict individual delta-ray events, only the average energy deposited at a radial distance that would be expected from delta-ray traversals. The amorphous model has been developed with theoretical and experimental data and provides a fairly accurate estimation of how dose extends radially from the ion path. Originally established using proton data, the model was extended to heavier ions by finding that the radial distribution of local dose varies as a function of Z^2/β^2, where Z is atomic number and β is particle velocity divided by the speed of light (Katz 1978).

The amorphous track model estimates the radial dose surrounding an ion path at a point where delta-ray equilibrium exists, providing dose estimates from very small to very large radii. This method provides an instantaneous radial dose estimate and does not account for deviation of the primary particle away from the track axis as it traverses a target. When studying a real target, ions of higher velocity require increased target depth to achieve delta-ray equilibrium. However, the chances of scattering and nuclear fragmentation both increase as the particle traverses deeper into a target. Track structure continues to evolve along the particle path, so the radial dose depends on more than just delta rays. Of course, the most significant source of ionizations lies within the core or just outside because electron fluence is highest. Farther away from the core, delta-ray events are much more diffuse, similar to those produced by x and gamma rays. The radial dose distribution indicates the lateral spread of the particle track but ignores the stochastics of possible energy-loss events along the track (Cucinotta et al. 1998).

Monte Carlo methods for simulating individual particle traversals are an effective method for detailing track structure. Instead of calculating ionization densities, individual energy deposition events and particle fluences are simulated. This information is used to correlate the spatial distribution of energy deposited with reference to biological targets. Monte Carlo methods can be used to report the statistical nature of the location of energy deposition sites on the DNA molecules, the amount of energy deposited, the spectrum of particles involved, and the diffusion of water radicals (Holley and Chatterjee 1996).

On the cellular level, variations in the particle trajectories of different ions cause a change in energy deposition and the resulting target effects. The spatial distribution of energy deposition (in a cell nucleus) from a high-atomic number, high-energy (HZE) particle track depends on the traversing particle, cellular targets, recoil nuclei, nuclear fragments, and delta rays. Targets of interest are DNA strands, with a diameter of about 2 nm, that make up a chromosome that is about 1.4 µm thick. Radiation directly strikes the target, disrupting molecular bonds, and is described as a direct effect. Damage is produced by both direct and indirect energy deposition events. Radiation can interact with the water inside the cell to create free radicals that can then migrate to damage DNA. Diffusing water radicals created from interactions in the water surrounding the DNA describes the scavengeable component of DNA damage (Nikjoo et al. 1998). The diffusion length of free radicals in a cellular media is commonly estimated at about 3 - 4 nm (Goodhead 2006; Chatterjee and Holley 1992), relevant to DNA base pair volumes. Radical diffusion can be estimated as a cylindrical region around the constant slowing-down path of a delta ray. The number of free radicals created is proportional to the energy deposited along a track. It is expected that larger penumbras will produce a larger field of radicals, but the density of radical formation may actually be of more concern. Monte Carlo methods can simulate the ionization of water molecules and their diffusion leading to strand breaks (Holley and Chatterjee 1996). Turner used Monte Carlo techniques to predict radical diffusion following the initial physics interactions in a medium (Turner et al. 1991). This 1991 study modeled a charged-particle path along with all associated secondary electrons. These particles were transported, step by step, until their energies fell below the minimum threshold for electronic transitions in liquid water. Each interaction was capable of initiating water radiolysis, where the resulting radical molecules could be tracked to a point of recombination leading to radical diffusion coefficients.

Clustering of ionizations on a DNA strand has been shown to produce lesions that are the most difficult to repair (Goodhead 2006). An energy deposition threshold of 17.5 eV is a common estimate for the amount of energy deposited in one sugar-phosphate volume to create a single strand break (Nikjoo et al. 1998). That local energy deposition estimate is representative of base damage as well as strand damage (Goodhead 2006). DSB can be predicted based on energy deposition values in a target in the penumbra or by simulating two events on a DNA strand that happen to lie within a few base pairs distance from each other. A separation of 30 base pairs is commonly set as the maximum separation between two single strand breaks to create a DSB (Charlton et al. 1989). Particle tracks impart a random orientation of ionizations leading to clustering of DNA lesions, which complicates repair. An absorbed dose of 1 Gy of x rays is estimated to create 40 DSB, 150 DNA crosslinks, 1000 SSB, and 2500 base damages (Goodhead 2006).

To relate the variations of track structure across different ion species and different velocities (but similar LET), charged particle tracks can be modeled by partitioning the energy deposition between primary track core and delta rays (Holley and Chatterjee 1996). The amorphous track model is restricted in that it only considers a cylindrical (or spherical) geometry surrounding the particle track and ignores the broad range of possible energy deposition events by a varying number of secondary particles. This research includes this range of events with frequency distributions of energy imparted to small volumes surrounding the primary particle path. Information from the amorphous track model can be compared with Monte Carlo simulation of energy imparted in a volume at some radial distance from the primary particle track.

Microdosimetry is the measurement of energy deposition events and particle fluence on scales relevant to cells. Tissue equivalent detectors containing low pressure gas can be placed within a biological target to simulate a cell-sized volume. This method allows dosimetry to be performed without disturbing the radiation field. For the purposes of this research, dosimetry quantities are scored in, or near, a heavy ion track in a water medium to generate the dose and number of particle traversals experienced by a cell nucleus. By placing the detector at different distances from a particle track, radial dose can be calculated.

Many radiation biology experiments irradiate thin layers of cells in culture, thin enough so that the LET does not vary appreciably. A major topic of discussion is track structure in thin targets, similar to a plane of plated cells in culture. The track structures are used to make estimates for energy depositions in the cell nucleus. Magnitude of energy deposited and clustering of events are the main criteria for determining damaging effects. The most probable energy deposition (rather than the mean) can be determined by Monte Carlo energy distribution simulation, giving more relevant results for very low fluence applications. The most probable value is generally less than the mean and should be used to calculate the dose that a cell would receive by a single ion traversal. The improbable and very high-energy loss events exaggerate the mean value as particle velocity increases. The Monte Carlo approach used in this research details the energy fluence of particles induced by a traversing GCR in a water target. Data are then used to make predictions on the relative damaging ability of different GCR for comparison with theoretical models.

Damaging ability of a track structure can be described by the ionization density within a cell nucleus that leads to DNA strand breakage, free radical production, and clustering of ionizations. Damage can be assessed by simulating the probabilities of ionization density and particle traversal frequencies within a large group of cells traversed by an ion.

CHAPTER III

METHODS

The goal of the research is to show differences in the track structure of different ions by modeling particle fluence and energy deposition events on a biologically-relevant scale. This analysis utilizes Monte Carlo simulation of GCR in water targets to model track structure and the corresponding interactions in targets similar to that used in the amorphous track model and microdosimetry. The FLUKA code can be used to provide the track structure for all interactions, detailing the paths of particles and their secondaries. Mean and most probable energy loss values are established from simulating large numbers of particle histories.

The first analysis in this research focuses on the track structure of GCR having equal stopping power. The Bethe-Bloch equation was used to determine particle velocities for ions with stopping powers of 100 keV μm^{-1} in water. This value was chosen because it correlates with the peak LET value on the quality factor curve, meaning it is the most detrimental. Kinetic energy values for each ion are as follows:

- Beryllium-8: 6.80 MeV n^{-1}
- Carbon-12: 18.48 MeV n^{-1}
- Oxygen-16: 37.52 MeV n^{-1}
- Magnesium-24: 106.3 MeV n^{-1}
- Silicon-28: 164.0 MeV n^{-1}
- Calcium-40: 631.5 MeV n^{-1}
- Titanium-48: 1582 MeV n^{-1}

The energy and range of nuclear fragments and delta rays produced in the target are strongly influenced by these primary particle velocities. As a result, there are variations in the energy deposited in a target for the different ions. For the second part of the research, GCR are compared with equal velocity and different LET. The velocity, presented as kinetic energy per nucleon, was chosen to be 600 MeV n^{-1} because it approximates the most probable GCR velocity in the space environment (NCRP 2006). Variations in track structure for equal velocity ions are only dependent on Z.

The FLUKA code was used to model the LET of each ion traversing a 1 μm thick water target slabs. The first analysis was to calculate the mean value of the spectrum of energy deposition events by the ion. This should be quite close to the 100 keV μm^{-1} stopping power predicted by the Bethe-Bloch equation. The most probable value is taken from a histogram of the energy loss spectrum and is relevant in analyzing individual particle traversals. Energy deposition distributions are performed with and without consideration for delta-ray tracks. To account for delta-ray equilibrium, electron fluences across thin slabs (perpendicular to the primary ion track) were scored at multiple depths inside a thick target. These data allow for the analysis of primary particle scatter, fragment production, and the build-up of delta rays toward equilibrium. The next step was to simulate those energy loss events on a scale relevant to cellular targets to create the track structure model.

Simulation Model

The FLUKA code can be used to account for all the particles involved in track structure analysis relevant to radiation biology studies. Interaction cross sections are specific enough to account for the broad kinetic energy spectrum of GCR. The code can be used to simulate delta-ray transport in complicated geometries and modeling their corresponding trajectories and energy deposition distributions.

The first target geometry for irradiation was made up of coaxial cylinders, parallel to the ion path and similar to the amorphous track model approach. Energy deposition at increasing radii was modeled along the primary particle track to establish a smooth trend of dose vs. radial distance to provide dosimetry for critical volumes as small as those found within a cell nucleus. Unlike the amorphous track model that gives an energy density value relative to radial distance, Monte Carlo models provide the spectrum of energy deposited by individual events in the regions surrounding the particle track. This process accounts for energy deposited based on particle type to provide comparisons at increasing depths in a target.

To develop sufficient data statistics, GCR traversals are modeled as a pencil beam penetrating a cylindrical slab of water. In this case, the primary particle is traveling into the page at the center of the figure. By simulating the primary particle through the same entrance point for each simulation, the delta-ray penumbra forms around the core axis. This slab is constructed of cylindrical shells of increasing radius, as shown in Figure 7 (not to scale).

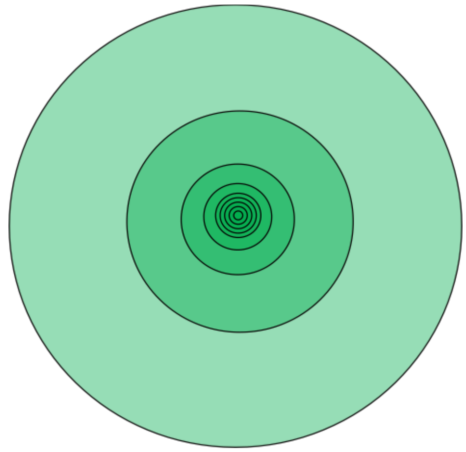

Figure 7. Cross-sectional view of the cylindrical shell geometry.

The dimensions were chosen to represent significant distances within a cell nucleus up to a few cell diameters. The innermost shell has a radius of 5 nm, roughly the size of the track core. The shells extend up to 1 cm radius to account for the very high-energy delta rays and scattering nuclear fragments. The slab is perpendicular to the beam axis, with a thickness of 1 μm. Multiple slabs, with the same thickness, are placed inside a larger target to provide particle fluence data as delta rays build toward equilibrium. This may require up to several millimeters of depth for higher-energy ions. These dimensions are intended to provide energy fluence data from a DNA-sized region of interest all the way up to multiple cell diameters.

Using the SCORE and USERBDX functions, the FLUKA code estimates the total energy deposited, frequency of energy deposition events in each region, and the particle fluence for each cylindrical boundary. Particle fluence information is sorted by particle type and kinetic energy when crossing the cylindrical boundaries, in conjunction with energy deposition scoring for each region of interest. Data can be scored by particle of interest, so the primary emphasis is placed on charged particles to account for the primary particle, charged fragments, and delta rays. Data output provides energy fluence and energy deposition information within the delta-ray penumbra produced by a GCR as well as its fragments. This information describes how the path of the primary ion is affected as it traverses the water medium. Primary and secondary ions will experience some scatter away from the initial beam axis, diffusing the track core measurements within the 5 nm cylinder. FLUKA input files are displayed in Appendix A for several irradiation scenarios and target geometries.

The FLUKA code cannot be used to follow the paths of electrons with kinetic energies below 1 keV. For the purposes of this research, the range of electrons below 1 keV is assumed to remain very near to the primary track core. The outer edges of the core are assumed to consist of electrons below a few keV and of water radicals, both contributing to very high-ionization density. Those low-energy electrons produced in ionizations farther away by high-energy delta rays are not expected to have enough range to cross the corresponding region boundary, and their energy is deposited along the path of the parent particle. This research assumes that the production of water radicals affects such small distances (~4 nm) that they are considered to react at the point of production. The FLUKA code is not capable of simulating the diffusion of chemical species.

The second simulation geometry utilizes the USERBIN function to provide energy deposition and particle fluence on a target-by-target basis. This approach generates dosimetry data for cell nuclei-sized volumes, to provide analysis of the number of sensitive targets being affected by a traversing ion. A thicker target accounts for the necessary delta-ray buildup for the higher-energy ions and gives better analysis for damage to a group of targets. Since nanometer volumes are not accounted for in this part of the research, the primary ion has more room to scatter off its path without negatively affecting the results. A water cube, with 1 mm edges, contains a mesh of many small cube-shaped voxels. Each voxel has 10 μm edges, giving a volume similar to a cell nucleus. By simulating particle traversals within this geometry using the FLUKA code, the probabilities for dose and number of particles traversing each voxel can be determined. The geometry is not meant to perfectly simulate a group of cells, only approximate the relevant biological target volumes. The geometry is depicted in Figure 8.

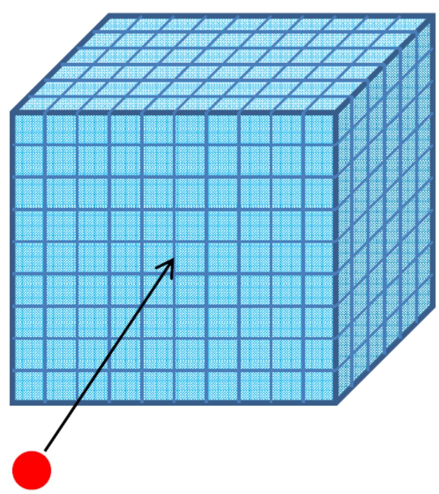

Figure 8. Mesh cube geometry for taking microdosimetry measurements inside a 1 mm thick cube. The red circle represents the incident primary ion.

The target consists of 1 million voxels, many of which may not receive any dose. By modeling the traversal of 200,000 ions (of the same type) through the same point, frequency distributions of dose and particle fluence can be determined with appropriate statistics. Dose and particle fluence from electrons is recorded in each voxel.

The final target geometry for this research is a cylindrical mesh with a 5 μm radius. The purpose for this geometry is to provide additional target hit data, using the USERBIN function, for very small volumes within the cube mesh. The cylinder mesh is contained inside of a single 1,000 μm^3 voxel from the 1 mm^3 geometry. The cylindrical mesh is 10 μm long and simulates 1 million target voxels that are nearly cube-shaped, having 10 nm edges. Similarly, the geometry can be used for radial dose comparison with the amorphous track model, as well as the cylindrical shell model previously described.

Analytical Methods

The FLUKA code was used to calculate the energy deposited in each cylindrical region, so results were compared with expected radial dose calculated by the amorphous track model. The next step was correlating the radial dose distribution with the spectrum of energy depositions in each cylindrical region. This research also treated the penumbra and core regions separately but accounted for individual events rather than relying on an average. Individual energy deposition events can be described radially. Delta-ray production was compared with the Katz delta-ray distribution formula. These electrons were scored as they crossed each region for the cylindrical model and the mesh cube.

The cube geometry provided data for individual cell nucleus-sized target events to simulate delta-ray effects on surrounding cells. Dose per voxel and the number of particle traversals per voxel were then compared across the different ions to establish damaging ability. The mesh cylinder provided data inside the 5 μm radius of a cell nucleus. The target voxels represented DNA strand-sized volumes; dose, number of particle traversals, and dose per electron were scored as well for each target.

The biological parameters considered for this research were ones of target geometry and dosimetry effects. The goal of the research was to determine the physical damaging ability of different ions relative to each other. Delta-ray energy fluence and local dose values identified the potential for damage occurring in the target. No consideration was made for damaging effects across different types of cells or with regard to dose-rate effects. The cylindrical radial dose geometry was intended to relate FLUKA results with commonly used radial dosimetry of heavy ions. The USERBIN mesh geometries provided more accurate data, accounting for target hits. Damaging ability was then compared on both intercellular and intracellular scales.

CHAPTER IV

RESULTS

Energy Deposition Trends

Monte Carlo simulation provides the user with more options for scoring spatial distributions of dose and particle fluence than the amorphous track model. Simulations also allow for studying the dose as a function of particle fluence through individual target regions. This section presents the results from the particle simulations for each irradiation scenario and target geometry.

The first analysis describes the energy deposition trends for several ions traversing thin slabs of water. Figure 9 depicts ions with calculated stopping powers of 100 keV μm^{-1} using the Bethe-Bloch approach, while Figure 10 shows ions of equal velocity (600 MeV n^{-1}) but different stopping powers.

Not all ions are represented in the Figure 9 for visual clarity, but the trend is clear. The data presented here describe energy deposited by a traversing ion, whose secondary particles are assumed to deposit their energy at the point of production. There is no energy escaping the target, except for that of the primary ion, so this figure represents the total value for each energy-loss event.

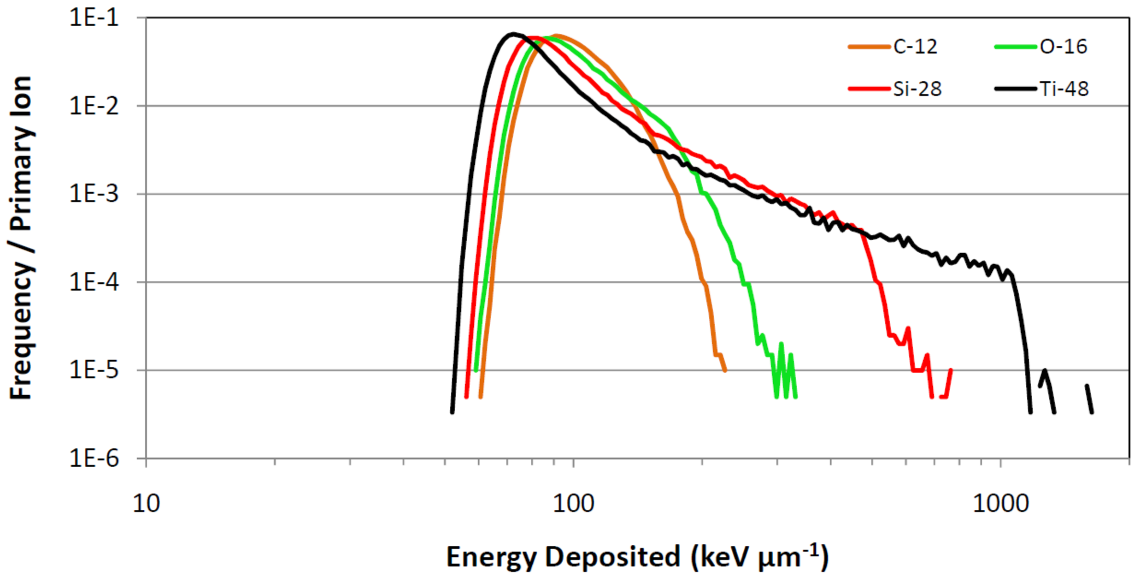

Figure 9. Spectrum of energy deposition events by ions with stopping powers of 100 keV um^{-1} in a 1 µm thick water slab. The curves represent the frequency of total energy deposition by individual particles averaged over the total number of particles simulated.

For ions of equal stopping power, the mean value of energy deposition is roughly the same, but the spectra have different shapes. The most probable energy deposition value is located at the peak of each curve. Most probable values describe the most likely energy-loss events for individual primary particle traversals.

Figure 10 displays the same comparison as Figure 9, but for ions with equal velocity (600 MeV n^{-1}). There are similar energy deposition trends for these ions, but there is a difference in magnitude of energy deposited, based on the ions' charge (Z^2/β^2). In this case, β is nearly identical for these ions, as its calculation depends only slightly on the number of neutrons held by each ion. The reason the lower-velocity ions deposit lower values of energy, is because there is decreased secondary-electron production due to decreased effective charge of the primary ion.

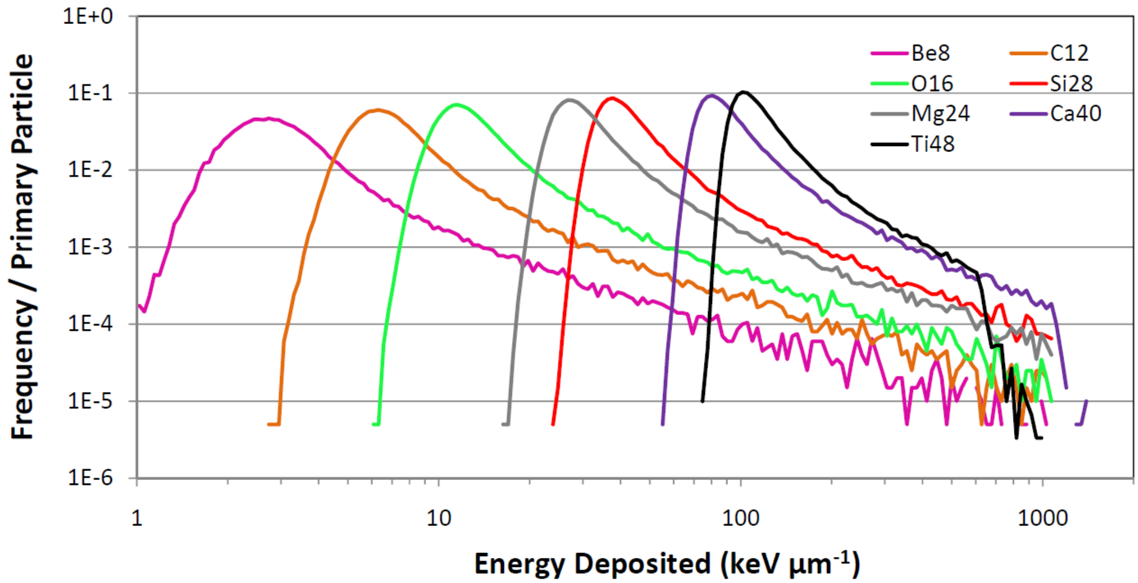

Figure 10. Spectrum of energy deposition events in a 1 µm thick water slab for ions having equal velocities of 600 MeV n^{-1}. The curves represent the frequency of total energy deposition by individual particles averaged over the total number of particles simulated.

Energy loss described by a calculated stopping power is not necessarily the energy imparted to a target. The data reflect total energy deposition per event and frequency is averaged over the total number of primary particles traversing the target. The effect of velocity is very apparent in both Figures 9 and 10. As in Figure 9, the higher velocity ions experience energy deposition events up to several MeV. As a result, there are very rare events representing very high-energy loss of a few MeV that significantly increase the average value representing LET. When cells are only traversed by a heavy ion every few days or weeks, the very high-energy interactions are too rare to be concerned with and can be neglected for risk analysis. The resulting LET is shown to decrease, and the focus should be placed on the most probable value of energy deposition. The most probable energy deposition value for an ion decreases with increasing velocity since it is not influenced by the high-energy events.

Table 3 displays the average and most probable energies imparted to a 1 μm thick water slab as simulated using the FLUKA code. Ions with equal stopping power produce similar mean values but different most probable values of energy deposition. The most probable value depends strongly on the ion velocity. The LET of the 600 MeV n^{-1} ions are presented to display the effect of Z on total energy deposition in the slab. In this case, the β^2 value is nearly identical for these ions, and it was determined that their energy deposition values do, in fact, vary as a function of Z^2.

Table 3. Mean and most probable energy deposition in 1 μm thick water slabs. The ions had either 100 keV um^{-1} stopping power or 600 MeV n^{-1} kinetic energy.

Ion	Be-8	C-12	O-16	Mg-24	Si-28	Ca-40	Ti-48
100 keV μm^{-1} Mean Value	99.07	99.38	99.69	100.29	100.21	98.35	94.26
100 keV μm^{-1} Most Probable Value	99.07	90.91	86.42	82.15	80.09	76.14	72.37
600 MeV n^{-1} Mean Value	3.96	9.01	15.97	36.08	49.05	100.48	121.46
600 MeV n^{-1} Most Probable Value	2.69	6.2	11.38	26.27	36.98	79.08	99.34

Figures 9 and 10 describe the energy lost by charged particles traversing water, but this is not the entire picture. Ion interactions in the target produce secondary radiations that do not necessarily deposit their kinetic energy at the point of production. Much of this energy can be transferred to delta rays that can escape the target, reducing the local dose. The FLUKA code allows the user to simulate secondary electron tracks following the collisions that make up the LET values shown above. Many dose readings, at increasing depth, were taken to study the buildup of delta rays towards an equilibrium state. This state occurs when the delta rays that escape out of the downstream face of the target are replaced by delta rays coming in from the upstream face. Delta-ray equilibrium is established based upon the primary ion velocity but requires significantly less depth than predicted by the highest energy delta ray.

When the highly energetic delta rays escape the thin 1 μm target slab, the energy that is deposited locally shows a different trend. Figures 11 and 12 show the energy deposition curves for Si-28 and O-16 traversing multiple target thicknesses. To recapture the energy lost to delta rays, targets are placed deeper inside the water medium, allowing for delta-ray buildup. The data are presented with the stopping power curves discussed earlier. The other curves show the significant change in local energy deposition that occurs when delta-ray buildup is accounted for. The electrons produced in the very large collisions no longer deposit all of their energy within 1 μm.

At increasing depth in a water medium, the target slabs receive an increasing amount of delta-ray buildup, which eventually reaches equilibrium. Increased depths display more high-energy events than the 0-1 μm depth, meaning delta rays that are created at shallow depths deposit their energy deeper into the target. The curve never completely resembles the stopping power curve at high energies because secondaries produced in these high-energy reactions are very rare and have widely varying ranges.

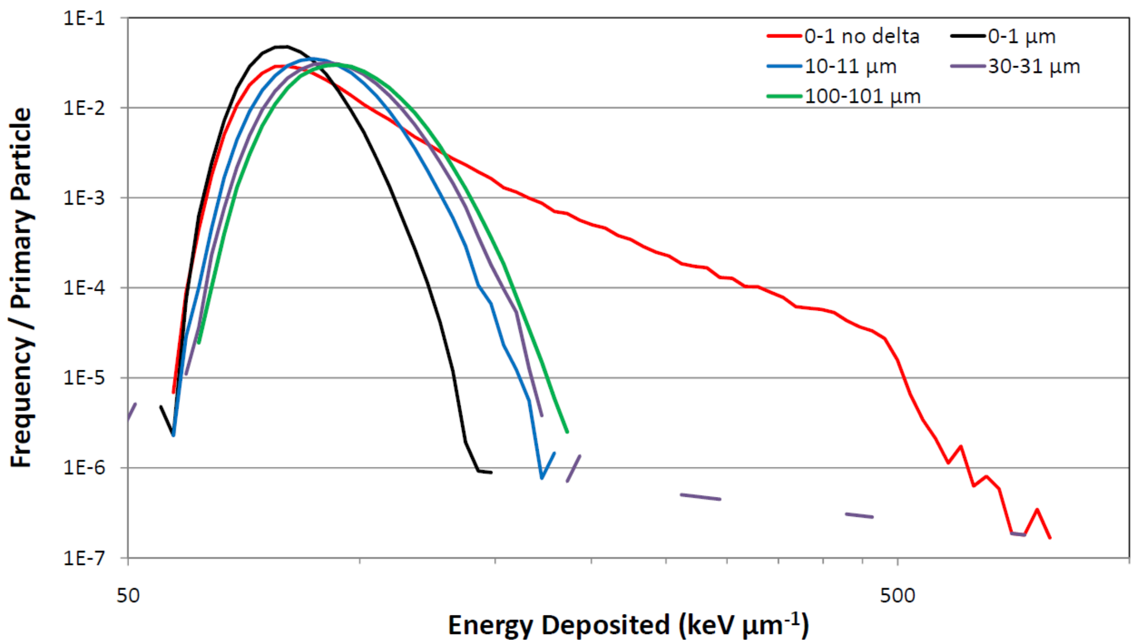

Figure 11. Si-28 ion traversing 1 µm thick target slabs at increasing depth in water medium. The ion had a calculated stopping power of 100 keV um^{-1}. The curves represent the frequency of total energy deposition by individual particles averaged over the total number of particles simulated. Different curves represent different depths of the target slab to detail delta-ray buildup.

In Figure 12, the O-16 ion appears to have reached delta-ray equilibrium by 50 µm depth, while the Si-28 ion, in Figure 11 hasn't reached delta-ray equilibrium at 100 µm depth. The higher velocity Si-28 ion requires larger depths to reach delta-ray equilibrium.

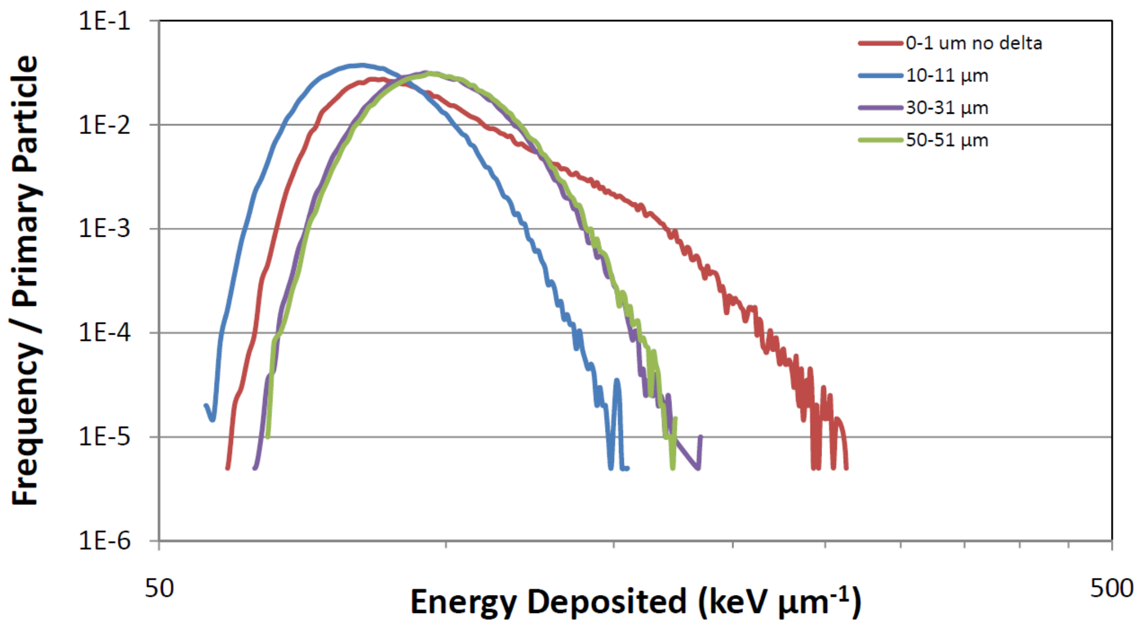

Figure 12. O-16 ion traversing 1 µm thick target slabs at increasing depth in water medium. The ion has a stopping power of 100 keV um^{-1}. The curves represent the frequency of total energy deposition by individual particles averaged over the total number of particles simulated. Different curves represent different depths of the target slab to detail delta-ray buildup.

Table 4 describes the energy deposited in 1 µm thick slabs at increasing depths by the ions having 100 keV µm^{-1} stopping power. Higher velocity ions require significantly thicker targets to achieve delta ray-equilibrium. The Be-8 ion exhibits a lower LET value in FLUKA data than calculated by the Bethe-Bloch approach. The curves in Figures 11 and 12 do show that energy deposition trends reach equilibrium after much less target depth than predicted by the range of the highest energy delta ray. The Si-28 ions reach this point around 100 µm, while O-16 ions do by 50 µm depth.

Table 4. Energy deposition, accounting for delta-ray escape, for ions having equal stopping powers of 100 keV um^{-1}. Maximum energy delta rays, and their range, are displayed and depend on the kinetic energy of the primary particle.

Ion	MeV n^{-1}	Max Energy Delta (keV)	Range in H2O (µm)	Energy Deposited (keV) in 1 µm slabs 0-1	10-11	20-21	30-31
Be-8	6.8	14.86	5.15	84.22	91.56	90.28	91.55
C-12	18.48	40.63	29.2	87.44	98.55	99.87	100.92
O-16	37.52	83.31	98	84.88	95.32	97.22	99.51
Mg-24	106.27	244.4	640	82.08	91.18	92.83	95.3
Si-28	164	388.2	1200	80.64	89.37	90.85	93.43
Ca-40	631.5	1837	7000	77.22	84.93	86.07	88.61
Ti-48	1582	6345	32000	74.16	81.05	82.2	84.56

As seen in Figure 10, energy deposition spectra exhibited similar shapes and trends for ions of equal velocity when delta rays were not transported. The differences in LET were due to increased production of ionizations that are a function of Z^2. When delta rays were transported, the effect of delta-ray loss affected the energy deposition trends experienced by ions of equal velocity. Figure 13 displays those trends as the ions traversed a 1 µm slab at 30 µm depth in water.

Each energy deposition value consists of the total energy deposited by a single ion, averaged over the total number of ions simulated. The energy deposition value is dependent on the charge of the primary particle, so lower charge ions deposit less energy. As shown in Figure 13, lower charge ions also experience the very-high energy deposition events when high-energy delta rays are produced.

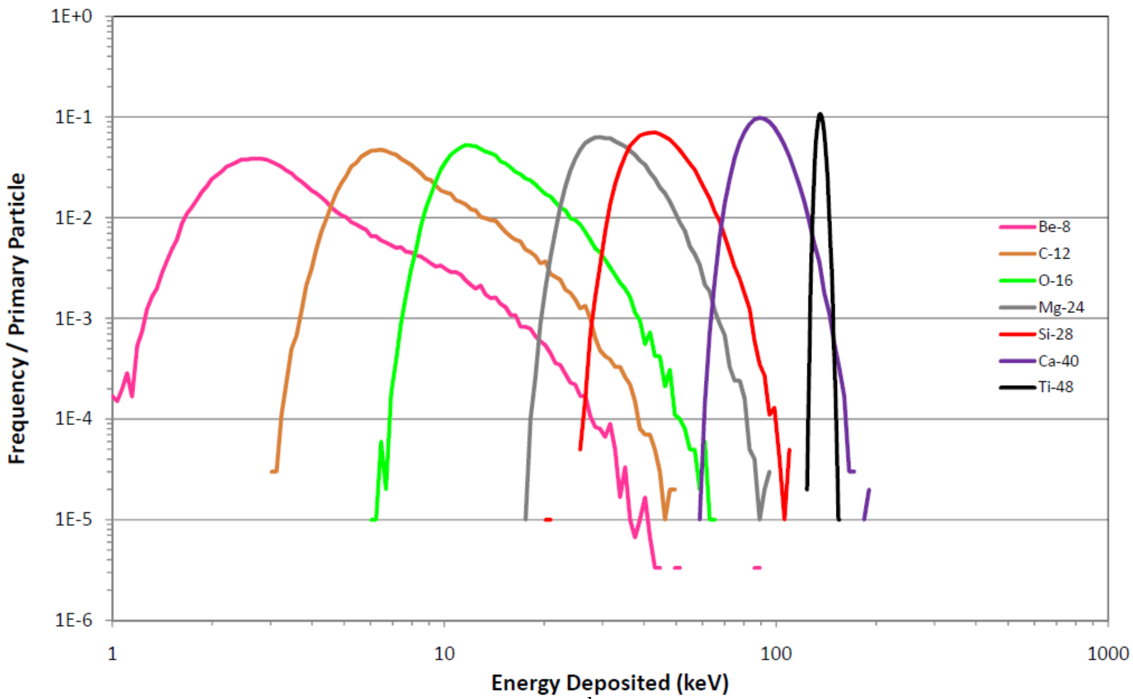

Figure 13. Energy deposition by 600 MeV n^{-1} (equal velocity) ions traversing 1 µm thick target slabs at 30 µm depth in water medium. The curves represent the frequency of total energy deposition by individual particles averaged over the total number of particles simulated. Different curves represent different ions traversing the target slab.

Delta-ray kinetic energy can be calculated, as discussed earlier, or it can be scored along with particle fluence in the FLUKA simulation. Energy fluence is scored by the number of electrons crossing a cylindrical boundary parallel and surrounding the ion track. Figure 14 displays the frequency of an electron with a corresponding kinetic energy crossing a 5 nm radius water cylinder, 1 µm long. The Ti-48 ions, having the highest charge and velocity, create more delta rays that can extend to higher kinetic energies. The maximum energy delta rays for each ion are described by the cut-off values, of each curve, seen in Figure 14.

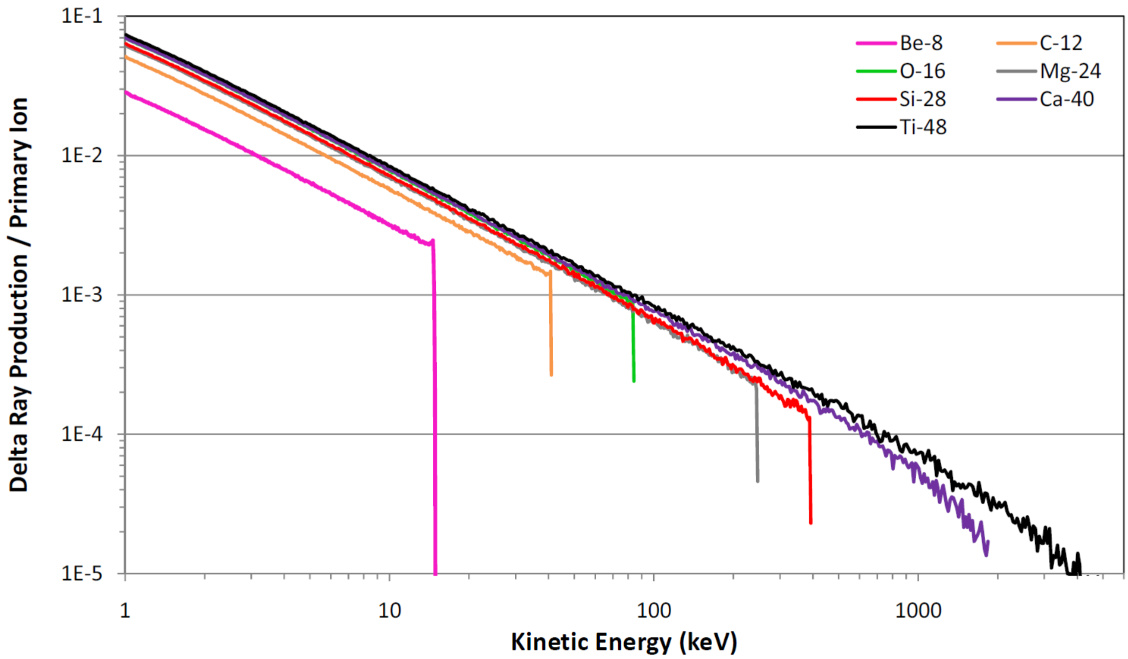

Figure 14. Delta-ray production and their corresponding kinetic energy for ions having equal stopping powers of 100 keV um^{-1}.

When velocity is equal, variations in delta-ray production depend only on the primary ion charge. Figure 15 describes the effect of effective charge on delta-ray production. Ions of different charge, but equal velocity, have different ranges in target media. The ions depicted in Figure 15 have sufficient velocity that stopping power and range do not vary significantly over target thickness.

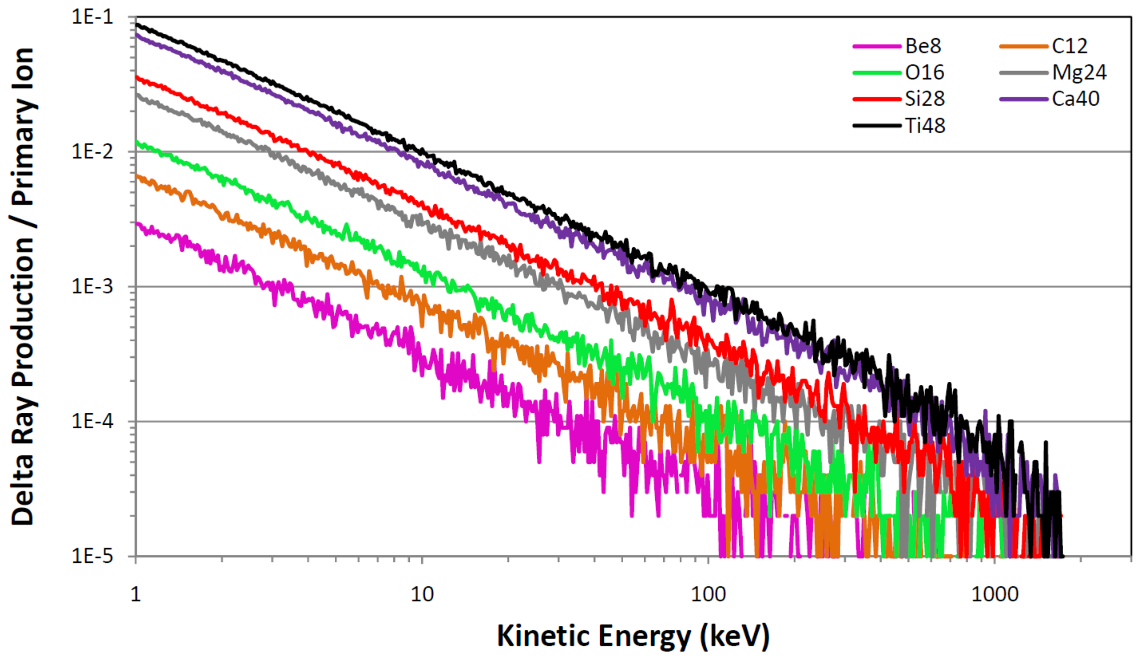

Figure 15. Delta-ray production and their corresponding kinetic energy for equal velocity ions at 600 MeV n^{-1}.

Looking back to the delta-ray distribution formula proposed by Katz (1967), delta-ray production can be calculated for any of the ions considered in this research. Figure 16 shows a comparison of the simulated data to Katz theory for delta-ray production from an Si-28 ion at 164 MeV n^{-1}. There is some deviation at energies below about 4 keV, and the FLUKA code does not track electrons below 1 keV. Part of the difference may be due to the fact that the FLUKA model is scoring electrons that have traversed at least 5 nm radially outward from the ion, while the Katz formula includes all electrons produced by the traversing ion. The curves do match for energies above ~ 4 keV.

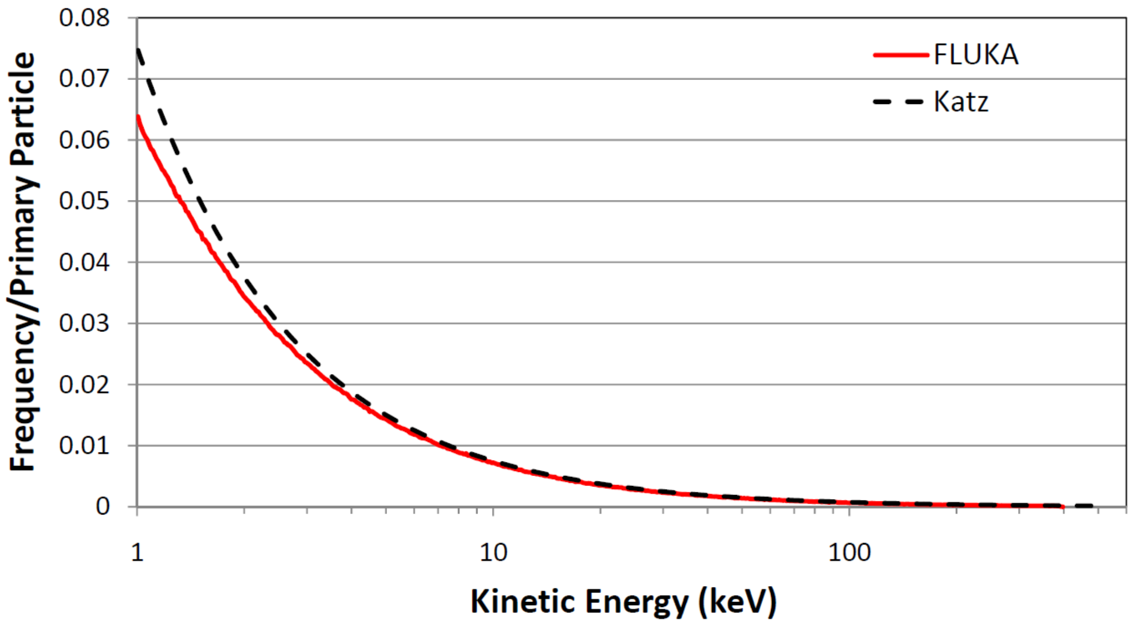

Figure 16. Delta-ray production for 100 keV μm^{-1} stopping power Si-28 ion predicted by FLUKA simulation (—) and the Katz equation (- - - -).

The lower the electron kinetic energy, the more tortuous its track. Lower-energy electrons are also emitted at a larger angle to the ion path. These delta rays come off at nearly a 90-degree angle but do not follow straight paths. Higher-energy electrons are more forward directed, with straighter paths until they slow down.

To further investigate the necessary delta-ray buildup depth, ions were simulated to traverse a 1 mm thick water target. Figure 17 displays the mean energy deposited in 1 μm slabs at increasing depth. It is apparent that the energy deposited per micrometer by Ca-40 and Ti-48 ions never achieve the calculated stopping power of 100 keV μm^{-1} in a 1 mm thick water target. In fact, the FLUKA-simulated LET without delta-ray loss were 94.26 and 98.35 for Ti-48 and Ca-40, respectively, so there is some discrepancy between the calculation and Monte Carlo simulation. The Be-8 ion stops in the target and the C-

12 ion reaches a much higher stopping power, so neither are included to provide a clear view of the other ion LET values.

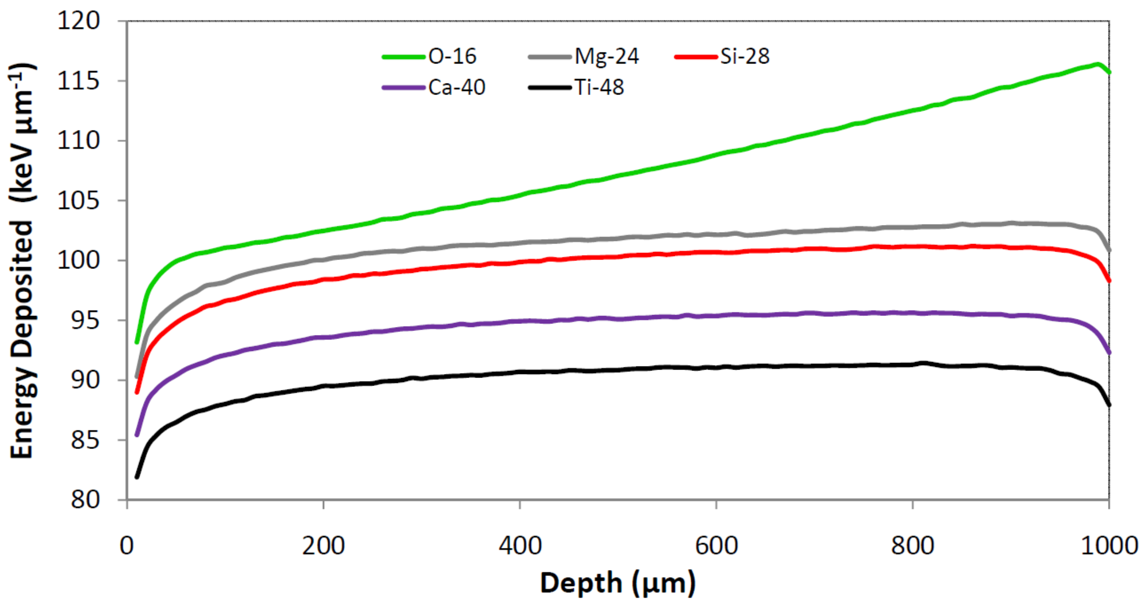

Figure 17. LET as a function of depth in a 1 mm thick water target. The stopping power of the ions were calculated to be 100 keV μm^{-1} in water.

Realistically, the Ca-40 and Ti-48 ions do not deposit their maximum energy loss value within 1 mm of water because a small portion of their delta rays can travel a millimeter, or more, in water. Since the medium surrounding the target is a vacuum, the curves tail downwards at the exit face of the target because there is no back-scattering of delta rays. Exit stopping powers (following 1 mm of water) are listed in Table 5 for both ions of equal stopping power and separately, for ions of equal velocity. The Be-8 ion stops at about 300 µm depth in the target. The stopping power values in Table 5 describe the effect of the ion slowing down and increasing its LET as it penetrates matter.

Table 5. Calculated stopping power as the ion exits the 1 mm thick water target.

Ion	Be-8	C-12	O-16	Mg-24	Si-28	Ca-40	Ti-48
100 keV um^{-1} ions	0	216.21	117.84	103.11	101.55	100.14	100.01
600 MeV n^{-1} ions	4.12	9.28	16.5	37.13	50.55	103.2	124.88

The increase in LET is primarily concentrated in the small core region surrounding the primary, and the only change in the penumbra is due to decreased velocity and effective charge. For this target thickness, the higher velocity ions are affected less, and the increase in dose is actually due to delta-ray buildup. The stopping power for equal velocity ions does not vary at the same rate, largely due to the ion charge, but also because of variations in the amount of energy being deposited by delta rays. Changing LET is incidental to laboratory experimentation so it is included in this study to promote a more realistic approach.

Radial Dose Profiles

After discussing the characteristics of energy deposition and secondary electron generation longitudinally along the ion path, the next step is to analyze the dose deposited radially. To compare the FLUKA geometry with the amorphous track model, delta-ray equilibrium must be established. By setting the target slab at a depth dependent on the buildup depths described earlier, delta-ray equilibrium is satisfied. Unfortunately, as depth increases, the primary ion tends to scatter away from its initial trajectory. At 10 µm depth, a primary ion scattering over 5 nm radially (out of the innermost shell) represents more than a 0.0005 degree scatter. This is extremely small, but creates errors in the radial dose results at small radii. To account for this, events are only scored when the ion leaves the rear of the 5 nm radius target shell (meaning it remained within that shell for its entire track). This method simulates the common experimental practice of requiring coincidence with an exit-detector pulse. The FLUKA USERBDX input option scores the forward fluence of particles crossing the downstream boundary for each cylindrical shell. Ions that exit shells other than the 5 nm radius must be subtracted from the radial dose analysis because they impart their core regions and penumbras in the wrong place. This process was applied to generate the data in Figure 18, so only the ions that actually exit out the rear of the 5 nm cylinder are scored. The radial dose profiles deposited by ions of 100 keV μm^{-1} are presented in Figure 18 and extend over many orders of magnitude.

The trends are similar, and are difficult to distinguish on a log-log plot. The effects of increased radial distance are evident at large radii, greater than about 5 µm. A 5 µm radius is also the approximate distance where delta-ray buildup and target thickness become significant factors. Scattering effects are more noticeable for the slower ions, although they require less delta-ray buildup depth. The dose profiles described above are at different depths, corresponding to the necessary buildup depth for the individual ion.

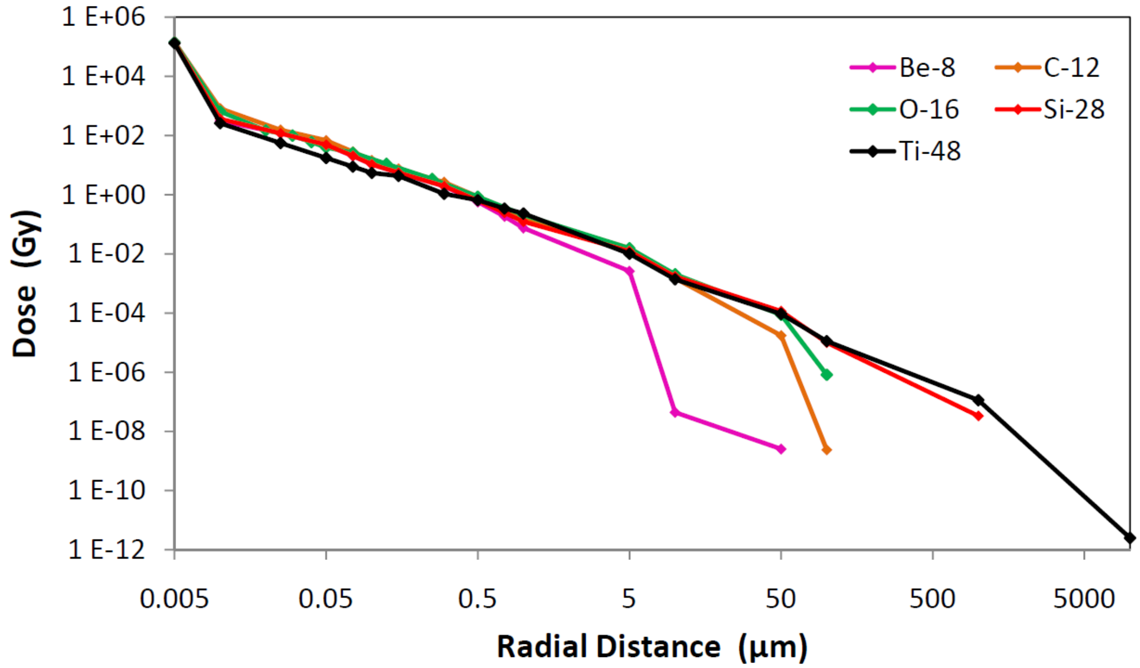

Figure 18. Dose as a function of radial distance away from the primary ion track for 100 keV µm^{-1} stopping power ions. Data points describe the dose in each cylindrical shell modeled in the FLUKA geometry. Target slab depth is located at the minimum depth required for delta-ray equilibrium corresponding to the velocity of each ion.

Radial dose ranges over many orders of magnitude, so an easier way to view the information is by the percent of the total dose that is deposited within a certain radial distance. Figure 19 displays the percent of total radial dose deposited vs. radial distance of predicted by the Chatterjee model (Chatterjee and Schaefer 1976) compared to that predicted in cylindrical shells modeled using the FLUKA code. These results represent ions with 100 keV um^{-1} stopping power.

The slower moving ions deposit more energy within small radii and less at large radii. Were the data to extend below 1 keV delta rays, the percent dose at 5 to 10 nm would probably be lower and more similar to the Chatterjee data. Those electrons may have enough range to travel outside a 10 nm radius, reducing the core dose and depositing energy at larger radii. Most of the ions are not depositing 100% of their dose in the 1 micron slab, describing energy lost to delta rays escaping the target. This reduced dose is partly dependent on the depth of the target slab as described earlier in the section discussing delta-ray buildup. It also depends on the energy deposition trends previously discussed.

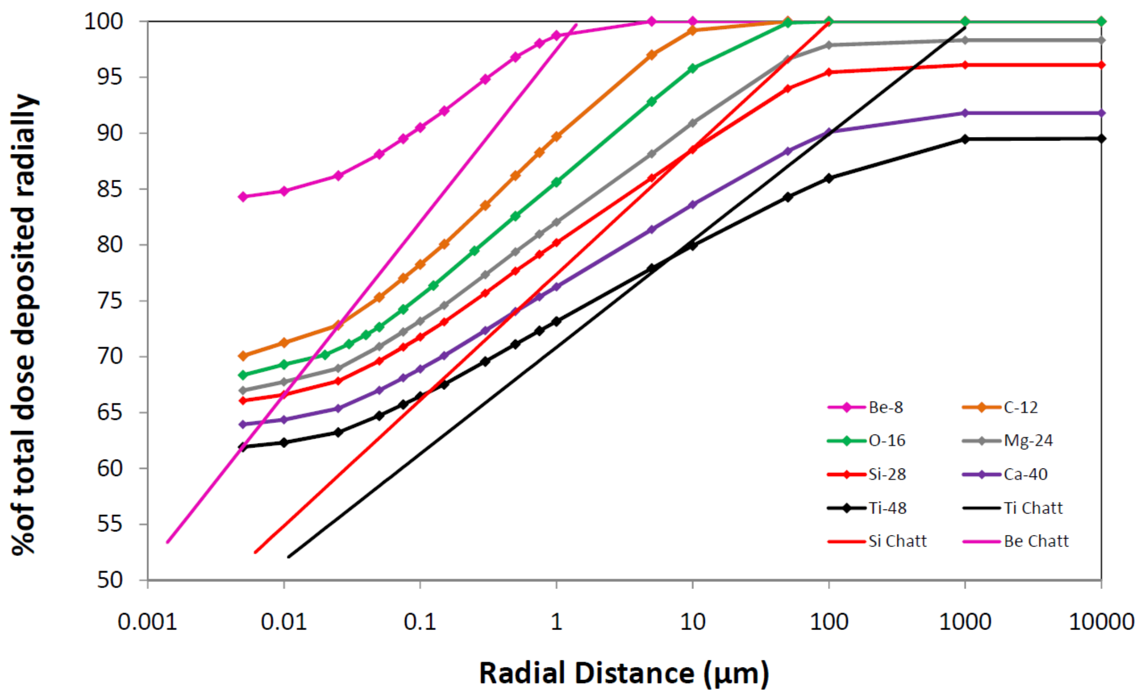

Figure 19. Percent radial dose as a function of radial distance away from the primary ion track of ions with equal stopping power of 100 keV μm^{-1} in water. Chatterjee data are presented for Be-8, Si-28, and Ti-48 ions. For the FLUKA-simulated data, data points represent the percent of dose deposited within that cylindrical shell radius.

These dose profiles contain energy deposition spectra for several hundred thousand particle traversals through the same target orientation. The reason delta-ray equilibrium is not established at large radii is because the highest energy delta rays require significant buildup depths relative to the amount of scattering undergone by the primary particle. Simulating radial dose for that depth would reduce the accuracy of measurements at small radii where dose is much more significant compared to the outer radii. The FLUKA trends are not the same as the Chatterjee trends, but they do appear to have about the same maximum penumbra radii.

The radial dose plots in Figures 18 and 19 display data at a point within the target delta-ray equilibrium exists within the penumbra radius determined by the Chatterjee approach. Increases in stopping power are negligible, but there has been adequate depth for delta ray buildup within the 5 μm radius. The higher velocity ions have been allowed thicker buildup targets because their LET and angular scatter are affected less.

Estimating probabilities for DNA target hits is not possible to simulate with this model, due to the delta-ray energy cutoff in the FLUKA code. However, dose deposited across the cell, and into neighboring cells, can be modeled effectively. Figure 20 presents the radial dose on a narrower scale – the radial dose at 50 nm to 5 μm for 100 keV μm^{-1} ions. Electrons with kinetic energies below 1 keV do not travel much farther than 50 nm in water, so their absence in the FLUKA simulation should not skew the data presented in this plot. Were the ion to cross the middle of a cell nucleus, the radial distance scale displayed in Figure 20 depicts the penumbra dose across that cell nucleus. The lighter ions deposit the larger dose across that distance.

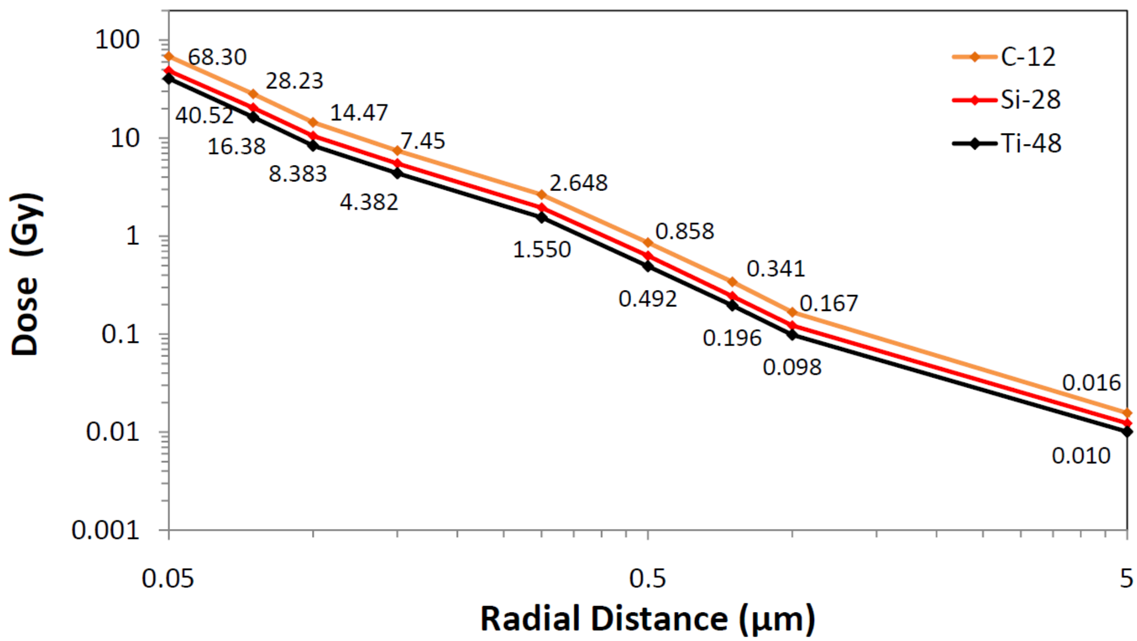

Figure 20. Dose as a function of radial distance away from the primary ion track. Ions displayed have equal stopping power of 100 keV µm^{-1} in water. Data points represent the dose deposited in cylindrical shells surrounding the primary ion path for the C-12 and Ti-48 ions.

The trend in Figure 20 describes how ions of equal stopping power, but different velocity, transition toward a region where the radial dose is equal. Dose at 50 nm radii is significantly different, while dose a 5 µm is more similar. The doses for the lighter ions tail off, while the penumbrae of the heavier (and faster) ions extend outward much farther, but at very low dose – a region describing rare, but large radial distance effects. Within a 10 µm diameter is truly the region of interest for this dose model. Inside 0.05 µm, the dose is dominated by the primary ion and its short-range delta rays, while outside 10 µm, events are rare and diffuse.

Figure 21 describes the effect of delta-ray buildup in the radial dose model. High-energy electrons are very forward directed with relatively straight paths, but the chance of them re-entering the narrow shell regions is very small. Correspondingly, delta-ray buildup only affects the larger radial volumes.

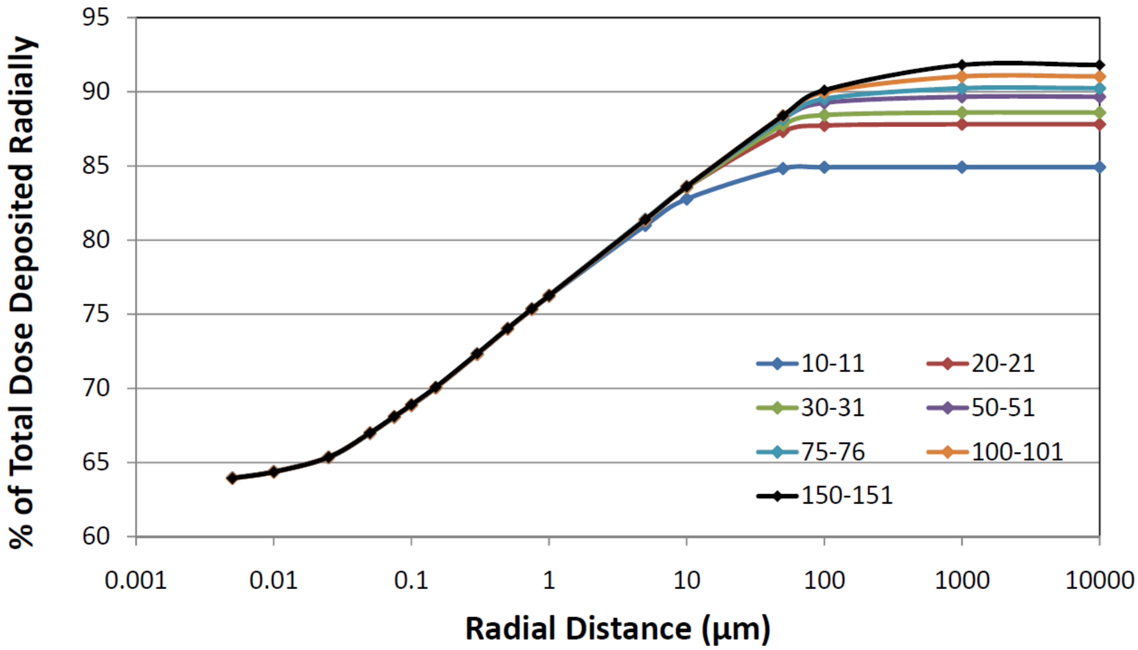

Figure 21. Percent radial dose as a function of radial distance away from the primary ion track for 100 keV µm^{-1} stopping power Ca-40 ions at increasing depth in water. Data points represent the dose deposited in cylindrical shells surrounding the primary ion path. Separate curves represent different target depths inside a water medium.

The trend in Figure 21 emphasizes that delta-ray buildup is primarily an effect measured above 10 µm away from the ion track, describing regions outside a cell nucleus diameter. The inner cylindrical volumes are so small, it is rare for a scattered particle to come from outside and deposit any significant amount of energy. As target depth increases, the primary ions tends to scatter outside of the 5 nm radius shell. These scattering events must be subtracted from the FLUKA data and more primary particles must be simulated to achieve adequate statistics.

Ions of equal velocity exhibit the same radial dose trends, only at different magnitudes, due only to the effect of Z^2. In Figure 22, Ti-48 ion dose is seen beyond 1000 µm, and describes a statistical effect due to the larger number of delta rays that are produced.

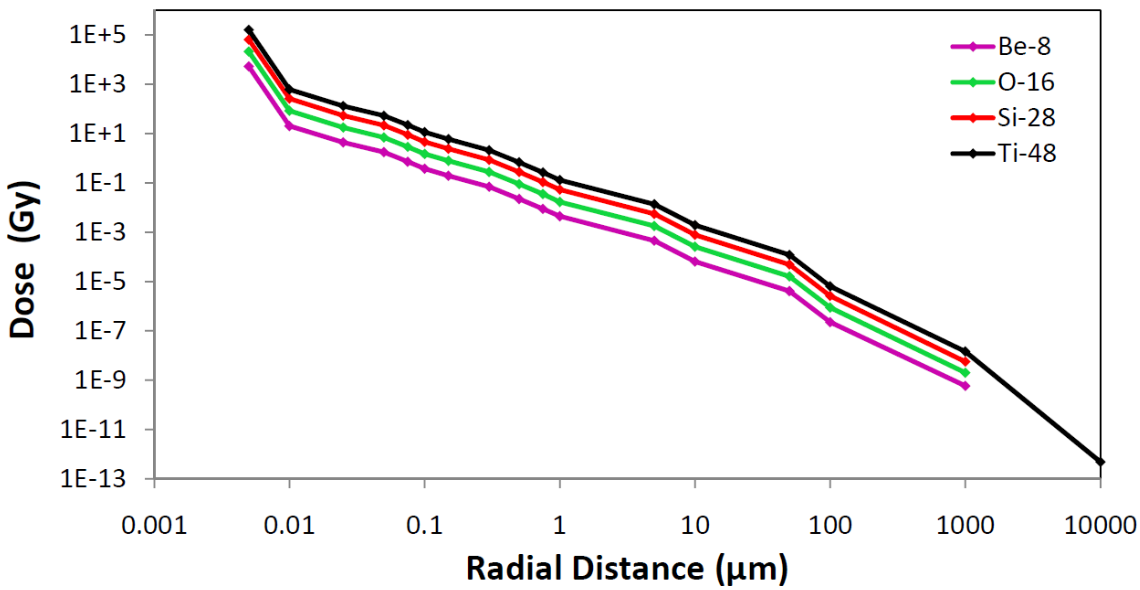

Figure 22. Dose as a function of radial distance away from the primary ion track for equal velocity ions at 600 MeV n^{-1}. Data points represent the dose deposited in cylindrical shells surrounding the primary ion path.

Figure 23 displays the percent of the total dose deposited within a radial distance by ions with equal velocity. The trends are the same because the ions produce delta rays with the same kinetic energies. Therefore, the same percentage of an ion dose is deposited along the radial distance, regardless of charge.

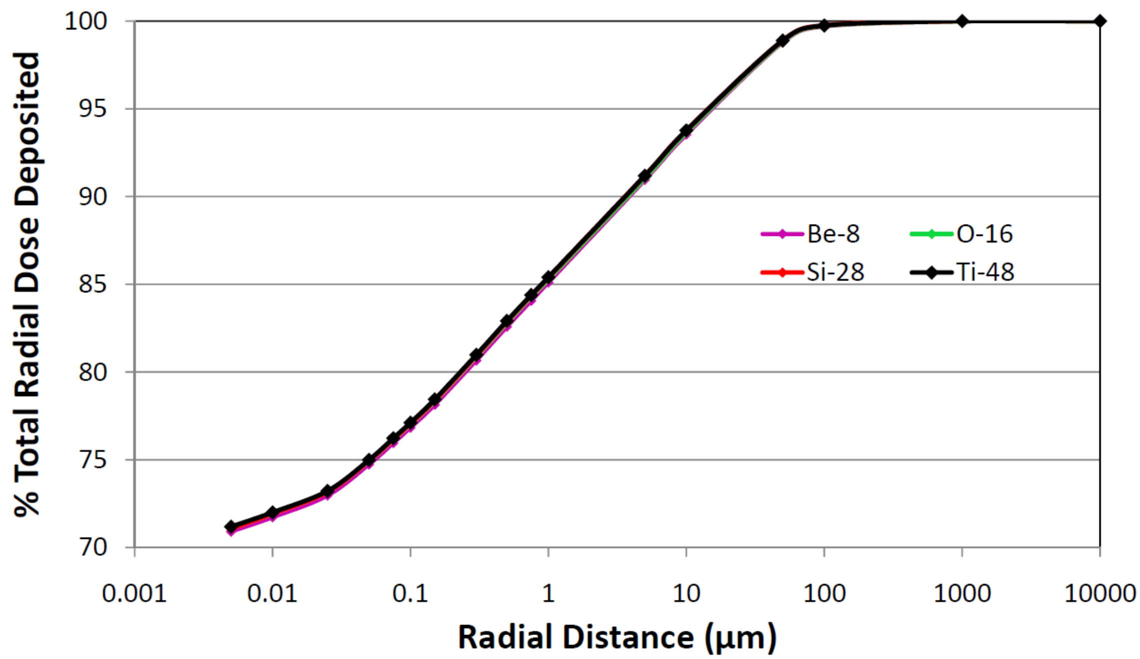

Figure 23. Percent radial dose as a function of radial distance away from the primary ion track for equal velocity ions at 600 MeV n^{-1}. Data points represent the dose deposited in cylindrical shells surrounding the primary ion path.

To keep this study focused on relative damaging ability, particle fluence is also scored for electrons crossing from inner shell regions to outer regions. The trend is seen in Figures 24, 25, and 26 that the low-energy electrons stop within smaller radii because they have shorter range. High-energy delta rays do not create enough low-energy delta rays to maintain the energy spectrum.

Figure 24 displays the number of delta rays traveling outward from the primary track at increasing radii. The lower-energy electrons obviously do not travel as far, as seen by the decreasing trend at lower energies. This spectrum is similar for the different ions, and only Si-28 is depicted here. Ca-40 and Ti-48 ions produce higher-energy electrons that travel farther than the 50 µm radius seen here.

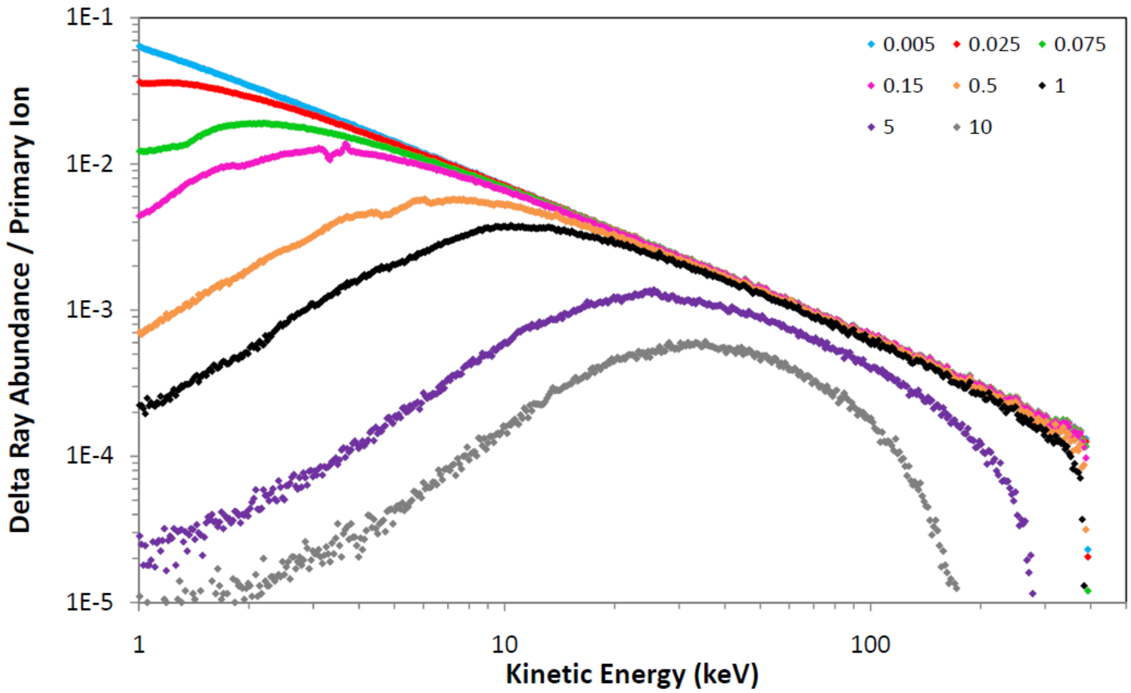

Figure 24. Frequence of delta rays crossing the surface of shell detectors with increasing radii for the Si-28 ion with 100 keV μm^{-1} stopping power. The shell radii have dimensions of microns.

Taking the same measurements, four ions are plotted in relation to each other at 75 nm and 250 nm radii in Figures 25 and 26. Delta-ray abundance for energies below 2 keV is significantly reduced between 75 and 250 nm, signifying the extent of their range. Very high-energy delta rays of a few MeV are produced by the Ti-48 ion. Those delta rays exhibit less reduction in abundance at these small radii compared to those produced by a slower-moving ion. As delta rays traverse the water medium, they slow down and can generate small populations of tertiary delta rays. The Be-8 ion data show that there remains are very small population of delta rays between 15 and 20 keV. This trend also appears for the O-16 ion above about 80 keV.

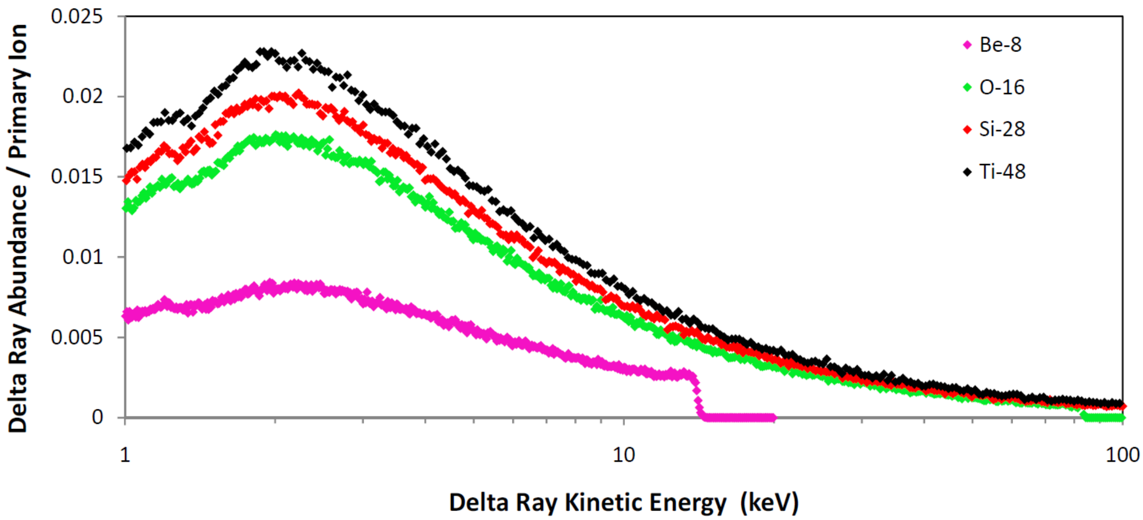

Figure 25. Frequence of delta rays crossing the shell detector at 75 nm radius for ions with 100 keV μm^{-1} stopping powers. Lower-velocity ions produce delta rays with smaller kinetic energy and range.

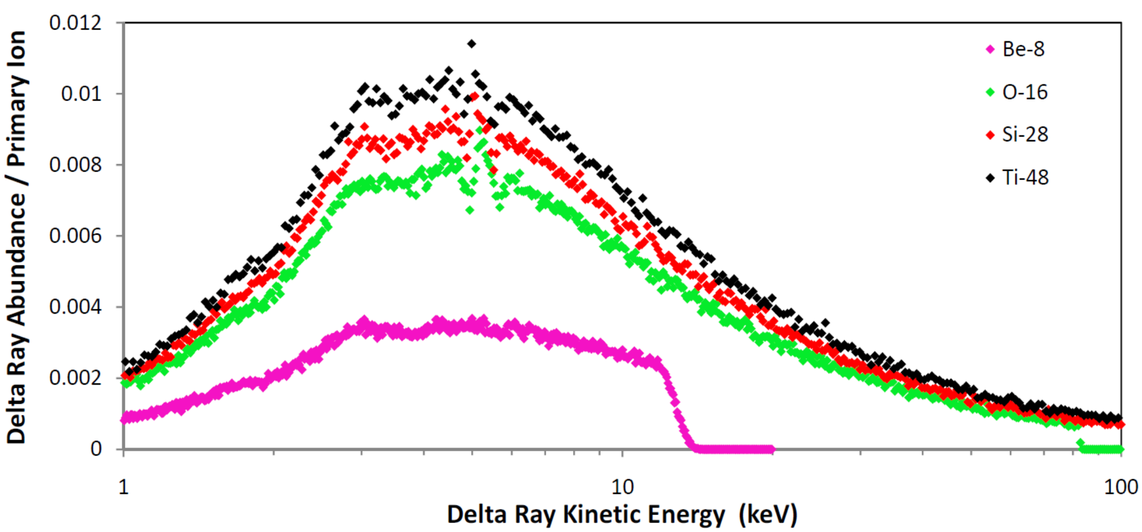

Figure 26. Frequence of delta rays crossing the shell detector at 250 nm for ions with 100 keV μm^{-1} stopping powers. Lower-velocity ions produce delta rays with smaller kinetic energy and range.

Table 6 displays the dose deposited by delta rays in cylindrical shells for radii from outside 1 µm up to 10 mm. The shell with a 5 µm radius contains the dose between 1 and 5 μm. For ions with equal stopping powers, higher velocity is shown to produce higher doses at large radii.

Table 6. Penumbra dose for ions with 100 keV μm^{-1} stopping powers scored in cylindrical shells of different radii outside 1 μm radius. The maximum dose for each radial distance is displayed in bold font.

Radial Distance (μm)	10000	1000	100	50	10	5
Electron Dose (Gy)						
Be-8	0	6.994E-13	5.226E-10	9.997E-09	4.281E-07	2.091E-02
C-12	0	4.648E-12	9.151E-10	4.046E-05	5.852E-03	1.124E-01
O-16	0	8.922E-12	1.492E-07	1.346E-04	8.801E-03	**1.169E-01**
Mg-24	0	6.738E-10	2.274E-06	2.629E-04	1.108E-02	1.092E-01
Si-28	0	1.715E-09	3.783E-06	3.057E-04	**1.132E-02**	1.051E-01
Ca-40	0	7.000E-09	7.759E-06	**3.656E-04**	1.108E-02	9.472E-02
Ti-48	0	**9.301E-09**	**8.655E-06**	3.587E-04	1.033E-02	8.611E-02

Lower velocity ions produce narrower penumbrae. Table 7 displays dose deposited in cylindrical shells for radii inside of 1 μm. All ions impart significantly higher doses in the smaller shell volumes. Table 7 shows that the C-12 ion dominates the radial dose within 1 μm radii. The Be-8 ion is experiencing the end of its track, so secondary electrons have very small ranges. The 5 nm radius shell absorbs a smaller dose from the Be-8 ion compared to the C-12 ion, describing an inconsistency between the FLUKA code calculations compared with the Bethe-Bloch approach for energy loss as well as the Chatterjee trends. Excluding the Be-8 ion, for ions of equal stopping power, radial dose decreases with increasing primary ion velocity inside a 1 μm radius.

Table 7. Penumbra dose for ions with 100 keV μm^{-1} stopping powers scored in cylindrical shells of different radii inside 1 μm radius. The maximum dose for each radial distance is displayed in bold font.

Radial Distance (μm)	1	0.75	0.5	0.3	0.15	0.1	0.05	0.025	0.01	0.005
Electron Dose (Gy)										
Be-8	0.76	1.91	5.71	18.82	52.67	101.04	456.62	1127.94	3177.87	4370.71
C-12	**1.57**	**3.26**	**8.33**	**25.92**	**72.81**	**140.45**	**673.51**	**1500.39**	**4350.59**	**5663.77**
O-16	1.39	2.88	7.35	22.93	64.65	124.39	602.21	1298.49	3984.53	5331.85
Mg-24	1.22	2.51	6.40	19.99	56.38	108.30	526.83	1118.97	3517.89	4743.99
Si-28	1.16	2.39	6.10	19.04	53.79	103.27	483.71	1133.85	3360.43	4505.65
Ca-40	1.02	2.10	5.35	16.72	47.12	90.52	440.53	929.59	2944.71	3968.51
Ti-48	0.93	1.90	4.84	15.14	42.69	81.94	399.04	840.89	2667.54	3592.54

Without knowing actual target hits, it is difficult to relate radial dose information to realistic damage. The delta-ray kinetic-energy spectra were determined to follow similar trends, and high-energy events are very unlikely. As radial distance increases, the dominating penumbra dose shifts toward the higher velocity ions. This dose value is largely dependent on the velocity of the ion, while the full target geometry plays a part as well. C-12 ions dominate the radial dose within a 1 μm radius.

The FLUKA-simulated radial dose model is effective for understanding the general trends of delta rays and describes the influence of primary ion charge and velocity. Unfortunately, it does not provide enough information for determining physical damage to biologically relevant targets, especially for single-ion traversals. The number of delta rays crossing each cylindrical region surrounding the ion trajectory and the corresponding energy that they deposit determine the ionizations that will be imparted to sensitive targets. Of the radial dose trends discussed here, several challenges to the accuracy of the simulation have arisen, including primary ion scatter, delta-ray buildup, and stopping power increasing across target depth. To address these shortfalls, additional target geometries must be simulated.

Mesh Geometry Analysis

To effectively demonstrate how a track structure realistically affects nearby targets, a set geometry must be utilized to provide microdosimetry information. Target dose and hits can be determined by simulating a water geometry housing many adjacent, small detectors. The mesh cube geometry consists of 1 million cube-shaped voxels with edges of 10 μm that make up a large cube having edges of 1 mm. The mesh cylinder is housed inside the volume of one 10 μm voxel. It provides dosimetry analysis for one million (nearly) cube-shaped voxels with edges of 10 nm that make up a cylinder with a 5 μm radius and 10 μm length. The goal is to establish cell-damage probabilities based on dose and particle fluence accounting for each individual target. Measurements include the buildup of secondary particles, primary ion scatter, and to a lesser extent – fragmentation. Radial dosimetry around the ion track can also be performed. The geometry is small enough not to lose site of the track structure approach to still be able to discriminate the different energy deposition spectra and their spatial distributions.

The FLUKA code simulates the primary ion traversing the middle of a voxel contained near the center of the mesh geometry. The code records energy deposited and particle fluence for each voxel following each event. This particle is simulated through the same point and axis 200,000 times to improve the statistics and develop trends for each ion and irradiation scenario. Dose and particle fluence events for each voxel are cumulative over the 200,000 particle traversals and the resulting output data are presented as total dose or fluence divided by the 200,000 primary particles simulated. As trends are established for each ion, results can be compared by normalizing values with respect to the total energy they deposit in the target per primary ion. In order to establish damaging ability of these ions, the damage to surrounding targets is analyzed with respect to dose and particle traversals. Figure 27 describes the population of voxels, within the entire 1 mm^3 target, that receive a dose corresponding to the abscissa value.

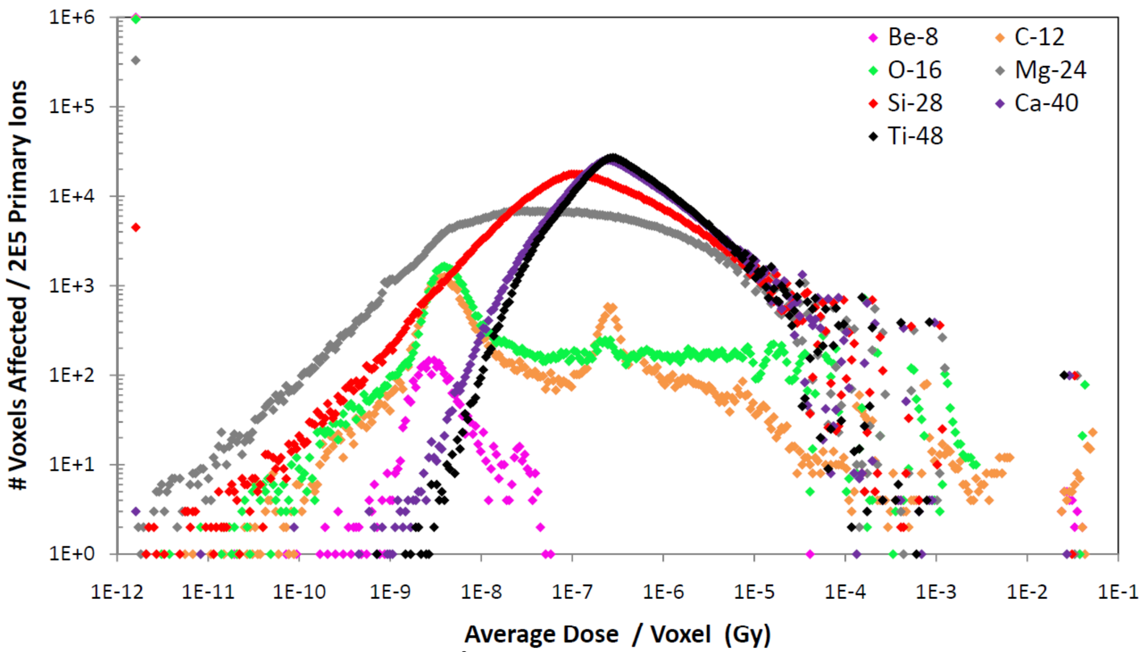

Figure 27. Population of 1,000 μm^3 targets receiving a dose in the mesh cube geometry by ions with 100 keV μm^{-1} stopping powers. Dose is presented as a trend that is averaged over the events produced by 200,000 primary particles traversing the geometry. Single primary-ion events produce many zero dose values making the average values orders of magnitude lower. Individual primary ion events would be seen as only a few, random, data points.

Dose represents the energy deposited by secondary electrons averaged over 200,000 primary ion traversals. For single primary ion traversals, most voxels are unaffected, so the final average value includes these zero values. Therefore, the dose appears orders of magnitude less than what is actually experienced by a voxel when it is hit. The very high dose values signify the targets that are traversed by the primary ion. For targets not traversed by the primary ion, this plot displays a more significant electron dose coming from the higher velocity ions. Multiple high-dose points represent scattering of the primary particle. The lowest dose events that affect a very high number of targets represent targets that receive zero (or very near to zero) dose. This means that zero, or one, electrons interacted in this voxel following 200,000 simulations. These voxels are assumed to be un-hit targets. This plot was generated from a histogram of target events, described by the data located in Appendix B. The lowest dose bin ranges from $0 – 1 \times 10^{-12}$ and contains the zero dose voxels. Excluding primary ion tracks, the Ti-48 ion affects the most targets with the highest doses. Ca-40 and Ti-48 are seen to affect the largest number of targets, with very similar trends. The high-dose data points are dispersed for C-12 due to the large amount of scattering it experiences when traversing 1 mm of water. The higher-velocity ions scatter less, and therefore, display only one, or a few, high dose data points. Decreasing Z and velocity decreases the abundance and range of the delta rays, so fewer targets are affected. To better visualize the trend, Figure 28 displays the effects of ions with equal velocity. As already established, they have very similar trends, with a simple increase in magnitude due to charge. In both plots, there are more un-hit targets for lower Z ion traversals, signifying decreased delta-ray production.

There is a clear distinction of 100 targets receiving primary ion doses seen in Figure 28 that is not as apparent for the equal stopping power ions in Figure 27. As detailed in Appendix B, the highest energy events do sum to 100 for each different ion, describing that the 1 mm thick target is 100 voxels thick. In Figure 28, there are two data points representing primary particle dose from Ti-48. This is an effect of the binning structure, as the edge of the high dose bin lies very near the corresponding primary track dose for the ion. For equal velocity ions, the number of targets affected at any dose is proportional to Z^2. For single primary ion traversals, most voxels are unaffected, so the final average value includes these zero values. Therefore, the dose appears orders of magnitude less than what is actually experienced by a hit voxel.

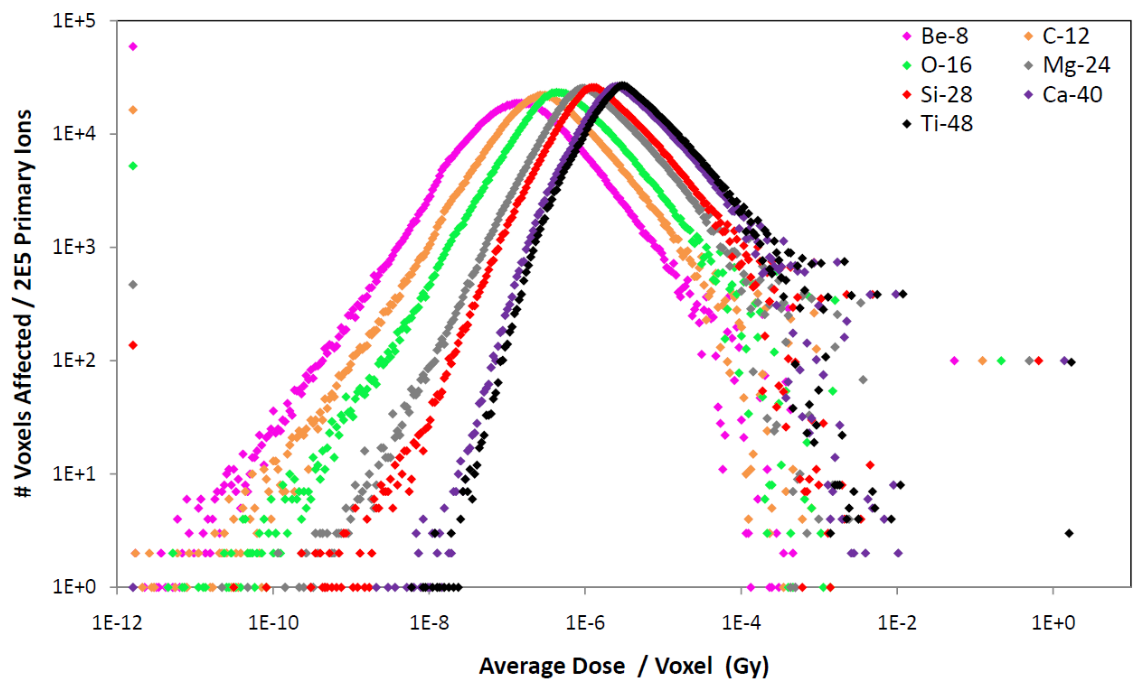

Figure 28. Population of 1,000 µm^3 targets receiving a dose in the mesh cube geometry by ions with 600 MeV n^{-1} velocities. Dose is presented as a trend that is averaged over the events produced by 200,000 primary particles traversing the geometry. Single primary-ion events produce many zero dose values making the average values orders of magnitude lower. Individual primary ion events would be seen as only a few, random, data points.

Figures 29 and 30 display a similar histogram, except the targets are affected by electron fluence, instead of dose. Similar to the dose measurements in Figures 27 and 28, the particle fluence values are averaged over the 200,000 primary ions simulated. Targets traversed by the primary ion experience greater-than one particle traversal due to the number of delta rays produced by the ion. The Be-8 ion, having the slowest velocity in Figure 29, affects significantly fewer targets since it has such a small penumbra. There are three data points signifying primary tracks, where particle fluence is greater-than one. The Be-8 peak describes the few delta-ray events that escape the volume of the 10 μm thick voxels located along the primary particle axis. As velocity increases, the number of delta rays escaping those central voxels increases creating a broader data curve. The Ca-40 and Ti-48 ions have a similar profile, suggesting their penumbras envelop roughly the same dimensions for this particular target geometry. The Ca-40 ion, with lower velocity, still manages to create energetic-enough delta rays to affect most targets inside this geometry.

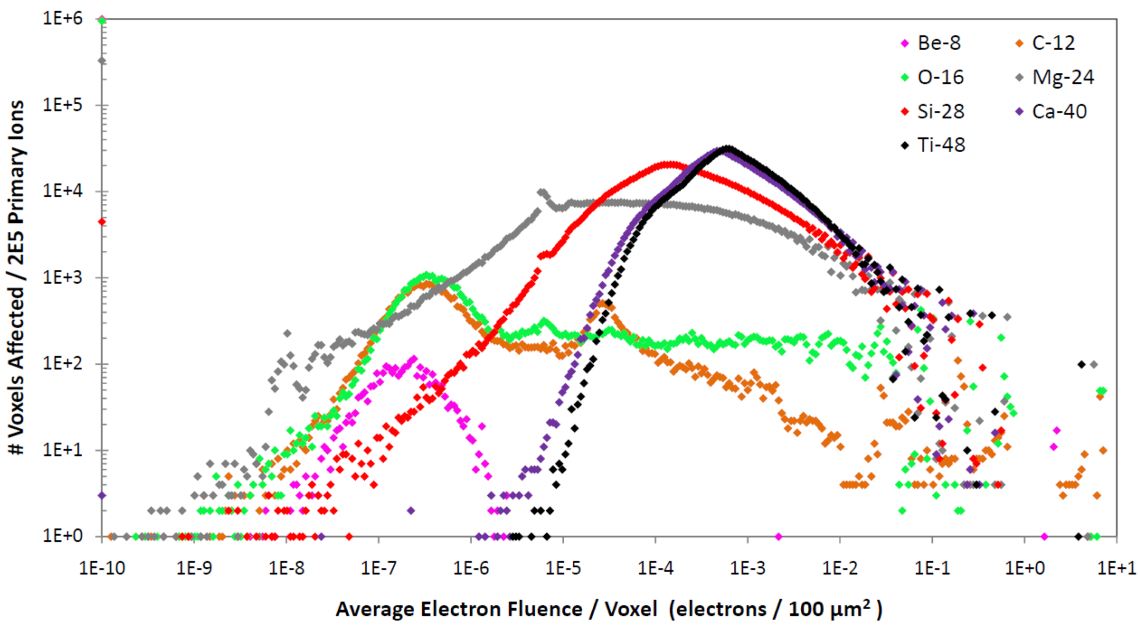

Figure 29. Population of 1,000 µm^3 targets affected by traversing electrons in the mesh cube geometry by ions with 100 keV µm^{-1} stopping powers. Fluence is presented as a trend that is averaged over the events produced by 200,000 primary particles traversing the geometry. Single primary-ion events produce many zero fluence values making the average values orders of magnitude lower. Individual primary ion events would be seen as only a few, random, data points.

The ions of equal velocity all produce a similarly-shaped curve that is proportional to Z^2. There is a peak of ~20,000 targets affected by 1E-5 to 1E-3 electrons per primary ion. This 20,000 target peak is also seen in the dose plot. Dose-depth and radial dose profiles can also be taken from these data although radial dose is only as narrow as the 10 µm voxel. Figures 27 and 29 present similar trends, indicating a correlation between the energy deposited and delta-ray fluence. This similarity is also present for Figures 28 and 30.

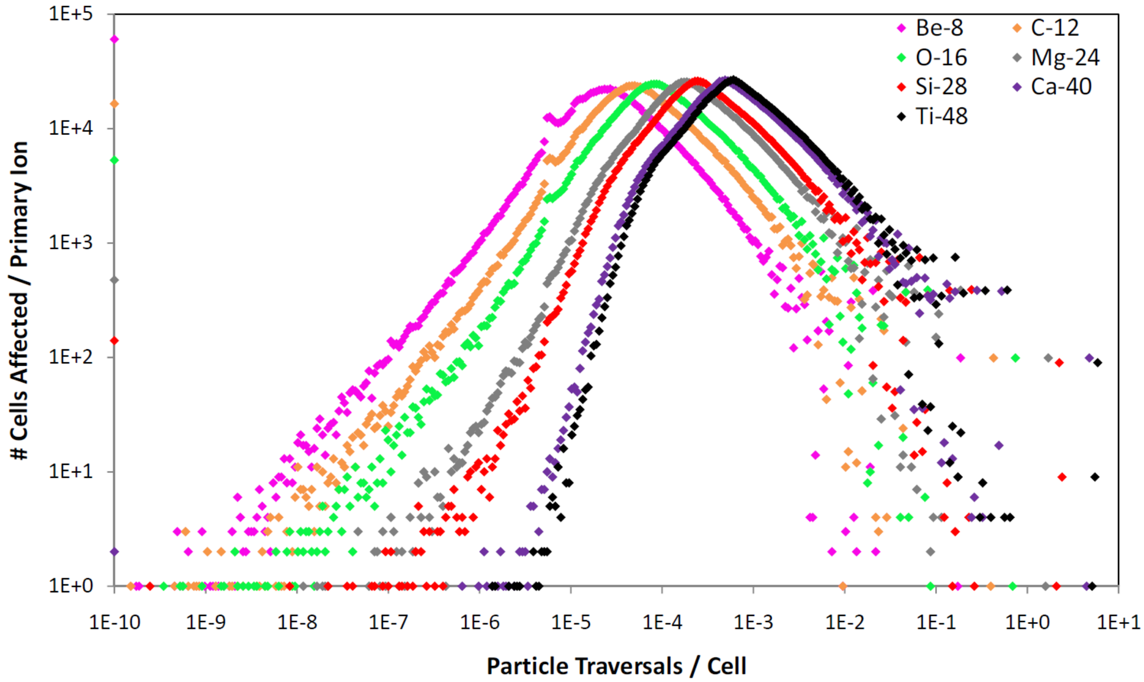

Figure 30. Population of 1,000 μm^3 targets affected by traversing electrons in the mesh cube geometry by ions with 600 MeV n^{-1} velocities. Fluence is presented as a trend that is averaged over the events produced by 200,000 primary particles traversing the geometry. Single primary-ion events produce many zero fluence values making the average values orders of magnitude lower. Individual primary ion events would be seen as only a few, random, data points.

Figures 28 and 30 showed that the delta-ray penumbra depends only on Z^2 for ions of equal, 600 MeV n^{-1}, velocity. Therefore, it can be deduced that the shapes of the curves in Figures 27 and 29 are based on ion velocity and those curves would be the same for any ion having the same velocity; only the magnitude of each point would vary by Z^2.

The next step toward an estimate of damaging ability is the correlation of dose and particle fluence for each target. Figure 31 displays the electron fluence that deposits a certain dose per voxel averaged over 200,000 primary ion simulations. The linear slope that creates the backbone of each series is a reflection of the similar shapes of the dose curves in Figures 27 and 29, and of the particle fluence curves in Figures 28 and 30. The ions represented in Figure 31 are Ti-48, O-16, and Be-8, having equal stopping power at the target's entrance surface. Only three ions were shown for visual clarity between the data points. Figure 32 is the same as Figure 31, but includes the Si-28 ion events. For both Figures 30 and 31, the primary ion dose is depicted in the top right where dose is highest and there is greater-than 1 particle crossing per target. The large data section of the plot represents the delta-ray penumbra. The Be-8 extends to a higher dose because it experiences its Bragg peak within the 1 mm cube. It also has the lowest incidence of particle traversals and at a low dose. There are very few, high-dose, data points from the Be-8 ion that suggest unlikely events where the primary ion scatters significantly and comes to a stop in a rare voxel.

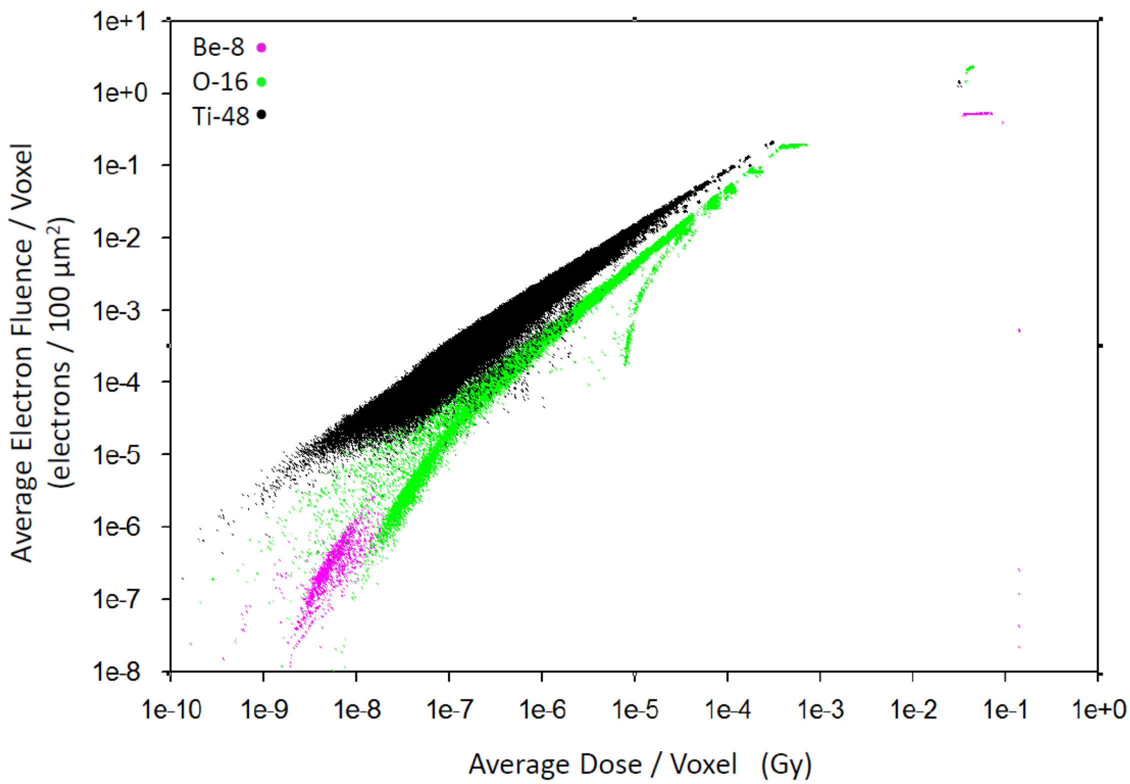

Figure 31. The electron fluence corresponding to a given dose for individual 1,000 μm^3 targets inside the cube mesh geometry for Be-8, O-16, and Ti-48 ions with 100 keV μm^{-1} stopping powers. Fluence vs. dose is presented as a trend that is averaged over the events produced by 200,000 primary particles traversing the geometry. Single primary-ion events produce many zero dose and fluence values making the average values orders of magnitude lower. Individual primary ion events would be seen as only a few, random, data points.

In Figure 32, the Si-28 ion appears to have the most significant penumbra, because it covers the largest area. The Ti-48 ion actually has more overlap of data points, but it is not described well by this figure. Referring to the particle fluence histogram in Appendix B, the Ti-48 ion affects all targets in the cube.

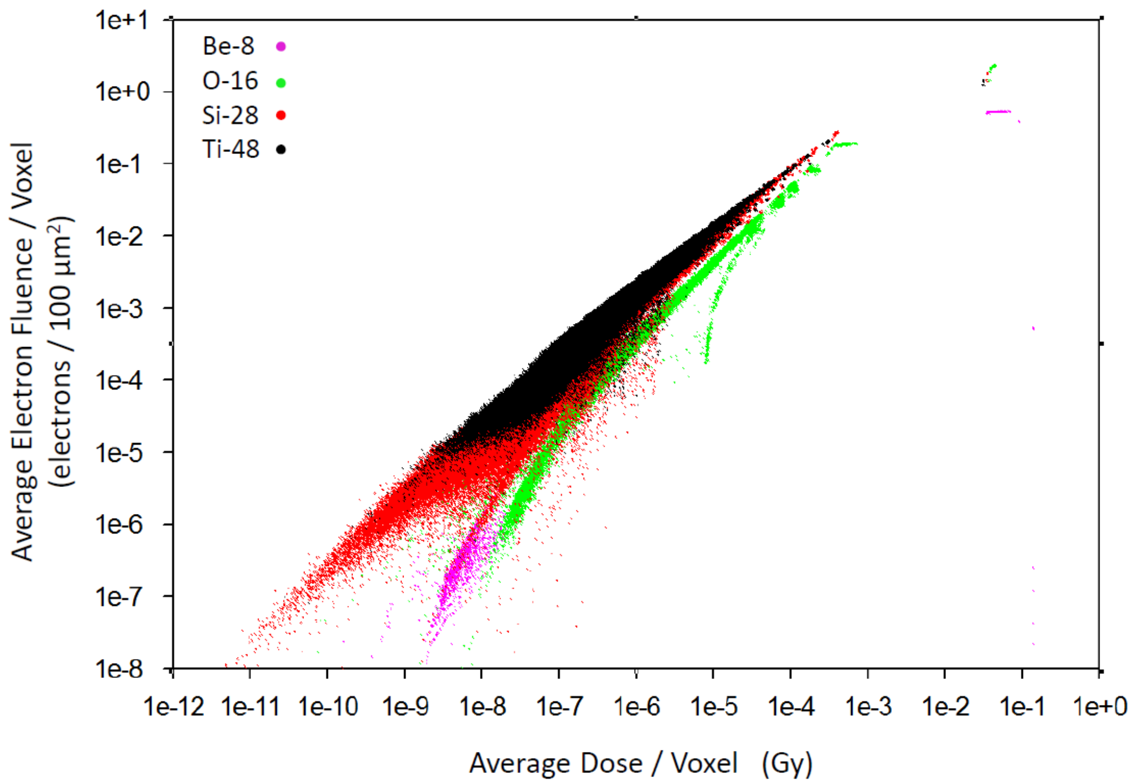

Figure 32. The electron fluence corresponding to a given dose for individual 1,000 µm^3 targets inside the cube mesh geometry for Be-8, O-16, Si-28, and Ti-48 ions with 100 keV µm^{-1} stopping powers. Fluence vs. dose is presented as a trend that is averaged over the events produced by 200,000 primary particles traversing the geometry. Single primary-ion events produce many zero dose and fluence values making the average values orders of magnitude lower. Individual primary ion events would be seen as only a few, random, data points.

The ions exhibited different shapes and magnitudes for Figures 31 and 32. Figure 33 displays the results for ions of equal velocity. The ions represented are Ti-48, O-16, and Be-8 at 600 MeV n^{-1}. The trends carry shape similarities, and there's more overlap for higher Z ions, describing a higher magnitude of dose and particle fluence for the Ti-48. In Figure 33, the Be-8 ion data cover the largest area, while the Ti-48 ion covers the smallest. The Ti-48 ion affected all targets inside the mesh cube geometry, so the particle fluence and dose values continued to add up, unlike the Be-8 ion that affected few targets.

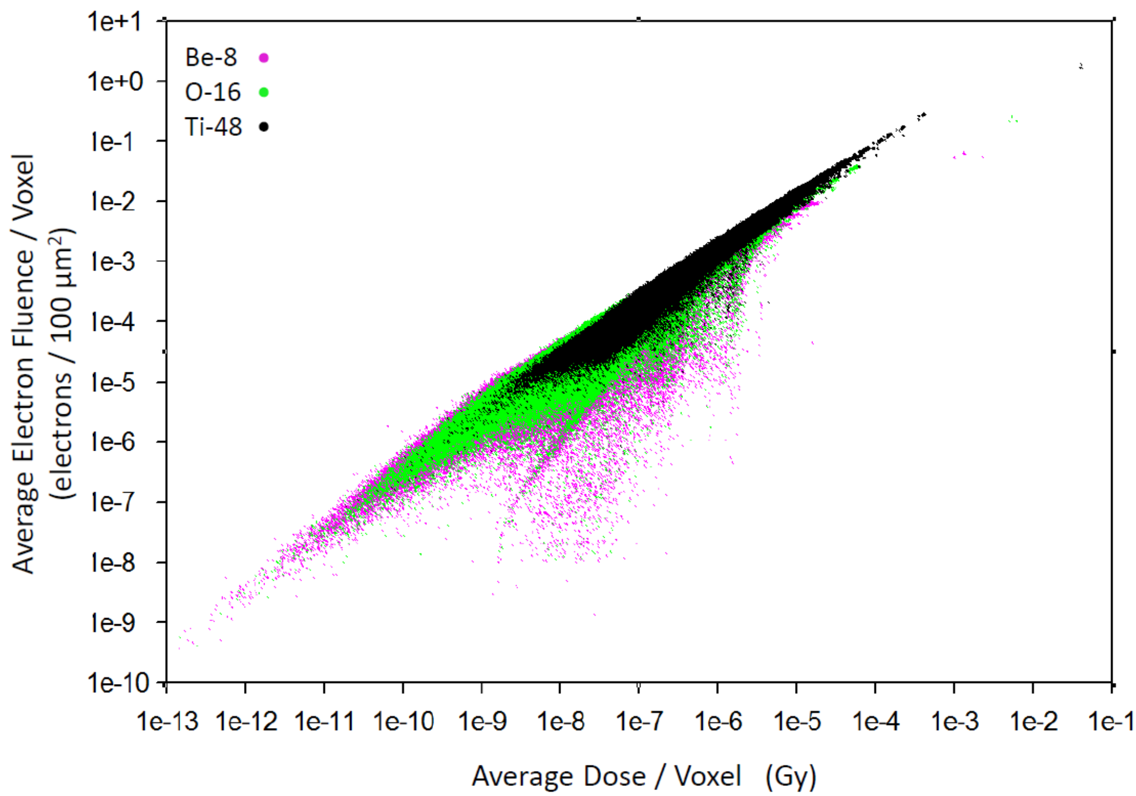

Figure 33. The electron fluence corresponding to a given dose for individual 1,000 μm^3 targets inside the cube mesh geometry for Be-8, O-16, and Ti-48 ions with 600 MeV n^{-1} velocities. Fluence vs. dose is presented as a trend that is averaged over the events produced by 200,000 primary particles traversing the geometry. Single primary-ion events produce many zero dose and fluence values making the average values orders of magnitude lower. Individual primary ion events would be seen as only a few, random, data points.

Table 8 was created from the mesh cube data presented in Figures 27, 29, 31, 32. Based on each ion velocity, the total dose deposited in the cube varies significantly as shown in Figure 17 due to the change in stopping powers leading to higher dose from the slower ions. The Be-8 ion imparts the least dose, because it stops near the 300 μm depth. The O-16, Mg-24, Si-28, and Ti-48 ions all deliver about the same percent of dose by delta rays. Unlike the Be-8 and C-12 ions, the higher velocity ions are not increasing significantly in stopping power across the 1 mm thick cube. The Ca-40 and Ti-48 ions are exhibiting delta-ray loss, by imparting slightly lower-electron doses than the doses of the O-16, Mg-24, and Si-28 ions. The O-16, Mg-24, and Si-28 ions also impart a higher-electron dose to far fewer targets than the Ca-40 and Ti-48 ions. Similarities in electron dose values suggest that the ions actually impart the same LET values through secondary electron production. Velocity and target geometry have a strong influence on obtaining consistent dosimetry readings.

Table 8. Dose characteristics within mesh cube geometry for ions having 100 keV μm^{-1} stopping powers. Data describe the number of targets affected by variations in the delta-ray penumbra created by ions with different velocities.

100 keV μm^{-1}	Be-8	C-12	O-16	Mg-24	Si-28	Ca-40	Ti-48
Tot Dose (Gy) / primary	8.72E-09	2.01E-08	1.72E-08	1.62E-08	1.59E-08	1.52E-08	1.46E-08
Electron Dose (Gy)	8.38E-10	5.02E-09	5.34E-09	5.33E-09	5.32E-09	5.02E-09	4.69E-09
% Electron dose per Total dose	9.61	24.98	31.05	32.90	33.46	33.03	32.12
Unhit cells	997,381	962,393	946,903	329,473	4,473	3	0

The damaging ability of the 100 keV μm^{-1} ions was determined from the population of targets that receive dose by secondary-electron traversals. Table 9 presents a summation of the product of dose and number of targets affected for each curve. This information is described by taking the area under each curve in Figures 27 and 29. The analysis is performed, separately, for both the dose plot in Figure 27 and the particle traversal plot in Figure 29. Different radiation types are commonly compared by their damaging ability relative to a reference radiation to establish RBE values. The results of this research are normalized to the Si-28 ion value because it represents a mid-point value for charge and velocity. Damaging ability is summed from the data calculated by the FLUKA code and presented in Table 9. The primary ion track for each simulation includes significant scattering effects and increases in stopping power for lower-velocity ions. For the higher-dose values in Figures 27 and 29, the lower-velocity ions display a scattering of data points. The data presented in Table 9 exclude dose and electron fluence data for the voxels located in the center of the target that are traversed by the primary ions. The data are not presented in conventional dosimetry terms, because each dose and particle traversal data point is multiplied by its frequency. Summing each target dose does not yield the total dose for the mesh cube.

Table 9. Voxel dose and particle traversals are summed, separately, from data in Figures 27 and 29 to establish a value for damage imparted to targets located more than 5 µm from the primary ion track.

	Cumulative Dose Events	Relative to Si-28		Cumulative Particle Fluence Events	Relative to Si-28
Be-8	5.56E-05	2.59E-05		2.86E-03	1.46E-06
C-12	1.0290	0.4792		146.69	0.0751
O-16	1.2457	0.5802		519.75	0.2660
Mg-24	1.9839	0.9240		1537.69	0.7871
Si-28	2.1470	1.0		1953.68	1.0
Ca-40	**2.1603**	**1.0062**		2384.28	1.2204
Ti-48	2.0454	0.9527		**2386.41**	**1.2215**

The Ti-48 ion produces the most targets affected for the mesh cube geometry. The dose imparted by the Ti-48 ion penumbra is less than that for the Ca-40 and Si-28 ions because of delta rays escaping the target. Information presented in Table 9 gives a relation for penumbra effects at radial distances greater than the core axis of 5 μm voxels at the center of the mesh geometry. The cylindrical mesh geometry provides dosimetry inside the 5 μm radius.

The cylindrical mesh, having radius of 5 μm and length of 10 μm, contains 1 million voxels with 1000 nm^3 volumes, simulating DNA-sized targets within a cell nucleus. A simulation of 200,000 primary ions was performed with the FLUKA code only for ions of equal stopping power. The dose and particle fluence were calculated for each voxel. Figure 34 displays radial dose across the mesh cylinder, similar to the earlier models in this study. Agreeing with the cylindrical shell simulation, C-12 ions deliver the highest dose up to a 2 μm radius, where O-16 ions begin to impart higher dose due to a slighter larger penumbra. The Be-8 ion penumbra drops off at 4 μm, characterizing the outer reaches of its penumbra. The radial distance scale represents penumbra data within a 5 μm radius down to the primary track, detailing track structure within a cell nucleus-sized volume.

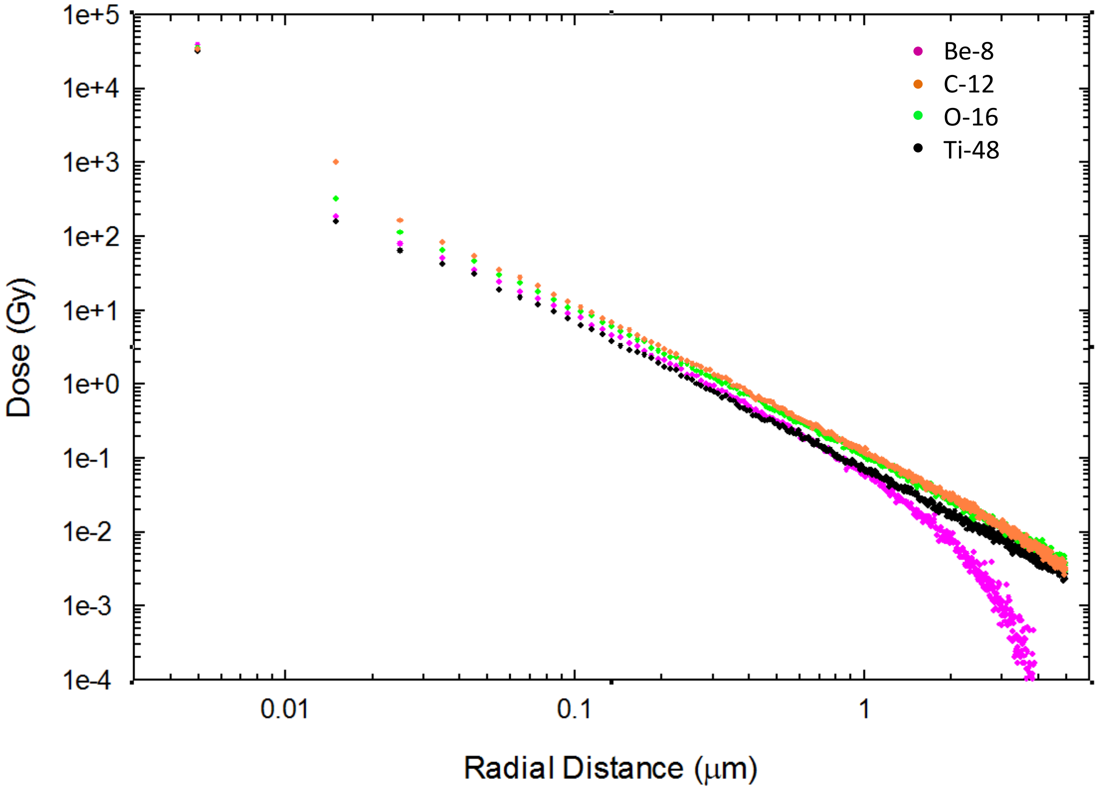

Figure 34. Dose as a function of radial distance away from the primary ion track inside the cylindrical mesh geometry. Data points represent FLUKA calculations for delta rays created by ions of equal 100 keV μm^{-1} stopping powers traversing a 10 μm thick water target. Dose values are averaged over 200,000 primary particles traversing the geometry.

Figure 35 displays the mesh cylinder data for C-12 and Ti-48 ions in reference to the Chatterjee calculation. The trends are quite similar, but there is definitely a difference in magnitude between the two approaches. A larger discrepancy in magnitude appears for the Ti-48 ion, as opposed to the C-12 ion data. This discrepancy is most likely due to the effect of delta-ray buildup, as the higher-velocity Ti-40 ion requires larger buildup depth.

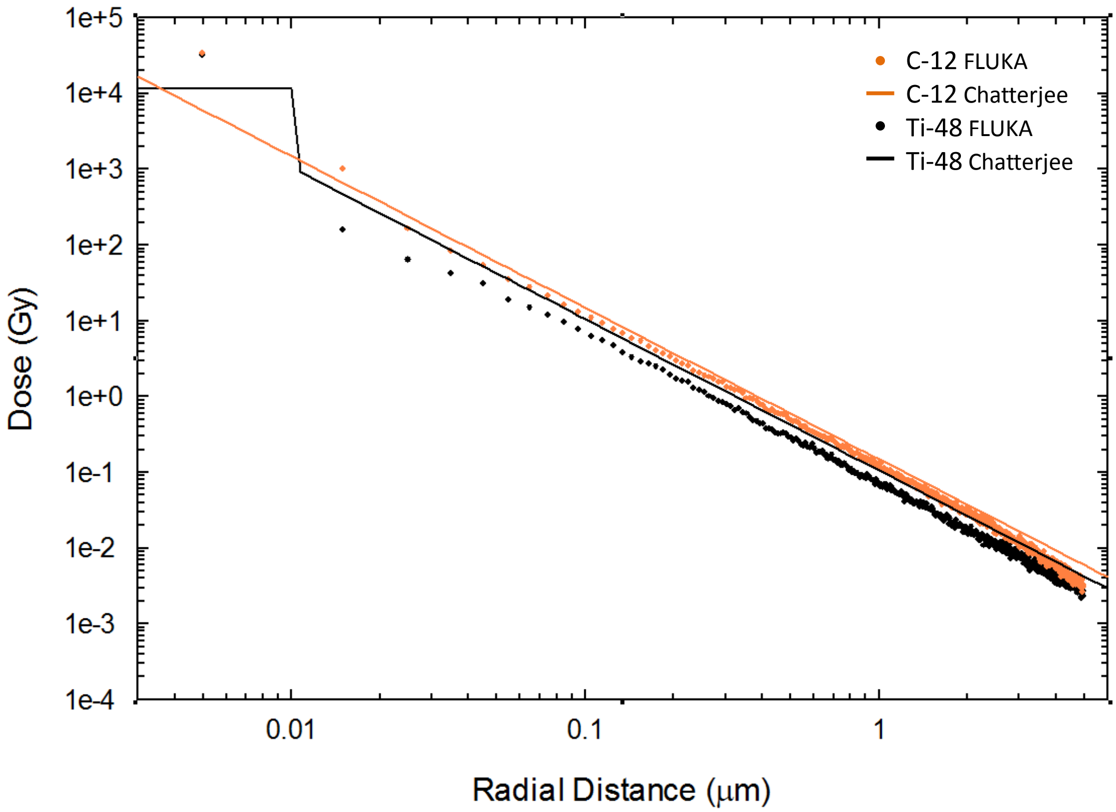

Figure 35. Dose as a function of radial distance away from the primary ion track inside the cylindrical mesh geometry presented with Chatterjee data. Data points represent FLUKA calculations for delta rays created by ions of equal 100 keV μm^{-1} stopping powers traversing a 10 μm thick water target. Data lines represent Chatterjee calculation for the same ions. For FLUKA data, dose and particle fluence values are averaged over 200,000 primary particles traversing the geometry.

Figures 36 and 37 display data for the dose and particle fluence, for individual voxels, imparted by delta rays produced within the mesh cylinder. Dose and particle fluence is averaged over 200,000 primary particle simulations. The Be-8 ion track structure is well contained within the small geometry of 10 μm, which is why the curve in Figure 36 presents such a broad spectrum of events. As velocity increases, and delta-ray ranges increase, the trends become more similar, as more targets are affected by a higher-energy delta ray spectrum. The trends described in Figures 36 and 37 exhibit a lower occurrence of events at low-dose for lower velocity ions and a higher occurrence of events at higher-dose. The primary ion track extended over a depth of 10 μm, and voxels are 10 nm thick. Therefore, the number of voxels receiving the core dose was 1,000 and is reflected by the plateau data in Figures 36 and 37. There is a scattering of data around the 10 – 100 Gy per target and 1E-4 to 2E-2 electrons per target area. These data represent primary ion scattering events away from the beam axis that deliver a higher dose to the surrounding targets. There is less scattering for the higher-velocity ions.

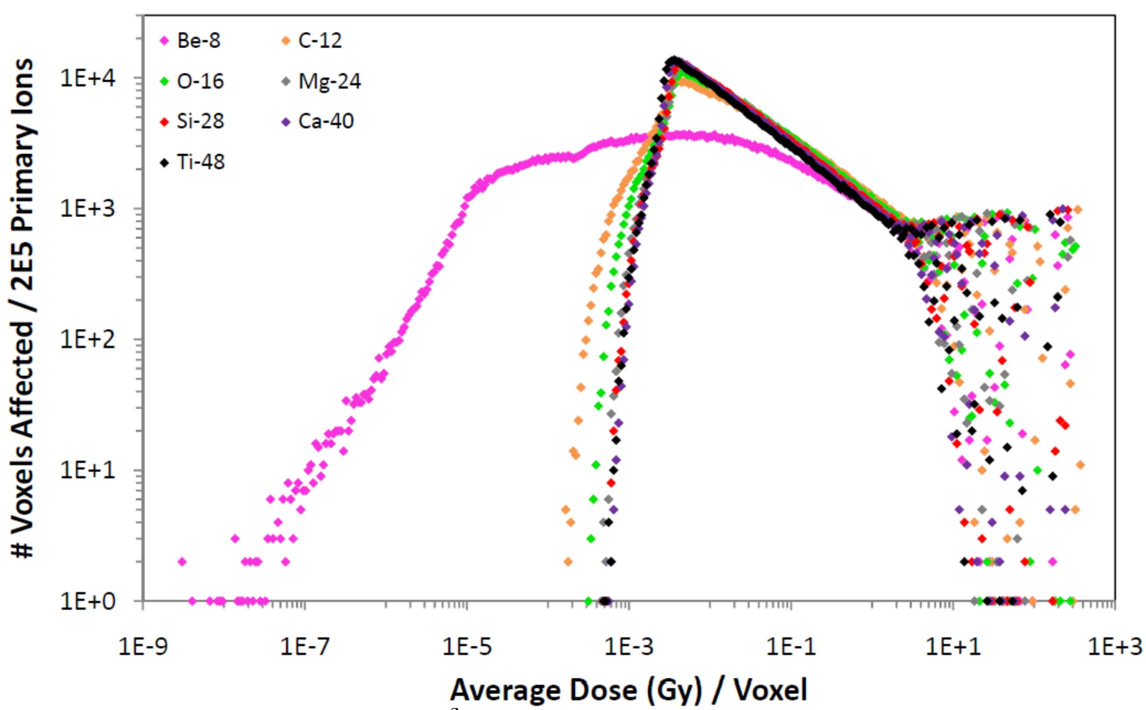

Figure 36. Population of 1000 nm^3 targets experiencing delta-ray dose inside the cylindrical mesh geometry by ions with 100 keV μm^{-1} stopping power. Dose values are averaged over 200,000 primary particles traversing the geometry. The large change in shape of the Be-8 ion data trend explains the effect of events that deposit zero dose in some voxels.

The shape of the curves in Figures 36 and 37 is similar, as seen earlier in the larger mesh geometry. However, there is a slight deviation in the peak regions between Figures 36 and 37. The Be-8 and C-12 ions appear to deviate more than the other ions. The dose per voxel can be divided by the electron fluence traversing that voxel, and describes differences in the approximate stopping powers of delta rays produced by different ions. As shown in Figure 38, the higher-velocity ions generate faster electrons, having lower-stopping power, so there are more events on the low end of the spectrum.

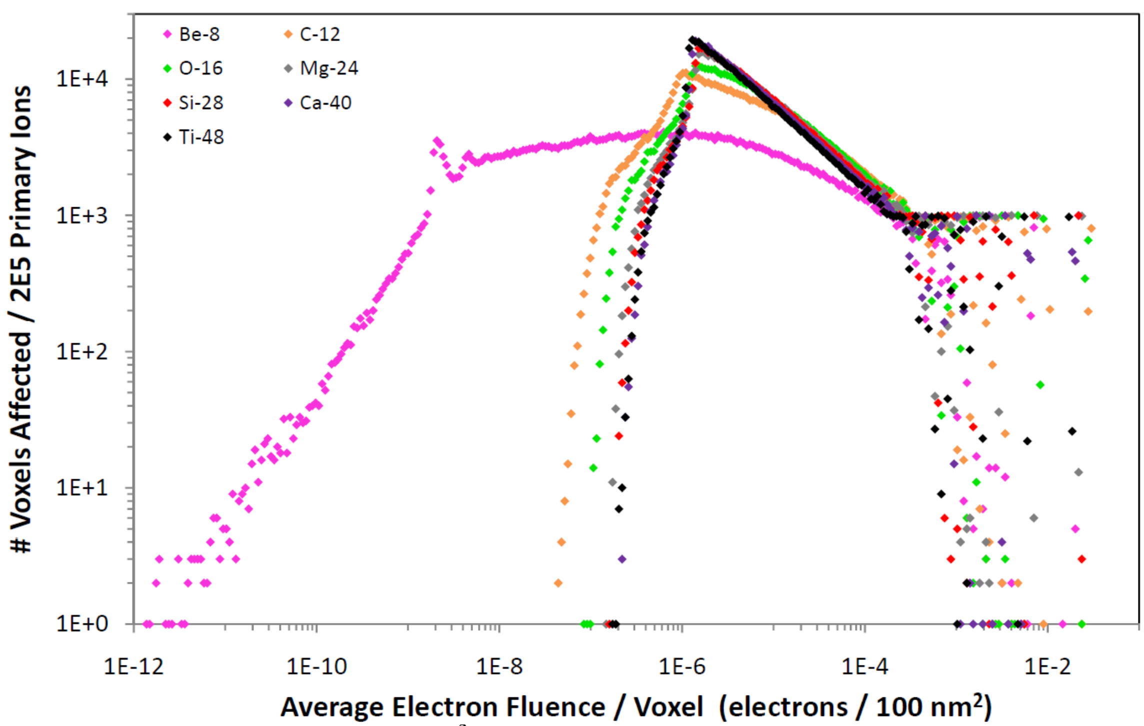

Figure 37. Population of 1000 nm^3 targets experiencing delta-ray fluence inside the cylindrical mesh geometry by ions with 100 keV μm^{-1} stopping power. Fluence values are averaged over 200,000 primary particles traversing the geometry. The large change in shape of the Be-8 ion data trend explains the effect of events that deposit zero dose in some voxels.

This analysis can be performed for this geometry because there is minimal ion scattering, and nearly all targets are traversed by delta rays. The Be-8 ion delta rays deliver higher dose on a per-particle basis. There is a maximum cut-off value experienced by each ion, except for Be-8, in Figure 38. This effect describes the range of possible dose values deposited by a delta ray that traverses the voxel targets.

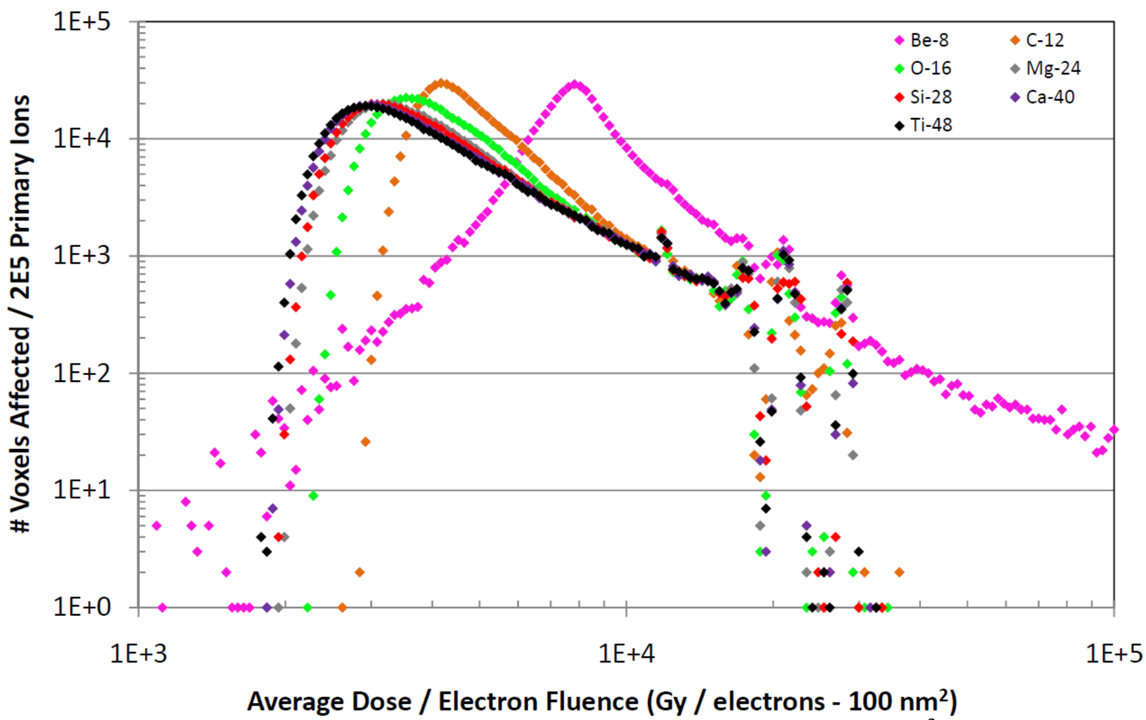

Figure 38. Dose per electron fluence across the population of 1000 nm^3 targets in the cylindrical mesh geometry by ions with 100 keV µm^{-1} stopping power. Dose and fluence values are averaged over 200,000 primary particles traversing the geometry. Be-8 ion abscissa values past ~3.5E4 are attributed to primary ion scatter so the data is cut off.

The higher events exhibited by the Be-8 ion describe scattering of the primary ion into voxels outside of the beam centerline and are not included in the damage calculation. Higher-velocity ions produce a larger number of delta rays that impart larger particle fluence per target, shown in Figure 37. The very small dose per fluence values experienced by the Be-8 ion describe the influence of un-hit voxels following individual primary ion events. These zero values are averaged into the total for each voxel. Smaller delta-ray fluence, in addition to increased delta-ray stopping power, result in the dominating C-12 ion curve in Figure 38.

The lower-velocity ions exhibit delta rays with a higher stopping power within a cell nuclei-sized volume. Similar to the analysis creating the data in Table 9, Table 10 presents damaging ability as the area under the curve for Figures 36, 37, and 38. The damage value is calculated by multiplying the abscissa value by the number of targets affected in Figures 36, 37, and 38. That information is summed into the data in Table 10 and displayed as the product of the number of targets affected multiplied by the dose, particle fluence, or dose per electron fluence per target in the cylindrical mesh geometry.

Table 10. Damaging events in the cylindrical mesh target are described as the total product of dose, particle traversals, and dose per electron fluence multiplied by the population affected. Ions have stopping powers of 100 keV μm^{-1}.

	Cumulative Dose Events	Relative to Si-28		Cumulative Particle Fluence Events	Relative to Si-28		Cumulative Dose/Electron Fluence Events	Relative to Si-28
Be-8	7.674E+05	0.955		48.736	0.928		**3.949E+09**	**1.787**
C-12	**1.072E+06**	**1.335**		**71.570**	**1.363**		2.656E+09	1.202
O-16	9.646E+05	1.201		64.678	1.232		2.382E+09	1.078
Mg-24	8.416E+05	1.048		56.045	1.067		2.234E+09	1.011
Si-28	8.032E+05	1.000		52.515	1.000		2.210E+09	1.000
Ca-40	7.008E+05	0.872		46.402	0.884		2.167E+09	0.980
Ti-48	6.393E+05	0.796		41.644	0.793		2.151E+09	0.973

To assess the damage imparted, Table 10 presents the product of interaction events with the number of targets experiencing those events. C-12 delivers the highest dose and delta-ray fluence for the cylindrical mesh. Ti-48 delivers the lowest values, signifying a lower amount of damage within this intercellular volume. Table 9 showed that for radial distances beyond 5 µm, Ca-40 scores the highest damage value for dose and Ti-48 scores larger delta-ray fluence. This is a direct example of the electron stopping power being higher for the delta rays produced by the Ca-40 ion, compared with the Ti-48 ion delta rays. In this cylindrical mesh, the Be-8 ion creates delta rays with the highest stopping power. Table 11 averages the values from the two different mesh geometries to account for both inner and outer penumbra damaging effects. Data are displayed relative to the Si-28 value in each category.

Table 11. Damaging events compared across cylindrical and cubic geometries.

Ion	Cumulative Dose Events Relative to Si-28			Cumulative Particle Fluence Events Relative to Si-28		
	<10 µm	>10 µm	Average	<10 µm	>10 µm	Average
Be-8	0.9554	2.59E-05	0.4777	0.9280	1.46E-06	0.4640
C-12	**1.3349**	0.4792	0.9071	**1.3629**	0.0751	0.7190
O-16	1.2010	0.5802	0.8906	1.2316	0.2660	0.7488
Mg-24	1.0478	0.9240	0.9859	1.0672	0.7871	0.9271
Si-28	1.0000	1.0000	**1.0000**	1.0000	1.0000	1.0000
Ca-40	0.8724	**1.0062**	0.9393	0.8836	1.2204	**1.0520**
Ti-48	0.7960	0.9527	0.8743	0.7930	**1.2215**	1.0072

The mesh cube geometry is described as intracellular and contained outside of a 5 µm radius from the primary particle axis. The cylindrical geometry is described as intercellular and contained within a 5 µm radius. The combination of the two geometries is meant to account for the high-energy density near the ion path as well as the large number of cells, far from the primary ion, that are affected. While C-12 and O-16 were highly damaging at small radii, the large number of targets affected by the Ca-40 and Ti-48 ions outweighs as a more significant factor. Damaging ability is seen to depend largely on the target volume of interest because velocity significantly determines where the energy is deposited. A larger number of cells are affected for higher-velocity ions, but the dose per delta ray is higher for lower-velocity ions. The data do show that the significantly high velocity of Ti-48 causes energy loss outside the target. Those delta rays have higher kinetic energy and, therefore, lower stopping power. Were the study to include targets outside of the 1 mm mesh cube, then the Ti-48 damaging effects would increase. This study may also indicate that kinetic energy in the range of a few hundred MeV n^{-1} is significant to the volumes of interest for biological damage. This is also the most abundant velocity for GCR.

The relative damaging ability for the different ions has been described by two different microdosimetric studies for targets inside and outside the scale of a cell nucleus. Damage is due to the energy deposition of the secondary electrons surrounding the primary ion path. Ion kinetic energy directly influences the localization of dose. A slower-traveling ion does more damage at small radii, while a faster ion spreads its dose to larger distances. The data show that the Be-8 ion (6.8 MeV n^{-1}) isolates its dose to very narrow radii within about 1 μm. The C-12 ion (18.5 MeV n^{-1}) proves to be the most effective velocity for concentrating its dose across about 5 μm radii, or the size of a cell nucleus. It is very helpful to reference the analysis of ions at equal velocity. It can be concluded that the track structure of any ion at equal velocity will deliver the same spectrum of delta rays to a cell-sized volume, while the magnitude of dose depends only on Z^2. This conclusion does not hold for ions whose stopping power varies significantly over the target thickness.

Seven different ions, each at a different velocity were studied, and it has been determined that the spatial distribution of dose is dependent upon the primary ion velocity. The magnitude of the dose is dependent upon the primary ion charge. The next step in furthering this study would be to establish a normalized value for damage based upon the existing data, and removing the influence of each ion charge by dividing out Z^2. This normalized factor would then be established for each velocity (comparable to MeV n^{-1}) used in the study. Z^2 could be incorporated back into those velocities to provide damage factors for each ion and each seven different velocities.

Realistically, this information would only apply to ions whose stopping power do not vary significantly across the target. As long as the damaging effects are consistent with that produced in the equal velocity approach used in this study, then a normalized value for damaging ability could be developed for each velocity of interest. Ion charge could be simply incorporated by multiplying by Z^2.

The decision for which ion imparts more damage relative to another comes down to the definition of damage. Considering GCR, genetic mutations created by mis- or unrepaired DNA, are the primary focus. If a cell is killed by a particle track in this low dose-rate environment, then it cannot go on to form a cancer. The region within a 5 µm radius has been described as one cell nucleus. The Be-8, C-12, and O-16 ions contained their damage primarily within this region, meaning the dose deposited on DNA strand sized targets would be higher. However, for a 1 mm^3 target, their effects are only dominant for ~100 cells compared to Si-28, Ca-40, and Ti-48 ions that affect far more cells. The other 999,900 cell nuclei will be more affected by the delta rays from a higher velocity ion. Therefore, emphasis must be placed on the number of cells receiving the largest number of particle traversals. Realistically, the Ti-48 affects many more cells, influencing its damaging ability outside the target volumes simulated in this research. Damaging ability is scenario specific and largely a factor of ion velocity and charge.

CHAPTER V

CONCLUSION

The biological risks of heavy ions encompass a broad field of research involving characterizing the space radiation field, shielding effects, track structure, biological damage, and repair mechanisms. Many factors determine how a HZE ion will interact with and change the mammalian cell that it traverses. This dissertation provided a review of these topics and focused on an in-depth study of track structure. The spatial distribution of energy deposition was determined by simulating biologically-similar target traversals by an ion and its secondary particles. Emphasis was placed on ion charge and velocity by keeping the targets of interest to a small scale. This approach helped to minimize effects of ion fragmentation, scatter, and increases in ion stopping power. Charge and velocity were determined to significantly affect the spectra of possible energy deposition events.

Based on the FLUKA simulations, for ions of equal stopping power (100 keV μm^{-1}), the Ti-48 ion imparted the lowest LET value to 1 μm thick water slabs. Due to its higher velocity, the Ti-48 ion experienced the most delta-ray escape from the target slab. Ions of equal velocity (600 MeV n^{-1}) were shown to deposit LET values proportional to Z^2.

Earlier studies implemented an amorphous track structure model to predict radial dose around an ion track. The methods used in this research simulated a cylindrical geometry to provide radial dose measurements, similar to the amorphous track model.

The FLUKA code simulated delta-ray penumbras of the same radii as the Chatterjee calculation. The simulated data showed a larger percentage of dose to be deposited within a 5 nm radius, compared to the Chatterjee calculation. This was primarily due to the fact that the FLUKA code doesn't transport electrons below 1 keV, so those electrons were considered to be deposited in the track core. The lower-velocity ions deposited a larger percent of dose for radial distances inside 5 μm. The C-12 ion deposited the largest dose inside a 1 μm radius. The Ti-48 ion imparted the lowest dose for this dimension but produced a delta-ray penumbra that extended over a 5 mm radius. Radial dose trends were the same for ions of equal velocity. The delta-ray penumbrae extended over the same volumes with dose varying as a function of Z^2.

Delta-ray equilibrium was determined to be a significant factor in simulating radial dose measurements for radii greater than 5 μm. To provide delta-ray buildup, significant target thicknesses were required to be placed in front of the target slabs in the FLUKA code geometry. Increased buildup-depth influenced radial scattering of the primary ion that complicated radial-dose measurements at distances near the track core.

To further investigate the spatial distribution of dose by the delta-ray penumbra, a voxel geometry was simulated in the FLUKA code. This method was used to calculate the dose and particle fluence for specific sites. The results described the number of voxels that received a corresponding dose from both the primary ion and by the delta-ray penumbra. The higher-velocity ions imparted their dose over most of the voxels, while the lower-velocity ions imparted their dose near the primary ion track. Out of 1 million voxels in the mesh cube geometry, the Ti-48 ion affected 1 million, while the C-12 ion affected only 37,607 voxels. The Be-8 ion affected even fewer, although it did not penetrate the entire target, due to its low velocity. Neglecting the Be-8 ion, the C-12 ion deposited the most energy across the 1 mm thick target (~125 MeV), while the Ti-48 ion deposited the least (~91 MeV). Physical target damage was described by the cumulative dose and particle fluence values across all voxels. The values were set relative to the Si-28 ion value to establish a relative damaging ability. The Ca-40 ion imparted the most dose-related damage, while the Ti-48 ion imparted the most particle fluence-related damage. These two ions affected far more targets than the other ions.

The cylindrical mesh geometry simulated 1 million target voxels inside a 10 μm thick cylinder having a radius of 5 μm. Radial dose was calculated, based on the FLUKA data. The radial trends were similar to the Chatterjee data, but predicted less dose. This effect was due to a lack of delta-ray equilibrium in the thin target. The quotient of voxel dose per electron fluence was established to describe the stopping power of the delta rays created by each ion. Slower ions created slower delta rays. The Be-8 ion produced delta rays with the highest stopping power. The C-12 ion was shown to produce the most delta rays. Those delta rays were of relatively low velocity, so the C-12 ion imparted the most dose and fluence-related damage to voxels in the cylindrical mesh geometry.

The relative damage values were averaged over the two mesh geometries. The Si-28 ion was determined to be the most damaging for dose-related damage, while the Ca-40 ion was the most damaging for particle fluence-related damage. The analysis performed in this research focused on both the high-ionization density within a cell nucleus-sized volume, as well as the low-ionization density created the delta-ray penumbra extending over the range of many cell volumes. This outer region is more similar to the diffuse ionization density of photon irradiation, while inside the cell nucleus lies the densely-ionizing track that makes heavy ions so damaging. This research did not attempt to predict biological endpoints. The conclusions drawn here relate the total damage imparted by GCR in reference to each other. Damage was described by energy deposited and particle fluence in small sites.

This research focused on the damaging ability of ions with 100 keV μm^{-1} stopping powers because their corresponding LET values have the highest quality factor for calculating dose equivalent. The analysis performed in this research could be reproduced for a single ion at different stopping power values. Variations in delta-ray penumbrae have been shown to vary as a function of primary ion velocity. The primary ion charge only designates the magnitude of secondary electrons produced. Spatial distribution of dose is determined by velocity, and its magnitude is simply a function of Z^2. At equal velocity, ions with higher charge have shorter range so choosing proper target geometries presents a challenge for comparing different ions.

Further research is needed to predict the biological risks associated with heavy ions. This dissertation thoroughly describes how the effects of charge and velocity impact resulting physical interactions and secondary-particle production. Radiation biology projects can utilize this information to better predict the microdosimetry within cellular targets in heavy ion-irradiation experiments.

Future Work

The methods utilized in this research could be extended to include additional stopping power values, higher-velocity ions, and different target-geometry scenarios. This approach would broaden the amount of data produced here. The mesh geometry simulations would be improved by providing data based on single-ion traversals, rather than the averages determined in this research. That method would provide random sampling of the actual dose and electron fluence for individual target voxels. A separate data analysis approach would be required to process the large amount of data that would be produced. Perhaps focusing on only a single atomic number ion would simplify the work. The Z^2 relationship could be utilized to relate that data to additional ions.

A separate computer code, such as GEANT4, could be utilized to perform delta-ray transport below 1 keV kinetic energies. There would be significant improvement to data drawn from the cylindrical mesh geometry utilized in this research. A separate library of interaction cross sections would help to identify weaknesses of each code.

Finally, the analysis drawn from this research could be implemented into planning ion beam-line experiments. Radiobiology experiments focusing on the effect of ion charge and velocity on RBE could utilize the trends established in this research.

REFERENCES

Attix FH. Introduction to radiological physics and radiation dosimetry. 2004 ed. Weinheim, Germany: Wiley-VCH: 161-162, 2004.

Ballarini F, Alloni D, Facoetti A, Ottolenghi A. Heavy-ion effects: from track structure to DNA and chromosome damage. New Journal of Physics 10: 075008; 2008.

Bolch WE, Turner JE, Yoshida H, Jacobson KB, Wright HA, Hamm RN. Monte Carlo calculations of free ammonia production in deoxygenated solutions of glycylglycine irradiatd by x rays and Co γ rays. Radiation Research 121, No. 3: 248-256; 1990.

Butts JJ, Katz R. Theory of RBE for heavy ion bombardment of dry enzymes and viruses. Radiation Research 30, No 4: 855-871; 1967.

Charlton DE, Nikjoo H, Humm JL. Calculation of initial yields of single- and double-strand breaks in cell nuclei from electrons, protons, and alpha particles. Int J Radiat Biol 56 No 1: 1-19; 1989.

Chatterjee A, Schaefer HJ. Microdosimetric structure of heavy ion tracks in tissue. Radiation and Environmental Biophysics 13: 215-227; 1976.

Chatterjee A, Holley WR. Energy deposition mechanisms and biochemical aspects of DNA strand breaks by ionizing radiation. Int J Quantum Chemistry 39: 709-727; 1991.

Chatterjee A, Holley WR. Biochemical mechanisms and clusters of damage for high-LET radiation. Advances in Space Research 12, No 2-3: 233-243; 1992.

Cucinotta FA, Nikjoo H, Goodhead DT. The effects of delta rays on the number of particle-track traversals per cell in laboratory and space exposures. Radiation Research 150, No. 1, 115-119; 1998.

Cucinotta FA, Schimerling W, Wilson JW, Peterson LE, Badwar GD, Saganti PB, Dicello JF. Space radiation cancer risks and uncertainties for Mars missions. Radiation Research 156: 682-688; 2001.

Curtis SB, Nealy JE, Wilson JW. Risk cross sections and their application to risk estimation in the galactic cosmic-ray environment. Radiation Research 141, No 1: 57-65; 1995.

Goodhead DT. Energy deposition stochastics and track structure: what about the target?, Radiation Protection Dosimetry 122, No 1-4: 3-15; 2006.

Holley WR, Chatterjee A. Clusters of DNA damage induced by ionizing radiation: formation of short DNA fragments. 1. Theoretical modeling. Radiation Research 145: 188-199; 1996.

International Commission on Radiological Protection (ICRP). Relative biological effectiveness (RBE), quality factor (Q), and radiation weighting factor (w_R). Pergamon Press; ICRP Publication 92, Ann ICRP; 2003.

Katz R, Ackerson B, Homayoonfar M, Sharma SC. Inactivation of cells by heavy ion bombardment. Radiation Research 47, No. 2: 402-425; 1971.

Katz R. Track structure theory in radiobiology and in radiation detection. Nuclear Track Detection 2, No. 1: 1-28; 1978.

Kraft G, Kramer M, Scholz M. LET, track structure and models. Radiat Environ Biophys 31: 161-180; 1992.

Meesungnoen J, Jay-Gerin JP, Filali-Mouhim A, Mankhetkorn S. Low-energy electron penetration range in liquid water. Radiation Research 158, No. 5: 657-660; 2002.

National Council on Radiation Protection and Measurements (NCRP). Radiation protection guidance for activites in low-Earth orbit. NCRP Report 132, Bethesda, MD. 2000.

National Council on Radiation Protection and Measurements (NCRP). Information needed to make radiation protection recommendations for space missions beyond low-Earth orbit. NCRP Report 153. Bethesda, MD, 2006.

Nikjoo H, Uehara S, Wilson WE, Hoshi M, Goodhead DT. Track structure in radiation biology: theory and applications. Int. J. Radiat. Biol. 73, No. 4, 355-364; 1998.

Ritter S, Durante M. Heavy-ion induced chromosomal aberrations: A review. Mutation Research 701: 38-46; 2010.

Turner JE, Bolch WE, Yoshida H, Jacobson KB, Wright HA, Hamm, RN, Ritchie RH, Klots CE. Radiation damage to a biomolecule: new physical model successfully traces molecular events. Appl. Radiat. Isot. 42, No. 10: 995-1001; 1991.

APPENDIX A

FLUKA INPUT FILES

Mesh Cylinder Geometry

```
TITLE
Mesh Cylinder
*...+....1....+....2....+....3....+....4....+....5....+....6....+....7....+....8
BEAM         -1.5820                                                     HEAVYION
HI-PROPE        22.0       48.0
BEAMPOS          0.0        0.0       -2.0
*...+....1....+....2....+....3....+....4....+....5....+....6....+....7....+....8
GEOBEGIN                                                                 COMBINAT
                         geometry title here
*...+....1....+....2....+....3....+....4....+....5....+....6....+....7....+....8
  RCC    1       0.0        0.0       -8.0        0.0        0.0       16.0
                 8.0
  RCC    2       0.0        0.0       -5.0        0.0        0.0       10.0
                 5.0
  RCC    3       0.0        0.0        0.0        0.0        0.0     0.0016
               0.005
  END
*...+....1......1......1......1......1......1......1......1......1......1......1
  BH1    1     +1      -2
  VA1    2     +2      -3
  WA1    3     +3
  END
GEOEND
*...+....1....+....2....+....3....+....4....+....5....+....6....+....7....+....8
ASSIGNMA         1.0          1
ASSIGNMA         2.0          2
ASSIGNMA        26.0          3
*ASSIGNMA        27.0          5
*MATERIAL         0.0        0.0      1.127       26.0                      TE
*COMPOUND       -10.2        3.0     -77.55        6.0      -3.47       7.0 TE
*COMPOUND        -5.2        8.0      -1.84       21.0      -1.74       8.0 TE
MATERIAL         0.0        0.0        1.0       26.0                     WATER
COMPOUND         2.0        3.0        1.0        8.0                     WATER
EMF                                                                       EMF-ON
*...+....1....+....2....+....3....+....4....+....5....+....6....+....7....+....8
DELTARAY    0.000001        0.0        0.0  HYDROGEN  @LASTMAT           PRINT
*SCORE          208.0
*EVENTDAT          41                                                   edat.out
EVENTYPE         0.0        0.0        2.0        0.0        0.0        0. DPMJET
*EVENTBIN       -10.0      208.0       11.0        0.1        0.1     0.010 Ebin
*EVENTBIN        -0.1       -0.1      0.009      200.0      200.0       1.0 &
USRBIN          11.0      213.0       11.0     0.0005        0.0     0.001 Ebin
USRBIN           0.0        0.0        0.0      500.0        1.0    1000.0 &
USRBIN          11.0      208.0       11.0     0.0005        0.0     0.001 Ebin
USRBIN           0.0        0.0        0.0      500.0        1.0    1000.0 &
USRBIN          11.0      211.0       11.0     0.0005        0.0     0.001 Ebin
USRBIN           0.0        0.0        0.0      500.0        1.0    1000.0 &
*...+....1....+....2....+....3....+....4....+....5....+....6....+....7....+....8
RANDOMIZE        1.0        1.0
START       200000.0
STOP
```

Mesh Cube Geometry

```
TITLE
Mesh Cube
*...+....1....+....2....+....3....+....4....+....5....+....6....+....7....+....8
BEAM           -0.60                                                    HEAVYION
HI-PROPE        22.0      48.0
BEAMPOS          0.0       0.0      -2.0
*...+....1....+....2....+....3....+....4....+....5....+....6....+....7....+....8
GEOBEGIN                                                                COMBINAT
                         geometry title here
*...+....1....+....2....+....3....+....4....+....5....+....6....+....7....+....8
  RCC    1       0.0       0.0      -8.0       0.0       0.0      16.0
                 8.0
  RCC    2       0.0       0.0      -5.0       0.0       0.0      10.0
                 5.0
  RCC    3       0.0       0.0       0.0       0.0       0.0      0.10
                 1.0
  END
*...+....1......1......1......1......1......1......1......1......1......1......1
  BH1    1     +1     -2
  VA1    2     +2     -3
  WA1    3     +3
  END
GEOEND
*...+....1....+....2....+....3....+....4....+....5....+....6....+....7....+....8
ASSIGNMA         1.0         1
ASSIGNMA         2.0         2
ASSIGNMA        26.0         3
*ASSIGNMA        27.0         5
*MATERIAL         0.0       0.0     1.127      26.0                       TE
*COMPOUND       -10.2       3.0    -77.55       6.0     -3.47       7.0 TE
*COMPOUND        -5.2       8.0     -1.84      21.0     -1.74       8.0 TE
MATERIAL         0.0       0.0       1.0      26.0                       WATER
COMPOUND         2.0       3.0       1.0       8.0                       WATER
EMF                                                                      EMF-ON
*...+....1....+....2....+....3....+....4....+....5....+....6....+....7....+....8
DELTARAY    0.000001       0.0       0.0  HYDROGEN  @LASTMAT            PRINT
*SCORE          208.0
*EVENTDAT          41                                                    edat.out
EVENTYPE         0.0       0.0       2.0       0.0       0.0        0. DPMJET
*EVENTBIN       -10.0     208.0      11.0       0.1       0.1     0.010 Ebin
*EVENTBIN        -0.1      -0.1     0.009     200.0     200.0       1.0 &
USRBIN          10.0     213.0      11.0    0.0495    0.0495      0.10 Ebin
USRBIN       -0.0505   -0.0505       0.0     100.0     100.0     100.0 &
USRBIN          10.0     208.0      11.0    0.0495    0.0495      0.10 Ebin
USRBIN       -0.0505   -0.0505       0.0     100.0     100.0     100.0 &
USRBIN          10.0     211.0      11.0    0.0495    0.0495      0.10 Ebin
USRBIN       -0.0505   -0.0505       0.0     100.0     100.0     100.0 &
*...+....1....+....2....+....3....+....4....+....5....+....6....+....7....+....8
RANDOMIZE        1.0       1.0
START       200000.0
STOP
```

Shell Cylinder Geometry

```
TITLE
Shell Cylinders
*...+....1....+....2....+....3....+....4....+....5....+....6....+....7....+....8
BEAM          -1.5820                                                    HEAVYION
HI-PROPE         22.0      48.0
BEAMPOS           0.0       0.0      -4.0
*...+....1....+....2....+....3....+....4....+....5....+....6....+....7....+....8
GEOBEGIN                                                                 COMBINAT
                         geometry title here
*...+....1....+....2....+....3....+....4....+....5....+....6....+....7....+....8
  RCC     1       0.0       0.0      -8.0       0.0       0.0      16.0
                 10.0
  RCC     2       0.0       0.0      -5.0       0.0       0.0      10.0
                  9.0
  RCC     3       0.0       0.0    -0.001       0.0       0.0    0.0012
                  6.0
  RCC     4       0.0       0.0       0.0       0.0       0.0    0.0001
                  1.0
  RCC     5       0.0       0.0       0.0       0.0       0.0    0.0001
                  0.1
  RCC     6       0.0       0.0       0.0       0.0       0.0    0.0001
                 0.01
  RCC     7       0.0       0.0       0.0       0.0       0.0    0.0001
                0.005
  RCC     8       0.0       0.0       0.0       0.0       0.0    0.0001
                0.001
  RCC     9       0.0       0.0       0.0       0.0       0.0    0.0001
               0.0005
  RCC    10       0.0       0.0       0.0       0.0       0.0    0.0001
               0.0001
  RCC    11       0.0       0.0       0.0       0.0       0.0    0.0001
             0.000075
  RCC    12       0.0       0.0       0.0       0.0       0.0    0.0001
              0.00005
  RCC    13       0.0       0.0       0.0       0.0       0.0    0.0001
              0.00003
  RCC    14       0.0       0.0       0.0       0.0       0.0    0.0001
             0.000015
  RCC    15       0.0       0.0       0.0       0.0       0.0    0.0001
              0.00001
  RCC    16       0.0       0.0       0.0       0.0       0.0    0.0001
            0.0000075
  RCC    17       0.0       0.0       0.0       0.0       0.0    0.0001
            0.0000050
  RCC    18       0.0       0.0       0.0       0.0       0.0    0.0001
            0.0000025
  RCC    19       0.0       0.0       0.0       0.0       0.0    0.0001
            0.0000010
  RCC    20       0.0       0.0       0.0       0.0       0.0    0.0001
            0.0000005
  END
*...+....1......1......1......1......1......1......1......1......1......1......1
```

Shell Cylinder Continued

```
  BH1   21     +1     -2
  VA1   21     +2     -3
  SH1   21     +3     -4
  WA1   21     +4     -5
  WA2   21     +5     -6
  WA3   21     +6     -7
  WA4   21     +7     -8
  WA5   21     +8     -9
  WA6   21     +9    -10
  WA7   21    +10    -11
  WA8   21    +11    -12
  WA9   21    +12    -13
  WA10  21    +13    -14
  WA11  21    +14    -15
  WA12  21    +15    -16
  WA13  21    +16    -17
  WA14  21    +17    -18
  WA15  21    +18    -19
  WA16  21    +19    -20
  WA17  21    +20
  END
GEOEND
*...+....1....+....2....+....3....+....4....+....5....+....6....+....7....+....8
ASSIGNMA         1.0         1
ASSIGNMA         2.0         2
ASSIGNMA        26.0         3
ASSIGNMA        26.0         4
ASSIGNMA        26.0         5
ASSIGNMA        26.0         6
ASSIGNMA        26.0         7
ASSIGNMA        26.0         8
ASSIGNMA        26.0         9
ASSIGNMA        26.0        10
ASSIGNMA        26.0        11
ASSIGNMA        26.0        12
ASSIGNMA        26.0        13
ASSIGNMA        26.0        14
ASSIGNMA        26.0        15
ASSIGNMA        26.0        16
ASSIGNMA        26.0        17
ASSIGNMA        26.0        18
ASSIGNMA        26.0        19
ASSIGNMA        26.0        20
*ASSIGNMA        27.0         5
*MATERIAL         0.0        0.0     1.127      26.0                    TE
*COMPOUND       -10.2        3.0    -77.55       6.0     -3.47       7.0 TE
*COMPOUND        -5.2        8.0     -1.84      21.0     -1.74       8.0 TE
MATERIAL         0.0       0.0       1.0      26.0                       WATER
COMPOUND         2.0       3.0       1.0       8.0                       WATER
EMF                                                                      EMF-ON
*...+....1....+....2....+....3....+....4....+....5....+....6....+....7....+....8
DELTARAY    0.000001       0.0       0.0  HYDROGEN  @LASTMAT            PRINT
SCORE          208.0
EVENTDAT          41                                                    edat.out
EVENTYPE         0.0       0.0       2.0       0.0       0.0        0. DPMJET
*...+....1....+....2....+....3....+....4....+....5....+....6....+....7....+....8
RANDOMIZE        1.0       1.0
START       200000.0
STOP
```

APPENDIX B

DOSIMETRY DATA FOR CUBE AND CYLINDER MESH GEOMETRIES

Table B1. Dose (Gy) deposited in voxels inside the cube mesh geometry by ions of equal stopping power (100 keV um^{-1}). FLUKA data is scaled as GeV-cm^{-3} and described in the 'Bin' column. Un-hit voxels appear in the first row for each ion. The number of hit voxels is summed and listed at the bottom of the table.

Dose (Gy)	*Bin*	Be-8 *Voxels Hit*	C-12 *Voxels Hit*	O-16 *Voxels Hit*	Mg-24 *Voxels Hit*	Si-28 *Voxels Hit*	Ca-40 *Voxels Hit*	Ti-48 *Voxels Hit*
1.60E-12	1.00E-05	997388	962301	946704	329456	4485	3	0
1.71E-12	1.07E-05	0	0	0	2	0	0	0
1.83E-12	1.14E-05	0	0	0	1	0	0	0
1.95E-12	1.22E-05	0	0	0	2	0	0	0
2.08E-12	1.30E-05	0	0	0	1	1	0	0
2.22E-12	1.39E-05	0	0	0	2	2	0	0
2.38E-12	1.48E-05	0	0	0	0	0	0	0
2.54E-12	1.58E-05	0	0	0	3	2	0	0
2.71E-12	1.69E-05	0	0	0	5	1	0	0
2.89E-12	1.80E-05	0	0	0	5	0	0	0
3.09E-12	1.93E-05	0	0	1	6	0	0	0
3.30E-12	2.06E-05	0	0	0	3	1	0	0
3.52E-12	2.20E-05	0	0	0	5	0	0	0
3.76E-12	2.35E-05	0	0	1	6	0	0	0
4.01E-12	2.51E-05	0	0	0	7	0	0	0
4.29E-12	2.68E-05	0	0	0	7	0	0	0
4.58E-12	2.86E-05	0	0	0	2	0	0	0
4.89E-12	3.05E-05	0	0	0	7	1	0	0
5.22E-12	3.26E-05	0	0	0	3	0	0	0
5.57E-12	3.48E-05	0	1	0	3	3	0	0
5.95E-12	3.71E-05	0	0	0	3	3	0	0
6.35E-12	3.97E-05	0	0	0	6	2	0	0
6.79E-12	4.24E-05	0	1	0	8	3	0	0
7.25E-12	4.52E-05	0	0	0	8	3	0	0
7.74E-12	4.83E-05	0	0	0	6	0	0	0
8.26E-12	5.16E-05	0	0	2	9	0	1	0
8.82E-12	5.51E-05	0	0	0	9	0	0	0
9.42E-12	5.88E-05	0	0	0	4	2	0	0

1.01E-11	6.28E-05	0	0	0	7	0	0	0
1.07E-11	6.70E-05	0	1	0	4	2	0	0
1.15E-11	7.16E-05	0	1	0	12	1	0	0
1.22E-11	7.64E-05	0	2	0	10	2	0	0
1.31E-11	8.16E-05	0	0	0	16	5	0	0
1.40E-11	8.72E-05	0	2	1	23	2	0	0
1.49E-11	9.31E-05	0	1	2	15	2	0	0
1.59E-11	9.94E-05	0	0	0	10	2	0	0
1.70E-11	1.06E-04	0	0	2	16	5	0	0
1.82E-11	1.13E-04	0	1	1	19	6	0	0
1.94E-11	1.21E-04	1	0	2	22	5	0	0
2.07E-11	1.29E-04	0	1	1	18	4	0	0
2.21E-11	1.38E-04	0	1	1	21	1	0	0
2.36E-11	1.47E-04	0	0	3	13	7	0	0
2.52E-11	1.57E-04	0	2	4	18	6	0	0
2.69E-11	1.68E-04	0	1	2	21	6	0	0
2.87E-11	1.79E-04	0	2	1	19	3	0	0
3.07E-11	1.92E-04	0	1	5	23	7	0	0
3.28E-11	2.05E-04	0	2	6	32	7	0	0
3.50E-11	2.18E-04	0	1	6	32	5	0	0
3.74E-11	2.33E-04	0	1	4	34	6	0	0
3.99E-11	2.49E-04	0	2	6	36	2	0	0
4.26E-11	2.66E-04	0	3	5	44	13	0	0
4.55E-11	2.84E-04	0	4	7	48	13	0	0
4.86E-11	3.03E-04	0	4	1	51	7	0	0
5.19E-11	3.24E-04	0	8	6	41	12	0	0
5.54E-11	3.46E-04	0	3	4	60	9	0	0
5.91E-11	3.69E-04	0	1	5	52	11	0	0
6.32E-11	3.94E-04	0	3	3	61	12	0	0
6.74E-11	4.21E-04	0	2	6	51	9	0	0
7.20E-11	4.49E-04	1	2	3	76	7	0	0
7.69E-11	4.80E-04	1	1	4	65	17	0	0
8.21E-11	5.12E-04	0	3	10	68	14	0	0
8.77E-11	5.47E-04	0	1	3	68	17	2	0
9.36E-11	5.84E-04	1	6	12	75	15	0	0
1.00E-10	6.24E-04	0	6	9	78	21	0	0
1.07E-10	6.66E-04	0	3	7	99	19	0	0
1.14E-10	7.11E-04	0	4	8	107	17	0	0
1.22E-10	7.60E-04	0	5	5	108	18	0	0
1.30E-10	8.11E-04	0	0	12	106	30	0	0

1.39E-10	8.66E-04	0	6	7	122	29	0	0
1.48E-10	9.25E-04	0	5	4	120	28	0	0
1.58E-10	9.88E-04	0	6	23	150	39	0	0
1.69E-10	1.05E-03	1	10	17	139	36	0	0
1.80E-10	1.13E-03	0	17	25	163	29	0	0
1.93E-10	1.20E-03	2	12	22	159	33	0	0
2.06E-10	1.28E-03	1	14	24	193	48	0	0
2.20E-10	1.37E-03	0	21	23	219	39	0	0
2.35E-10	1.46E-03	0	16	29	204	33	0	0
2.51E-10	1.56E-03	1	19	29	195	37	0	0
2.67E-10	1.67E-03	3	22	19	229	58	0	0
2.86E-10	1.78E-03	0	19	29	275	51	0	0
3.05E-10	1.90E-03	1	12	37	270	52	0	0
3.26E-10	2.03E-03	0	26	28	300	72	0	0
3.48E-10	2.17E-03	2	25	45	305	74	0	0
3.71E-10	2.32E-03	1	22	48	296	82	0	0
3.97E-10	2.47E-03	2	17	43	343	67	0	0
4.23E-10	2.64E-03	2	33	32	404	86	0	0
4.52E-10	2.82E-03	2	30	43	396	76	1	0
4.83E-10	3.01E-03	1	28	39	447	78	0	0
5.16E-10	3.22E-03	0	35	61	437	88	0	0
5.50E-10	3.44E-03	1	26	52	461	127	0	0
5.88E-10	3.67E-03	4	36	51	530	120	3	0
6.28E-10	3.92E-03	3	30	56	600	116	0	0
6.70E-10	4.18E-03	6	37	60	589	121	2	0
7.16E-10	4.47E-03	2	44	66	619	148	1	1
7.64E-10	4.77E-03	1	49	60	679	156	0	0
8.16E-10	5.09E-03	4	64	69	831	140	2	0
8.71E-10	5.44E-03	1	46	77	1096	174	0	0
9.30E-10	5.81E-03	8	58	76	1056	188	1	0
9.94E-10	6.20E-03	4	40	96	1172	209	1	0
1.06E-09	6.62E-03	4	65	99	1183	190	1	0
1.13E-09	7.07E-03	8	70	99	1137	232	2	0
1.21E-09	7.55E-03	9	88	102	1193	251	4	0
1.29E-09	8.06E-03	11	82	116	1294	281	3	0
1.38E-09	8.61E-03	26	70	127	1364	302	2	0
1.47E-09	9.19E-03	31	133	137	1455	337	3	1
1.57E-09	9.82E-03	54	124	131	1510	398	4	0
1.68E-09	1.05E-02	50	193	153	1621	406	2	1
1.79E-09	1.12E-02	86	212	177	1657	464	4	0

1.91E-09	1.20E-02	73	288	216	1779	507	4	2
2.04E-09	1.28E-02	100	356	287	1960	499	5	2
2.18E-09	1.36E-02	122	438	396	2034	620	5	1
2.33E-09	1.46E-02	130	582	492	2176	629	8	0
2.49E-09	1.55E-02	120	710	665	2415	699	4	1
2.66E-09	1.66E-02	145	898	855	2677	746	12	1
2.84E-09	1.77E-02	102	1033	1072	2784	790	18	6
3.03E-09	1.89E-02	147	1128	1200	3007	872	12	2
3.24E-09	2.02E-02	123	1146	1464	3316	893	11	6
3.46E-09	2.16E-02	136	1249	1519	3411	942	16	4
3.69E-09	2.30E-02	120	1228	1618	3821	1085	15	5
3.94E-09	2.46E-02	104	1259	1646	3876	1105	21	4
4.21E-09	2.63E-02	87	1243	1591	4160	1185	32	10
4.49E-09	2.80E-02	92	1093	1556	4375	1314	38	9
4.80E-09	2.99E-02	63	995	1499	4380	1387	40	13
5.12E-09	3.20E-02	60	1009	1348	4501	1473	64	8
5.47E-09	3.41E-02	51	901	1254	4710	1589	76	19
5.84E-09	3.65E-02	47	708	1102	4834	1790	67	15
6.24E-09	3.89E-02	35	624	1029	4853	1846	80	23
6.66E-09	4.16E-02	22	592	863	4977	2015	95	37
7.11E-09	4.44E-02	35	513	736	4995	2229	113	32
7.60E-09	4.74E-02	30	443	657	5099	2307	132	48
8.11E-09	5.06E-02	22	382	578	5147	2511	163	50
8.66E-09	5.41E-02	27	328	462	5380	2774	192	56
9.25E-09	5.77E-02	17	324	456	5411	2934	232	80
9.87E-09	6.16E-02	14	253	360	5449	3148	277	93
1.05E-08	6.58E-02	23	253	368	5672	3369	336	115
1.13E-08	7.03E-02	11	263	300	5791	3494	327	160
1.20E-08	7.50E-02	4	212	304	5802	3726	408	178
1.28E-08	8.01E-02	9	210	292	5979	4019	522	198
1.37E-08	8.56E-02	16	179	254	6215	4367	547	275
1.46E-08	9.14E-02	13	162	230	6191	4672	627	327
1.56E-08	9.76E-02	7	170	245	6260	4898	725	355
1.67E-08	1.04E-01	10	153	230	6395	5409	861	440
1.78E-08	1.11E-01	10	134	244	6653	5725	946	531
1.90E-08	1.19E-01	4	136	222	6597	5928	1157	617
2.03E-08	1.27E-01	4	138	223	6717	6406	1236	658
2.17E-08	1.35E-01	6	137	218	6854	6939	1411	821
2.32E-08	1.45E-01	12	115	207	6744	7235	1532	1008
2.47E-08	1.54E-01	15	113	184	6741	7700	1794	1133

2.64E-08	1.65E-01	16	142	186	6806	7999	2020	1323
2.82E-08	1.76E-01	11	122	199	6858	8685	2269	1514
3.01E-08	1.88E-01	13	123	171	6788	9131	2366	1659
3.22E-08	2.01E-01	9	101	178	6871	9621	2792	1983
3.44E-08	2.14E-01	8	107	174	6686	9872	3075	2216
3.67E-08	2.29E-01	4	103	168	6763	10349	3433	2467
3.92E-08	2.44E-01	8	110	157	6708	11010	3727	2876
4.18E-08	2.61E-01	5	96	166	6816	11462	4048	3271
4.47E-08	2.79E-01	2	96	167	6777	11898	4417	3490
4.77E-08	2.98E-01	0	98	143	6779	12620	4971	3998
5.09E-08	3.18E-01	1	70	143	6709	13043	5264	4353
5.44E-08	3.39E-01	0	84	158	6626	13592	5747	4721
5.81E-08	3.62E-01	1	106	150	6692	14176	6360	5180
6.20E-08	3.87E-01	0	87	166	6760	14779	6975	5591
6.62E-08	4.13E-01	0	68	153	6640	15309	7454	6059
7.07E-08	4.41E-01	0	90	157	6683	15626	8063	6708
7.55E-08	4.71E-01	0	80	180	6664	15986	8868	7311
8.06E-08	5.03E-01	0	86	169	6670	16811	9415	8009
8.61E-08	5.37E-01	0	82	178	6652	16851	10264	8450
9.19E-08	5.74E-01	0	79	143	6667	17476	11325	9367
9.81E-08	6.13E-01	0	74	154	6578	17681	12221	10171
1.05E-07	6.54E-01	0	102	187	6498	17630	13096	11268
1.12E-07	6.98E-01	0	102	181	6724	17585	14247	12244
1.19E-07	7.46E-01	0	102	156	6656	17501	15223	13063
1.28E-07	7.96E-01	0	106	143	6484	17559	16348	14074
1.36E-07	8.50E-01	0	116	180	6525	17246	17390	15418
1.45E-07	9.08E-01	0	119	145	6546	17043	18318	16952
1.55E-07	9.70E-01	0	158	167	6299	16742	19569	17865
1.66E-07	1.04E+00	0	167	153	6298	16226	20901	19217
1.77E-07	1.11E+00	0	218	213	6323	15998	21479	20544
1.89E-07	1.18E+00	0	286	187	6155	15765	22888	21681
2.02E-07	1.26E+00	0	345	241	6185	15279	23767	23111
2.16E-07	1.35E+00	0	409	229	6163	14944	24586	24250
2.30E-07	1.44E+00	0	463	246	6019	14477	25189	25366
2.46E-07	1.53E+00	0	580	220	6022	14418	25282	26272
2.63E-07	1.64E+00	0	536	247	6043	13815	25241	26773
2.80E-07	1.75E+00	0	571	206	5887	13290	24554	26967
2.99E-07	1.87E+00	0	419	181	5757	13053	24103	26776
3.20E-07	2.00E+00	0	343	161	5905	12652	23169	25820
3.41E-07	2.13E+00	0	250	176	5711	12267	22509	25244

3.65E-07	2.28E+00	0	176	164	5608	11925	21672	24228
3.89E-07	2.43E+00	0	144	131	5653	11826	20688	23458
4.16E-07	2.59E+00	0	131	148	5479	11336	20083	22177
4.44E-07	2.77E+00	0	164	166	5398	10978	19216	21353
4.74E-07	2.96E+00	0	170	169	5366	10654	18260	20595
5.06E-07	3.16E+00	0	160	153	5237	10327	17683	19706
5.40E-07	3.37E+00	0	165	167	5157	10208	16797	18869
5.77E-07	3.60E+00	0	171	185	5032	9850	16226	17869
6.16E-07	3.85E+00	0	138	181	4942	9201	15441	17363
6.58E-07	4.11E+00	0	113	193	4828	9087	14804	16496
7.03E-07	4.39E+00	0	118	184	4751	8822	14305	15784
7.50E-07	4.68E+00	0	111	179	4694	8546	13416	15198
8.01E-07	5.00E+00	0	111	158	4633	8243	13071	14419
8.55E-07	5.34E+00	0	123	170	4576	7787	12305	13622
9.13E-07	5.70E+00	0	96	171	4382	7631	11847	12897
9.75E-07	6.09E+00	0	84	158	4358	7346	11327	12424
1.04E-06	6.50E+00	0	78	162	4138	6968	10927	11882
1.11E-06	6.94E+00	0	91	166	4062	6829	10200	11263
1.19E-06	7.41E+00	0	89	146	4048	6659	9869	10608
1.27E-06	7.91E+00	0	101	161	3864	6318	9329	10244
1.35E-06	8.45E+00	0	73	157	3806	6019	9013	9572
1.45E-06	9.02E+00	0	86	169	3751	5862	8587	9024
1.54E-06	9.64E+00	0	81	140	3641	5678	8079	8698
1.65E-06	1.03E+01	0	93	159	3476	5340	7608	8198
1.76E-06	1.10E+01	0	86	171	3428	5064	7279	7751
1.88E-06	1.17E+01	0	93	197	3223	4957	7080	7342
2.01E-06	1.25E+01	0	89	165	3231	4726	6553	7067
2.14E-06	1.34E+01	0	81	183	3098	4431	6227	6667
2.29E-06	1.43E+01	0	80	171	2913	4285	5876	6284
2.44E-06	1.53E+01	0	79	156	2982	4263	5773	5865
2.61E-06	1.63E+01	0	77	157	2783	3938	5344	5526
2.79E-06	1.74E+01	0	75	177	2693	3699	5116	5186
2.98E-06	1.86E+01	0	67	177	2739	3651	4733	4883
3.18E-06	1.98E+01	0	76	179	2492	3489	4655	4843
3.39E-06	2.12E+01	0	71	163	2335	3376	4348	4362
3.62E-06	2.26E+01	0	64	157	2414	3028	3961	4152
3.87E-06	2.41E+01	0	58	181	2291	3143	3933	3801
4.13E-06	2.58E+01	0	50	174	1961	2797	3592	3759
4.41E-06	2.75E+01	0	58	187	2134	2716	3496	3333
4.71E-06	2.94E+01	0	50	165	2160	2707	3088	3307

5.03E-06	3.14E+01	0	59	154	1753	2382	3246	2977
5.37E-06	3.35E+01	0	39	159	1903	2358	2741	2904
5.73E-06	3.58E+01	0	56	167	1929	2370	2804	2782
6.12E-06	3.82E+01	0	51	183	1645	2000	2539	2354
6.54E-06	4.08E+01	0	71	167	1426	2130	2316	2525
6.98E-06	4.36E+01	0	61	164	1634	1951	2491	2185
7.46E-06	4.65E+01	0	85	156	1800	1730	2024	1995
7.96E-06	4.97E+01	0	59	193	1059	1680	1900	2294
8.50E-06	5.31E+01	0	61	206	1270	1942	2257	1530
9.08E-06	5.67E+01	0	42	174	1562	1337	1484	1679
9.69E-06	6.05E+01	0	49	138	1372	1418	1666	1995
1.04E-05	6.46E+01	0	36	91	858	1663	1905	1221
1.11E-05	6.90E+01	0	38	92	1185	1349	1188	1426
1.18E-05	7.37E+01	0	43	104	987	1073	1418	1353
1.26E-05	7.87E+01	0	46	129	1421	1141	1338	1512
1.35E-05	8.40E+01	0	43	147	847	1383	1506	965
1.44E-05	8.97E+01	0	30	185	749	1143	970	728
1.53E-05	9.58E+01	0	25	217	630	829	674	1624
1.64E-05	1.02E+02	0	34	222	1315	667	1501	923
1.75E-05	1.09E+02	0	20	166	936	1328	1086	689
1.87E-05	1.17E+02	0	23	181	497	1044	636	662
1.99E-05	1.25E+02	0	26	214	473	528	552	995
2.13E-05	1.33E+02	0	25	180	939	537	1125	890
2.27E-05	1.42E+02	0	27	140	578	1062	778	789
2.43E-05	1.52E+02	0	15	88	840	577	752	464
2.59E-05	1.62E+02	0	16	87	659	785	594	357
2.77E-05	1.73E+02	0	16	92	411	664	280	524
2.96E-05	1.85E+02	0	8	112	232	383	661	751
3.16E-05	1.97E+02	0	14	135	646	456	457	1061
3.37E-05	2.10E+02	0	10	162	242	406	1326	45
3.60E-05	2.25E+02	0	12	174	1068	809	83	55
3.84E-05	2.40E+02	0	12	67	484	843	46	658
4.11E-05	2.56E+02	1	10	5	38	37	429	154
4.38E-05	2.74E+02	0	8	15	89	95	360	549
4.68E-05	2.92E+02	0	12	62	610	572	420	721
5.00E-05	3.12E+02	0	11	216	168	218	732	183
5.34E-05	3.33E+02	0	8	208	439	454	336	20
5.70E-05	3.56E+02	0	14	276	654	643	19	212
6.09E-05	3.80E+02	0	10	164	300	312	42	547
6.50E-05	4.06E+02	0	9	147	28	26	715	9

6.94E-05	4.33E+02	0	10	96	62	81	8	25
7.41E-05	4.63E+02	0	14	134	565	644	27	214
7.91E-05	4.94E+02	0	10	198	123	24	41	562
8.45E-05	5.27E+02	0	10	39	23	27	735	359
9.02E-05	5.63E+02	0	10	0	46	60	141	31
9.63E-05	6.01E+02	0	12	0	323	692	245	371
1.03E-04	6.42E+02	0	9	5	411	91	303	0
1.10E-04	6.86E+02	0	4	7	324	298	72	0
1.17E-04	7.32E+02	0	3	0	70	148	0	2
1.25E-04	7.82E+02	0	5	0	328	226	8	14
1.34E-04	8.35E+02	0	45	8	10	0	1	0
1.43E-04	8.91E+02	0	60	15	2	0	7	15
1.52E-04	9.52E+02	0	40	43	10	8	8	742
1.63E-04	1.02E+03	0	35	716	5	5	136	27
1.74E-04	1.09E+03	0	32	2	8	23	640	3
1.86E-04	1.16E+03	0	27	4	27	64	0	45
1.98E-04	1.24E+03	0	31	4	190	692	11	340
2.12E-04	1.32E+03	0	11	182	551	5	377	0
2.26E-04	1.41E+03	0	4	177	10	8	0	0
2.41E-04	1.51E+03	0	4	21	21	267	0	0
2.58E-04	1.61E+03	0	4	0	299	112	4	4
2.75E-04	1.72E+03	0	4	0	61	0	0	0
2.94E-04	1.83E+03	0	2	0	0	0	0	0
3.14E-04	1.96E+03	0	3	0	0	0	0	0
3.35E-04	2.09E+03	0	8	1	0	0	0	0
3.58E-04	2.23E+03	0	4	3	0	0	0	4
3.82E-04	2.38E+03	0	4	0	0	0	4	6
4.08E-04	2.55E+03	0	4	0	3	2	4	386
4.36E-04	2.72E+03	0	3	4	1	2	337	0
4.65E-04	2.90E+03	0	3	0	0	8	51	0
4.97E-04	3.10E+03	0	2	9	8	33	0	0
5.30E-04	3.31E+03	0	4	120	67	351	0	0
5.66E-04	3.54E+03	0	4	114	317	0	0	0
6.05E-04	3.78E+03	0	4	54	0	0	0	1
6.46E-04	4.03E+03	0	4	42	4	4	3	3
6.90E-04	4.30E+03	0	8	32	0	0	1	0
7.36E-04	4.60E+03	0	77	21	0	0	0	0
7.86E-04	4.91E+03	0	80	0	0	0	0	4
8.40E-04	5.24E+03	0	20	0	0	0	4	392
8.97E-04	5.60E+03	0	14	0	0	0	4	0

9.57E-04	5.98E+03	0	11	4	0	0	388	0
1.02E-03	6.38E+03	0	10	0	4	10	0	0
1.09E-03	6.81E+03	0	13	3	8	361	0	0
1.17E-03	7.28E+03	0	17	6	264	25	0	0
1.24E-03	7.77E+03	0	13	103	120	0	0	0
1.33E-03	8.30E+03	0	15	81	0	0	0	0
1.42E-03	8.86E+03	0	14	43	0	0	0	0
1.52E-03	9.46E+03	0	10	30	0	0	0	0
1.62E-03	1.01E+04	0	9	23	0	0	0	0
1.73E-03	1.08E+04	0	9	17	0	0	0	0
1.85E-03	1.15E+04	0	11	17	0	0	0	0
1.97E-03	1.23E+04	0	6	13	0	0	0	0
2.10E-03	1.31E+04	0	6	12	0	0	0	0
2.25E-03	1.40E+04	0	5	12	0	0	0	0
2.40E-03	1.50E+04	0	4	12	0	0	0	0
2.56E-03	1.60E+04	0	4	10	0	0	0	0
2.74E-03	1.71E+04	0	7	10	0	0	0	0
2.92E-03	1.82E+04	0	5	0	0	0	0	0
3.12E-03	1.95E+04	0	6	0	0	0	0	0
3.33E-03	2.08E+04	0	6	0	0	0	0	0
3.56E-03	2.22E+04	0	8	0	0	0	0	0
3.80E-03	2.37E+04	0	4	0	0	0	0	0
4.06E-03	2.53E+04	0	8	0	0	0	0	0
4.33E-03	2.70E+04	0	8	0	0	0	0	0
4.62E-03	2.89E+04	0	8	0	0	0	0	0
4.94E-03	3.08E+04	0	12	0	0	0	0	0
5.27E-03	3.29E+04	0	8	0	0	0	0	0
5.63E-03	3.51E+04	0	12	0	0	0	0	0
6.01E-03	3.75E+04	0	12	0	0	0	0	0
6.42E-03	4.01E+04	0	12	0	0	0	0	0
6.85E-03	4.28E+04	0	0	0	0	0	0	0
7.32E-03	4.57E+04	0	0	0	0	0	0	0
7.82E-03	4.88E+04	0	0	0	0	0	0	0
8.35E-03	5.21E+04	0	0	0	0	0	0	0
8.91E-03	5.56E+04	0	0	0	0	0	0	0
9.52E-03	5.94E+04	0	0	0	0	0	0	0
1.02E-02	6.34E+04	0	0	0	0	0	0	0
1.09E-02	6.77E+04	0	0	0	0	0	0	0
1.16E-02	7.23E+04	0	0	0	0	0	0	0
1.24E-02	7.72E+04	0	0	0	0	0	0	0

1.32E-02	8.25E+04	0	0	0	0	0	0	0
1.41E-02	8.80E+04	0	0	0	0	0	0	0
1.51E-02	9.40E+04	0	0	0	0	0	0	0
1.61E-02	1.00E+05	0	0	0	0	0	0	0
1.72E-02	1.07E+05	0	0	0	0	0	0	0
1.83E-02	1.14E+05	0	0	0	0	0	0	0
1.96E-02	1.22E+05	0	0	0	0	0	0	0
2.09E-02	1.31E+05	0	0	0	0	0	0	0
2.23E-02	1.39E+05	0	0	0	0	0	0	0
2.38E-02	1.49E+05	3	3	0	0	0	0	0
2.55E-02	1.59E+05	5	5	0	0	0	0	100
2.72E-02	1.70E+05	5	4	0	0	0	1	0
2.90E-02	1.81E+05	4	5	0	0	0	99	0
3.10E-02	1.93E+05	4	5	0	0	1	0	0
3.31E-02	2.07E+05	2	6	0	1	99	0	0
3.53E-02	2.21E+05	3	8	0	99	0	0	0
3.77E-02	2.36E+05	1	7	1	0	0	0	0
4.03E-02	2.52E+05	2	2	21	0	0	0	0
4.30E-02	2.69E+05	0	1	78	0	0	0	0
4.60E-02	2.87E+05	0	16	0	0	0	0	0
4.91E-02	3.06E+05	0	15	0	0	0	0	0
5.24E-02	3.27E+05	0	23	0	0	0	0	0
5.60E-02	3.49E+05	0	0	0	0	0	0	0
5.97E-02	3.73E+05	0	0	0	0	0	0	0
6.38E-02	3.98E+05	0	0	0	0	0	0	0
6.81E-02	4.25E+05	0	0	0	0	0	0	0
7.27E-02	4.54E+05	0	0	0	0	0	0	0
7.77E-02	4.85E+05	0	0	0	0	0	0	0
8.29E-02	5.18E+05	0	0	0	0	0	0	0
# Cells Affected --->		2612	37699	53296	670544	995515	999997	1000000

Table B2. Electron fluence (electrons / 1000 nm^2) in voxels inside the mesh cube by ions of equal stopping power (100 keV um^{-1}). FLUKA data is scaled as electrons-cm^{-2} and described in the 'Bin' column. Un-hit voxels appear in the first row for each ion. The number of hit voxels is summed and listed at the bottom of the table.

Electron Fluence	Bin	Be-8 Voxels Hit	C-12 Voxels Hit	O-16 Voxels Hit	Mg-24 Voxels Hit	Si-28 Voxels Hit	Ca-40 Voxels Hit	Ti-48 Voxels Hit
1.00E-10	1.00E-04	997381	962393	946903	329473	4473	3	0
1.08E-10	1.08E-04	0	0	0	0	0	0	0
1.17E-10	1.17E-04	0	0	0	0	0	0	0
1.26E-10	1.26E-04	0	1	0	0	0	0	0
1.36E-10	1.36E-04	0	0	0	1	0	0	0
1.47E-10	1.47E-04	0	0	0	0	0	0	0
1.59E-10	1.59E-04	0	0	0	0	0	0	0
1.72E-10	1.72E-04	0	0	0	0	0	0	0
1.85E-10	1.85E-04	0	0	0	1	0	0	0
2.00E-10	2.00E-04	0	0	0	0	0	0	0
2.16E-10	2.16E-04	0	0	0	0	0	0	0
2.34E-10	2.34E-04	0	0	1	0	0	0	0
2.52E-10	2.52E-04	0	0	0	0	0	0	0
2.73E-10	2.73E-04	0	1	0	1	0	0	0
2.94E-10	2.94E-04	0	0	1	0	0	0	0
3.18E-10	3.18E-04	0	1	0	1	0	0	0
3.43E-10	3.43E-04	0	1	0	2	0	0	0
3.71E-10	3.71E-04	0	0	0	1	0	0	0
4.01E-10	4.01E-04	0	0	1	0	0	0	0
4.33E-10	4.33E-04	0	0	0	2	0	0	0
4.68E-10	4.68E-04	1	0	0	1	0	0	0
5.05E-10	5.05E-04	0	0	0	2	0	0	0
5.46E-10	5.46E-04	0	0	0	0	0	0	0
5.89E-10	5.89E-04	0	0	0	0	0	0	0
6.37E-10	6.37E-04	0	1	0	1	0	0	0
6.88E-10	6.88E-04	0	1	1	0	0	0	0
7.43E-10	7.43E-04	0	0	1	2	1	0	0
8.02E-10	8.02E-04	0	0	1	0	0	0	0
8.67E-10	8.67E-04	0	0	0	1	1	0	0
9.36E-10	9.36E-04	0	0	1	1	0	0	0
1.01E-09	1.01E-03	0	0	1	3	0	0	0
1.09E-09	1.09E-03	0	0	1	5	0	0	0
1.18E-09	1.18E-03	0	1	2	1	0	0	0
1.27E-09	1.27E-03	0	3	2	3	0	0	0

1.38E-09	1.38E-03	0	0	0	1	0	0	0
1.49E-09	1.49E-03	0	1	2	7	0	0	0
1.61E-09	1.61E-03	0	0	1	3	0	0	0
1.74E-09	1.74E-03	0	0	5	0	0	0	0
1.87E-09	1.87E-03	0	1	2	4	0	0	0
2.02E-09	2.02E-03	0	1	2	4	0	0	0
2.19E-09	2.19E-03	0	2	0	7	0	0	0
2.36E-09	2.36E-03	0	5	3	3	2	0	0
2.55E-09	2.55E-03	0	2	2	3	0	0	0
2.76E-09	2.76E-03	0	3	1	7	0	0	0
2.98E-09	2.98E-03	0	1	4	1	2	0	0
3.22E-09	3.22E-03	0	0	1	3	0	0	0
3.47E-09	3.47E-03	0	3	2	6	0	0	0
3.75E-09	3.75E-03	0	1	1	5	1	0	0
4.05E-09	4.05E-03	1	3	3	10	0	0	0
4.38E-09	4.38E-03	0	0	4	9	0	0	0
4.73E-09	4.73E-03	0	7	1	7	1	0	0
5.11E-09	5.11E-03	0	2	8	1	0	0	0
5.52E-09	5.52E-03	1	6	4	5	0	0	0
5.96E-09	5.96E-03	2	3	6	11	1	0	0
6.44E-09	6.44E-03	0	0	7	28	3	0	0
6.95E-09	6.95E-03	1	7	5	65	1	0	0
7.51E-09	7.51E-03	1	3	10	52	1	0	0
8.11E-09	8.11E-03	0	8	3	82	2	0	0
8.76E-09	8.76E-03	0	5	3	107	0	0	0
9.47E-09	9.47E-03	0	6	9	99	2	0	0
1.02E-08	1.02E-02	0	10	9	227	2	0	0
1.10E-08	1.10E-02	2	6	17	126	1	0	0
1.19E-08	1.19E-02	4	12	10	95	1	0	0
1.29E-08	1.29E-02	4	7	12	58	0	0	0
1.39E-08	1.39E-02	3	13	15	52	1	0	0
1.50E-08	1.50E-02	2	11	12	41	1	0	0
1.62E-08	1.62E-02	5	10	14	50	2	0	0
1.75E-08	1.75E-02	0	14	18	91	3	0	0
1.90E-08	1.90E-02	3	19	11	115	4	0	0
2.05E-08	2.05E-02	5	22	25	131	1	0	0
2.21E-08	2.21E-02	3	25	19	166	3	0	0
2.39E-08	2.39E-02	8	20	19	166	2	1	0
2.58E-08	2.58E-02	11	23	24	120	2	0	0
2.79E-08	2.79E-02	10	22	19	103	3	0	0

3.01E-08	3.01E-02	6	26	25	120	4	0	0
3.25E-08	3.25E-02	14	39	29	159	2	0	0
3.51E-08	3.51E-02	17	30	25	169	8	0	0
3.79E-08	3.79E-02	18	46	40	193	6	0	0
4.10E-08	4.10E-02	11	53	47	165	9	0	0
4.43E-08	4.43E-02	21	66	42	178	9	0	0
4.78E-08	4.78E-02	25	70	45	183	1	0	0
5.17E-08	5.17E-02	21	77	57	172	8	0	0
5.58E-08	5.58E-02	27	84	65	233	5	0	0
6.03E-08	6.03E-02	41	102	88	236	12	0	0
6.51E-08	6.51E-02	43	126	84	225	7	0	0
7.03E-08	7.03E-02	47	133	107	221	5	0	0
7.60E-08	7.60E-02	37	151	115	217	10	0	0
8.20E-08	8.20E-02	55	176	145	242	7	0	0
8.86E-08	8.86E-02	56	222	201	259	4	0	0
9.57E-08	9.57E-02	78	247	194	250	14	0	0
1.03E-07	1.03E-01	62	298	247	292	14	0	0
1.12E-07	1.12E-01	79	323	283	292	8	0	0
1.21E-07	1.21E-01	94	350	328	297	19	0	0
1.30E-07	1.30E-01	90	433	385	292	11	0	0
1.41E-07	1.41E-01	79	454	433	335	17	0	0
1.52E-07	1.52E-01	90	519	498	363	16	0	0
1.64E-07	1.64E-01	73	590	559	355	24	0	0
1.77E-07	1.77E-01	82	596	603	371	22	0	0
1.92E-07	1.92E-01	92	696	723	394	25	0	0
2.07E-07	2.07E-01	95	673	734	400	24	0	0
2.24E-07	2.24E-01	108	758	850	470	28	2	0
2.42E-07	2.42E-01	115	783	899	466	28	0	0
2.61E-07	2.61E-01	73	830	931	475	41	0	0
2.82E-07	2.82E-01	92	824	1003	532	32	0	0
3.04E-07	3.04E-01	70	793	1026	595	54	0	0
3.29E-07	3.29E-01	83	852	1086	612	41	0	0
3.55E-07	3.55E-01	58	837	1032	619	38	0	0
3.84E-07	3.84E-01	76	839	1053	699	40	0	0
4.14E-07	4.14E-01	61	769	917	693	55	0	0
4.48E-07	4.48E-01	51	763	957	786	46	0	0
4.84E-07	4.84E-01	57	688	977	753	52	0	0
5.22E-07	5.22E-01	42	684	941	814	64	0	0
5.64E-07	5.64E-01	31	622	902	887	74	0	0
6.09E-07	6.09E-01	34	570	840	920	79	0	0

6.58E-07	6.58E-01	33	587	773	944	79	0	0
7.11E-07	7.11E-01	29	466	769	993	89	0	0
7.68E-07	7.68E-01	22	453	648	1056	101	0	0
8.30E-07	8.30E-01	19	429	588	1138	91	0	0
8.96E-07	8.96E-01	23	370	512	1167	129	0	0
9.68E-07	9.68E-01	14	321	524	1239	129	0	0
1.05E-06	1.05E+00	13	306	437	1338	143	0	0
1.13E-06	1.13E+00	6	274	380	1414	135	0	0
1.22E-06	1.22E+00	9	296	348	1507	170	1	0
1.32E-06	1.32E+00	19	239	348	1488	153	0	0
1.42E-06	1.42E+00	7	216	308	1738	174	1	0
1.54E-06	1.54E+00	5	229	253	1760	198	0	0
1.66E-06	1.66E+00	2	195	228	1887	216	3	0
1.79E-06	1.79E+00	1	187	232	2098	235	0	0
1.94E-06	1.94E+00	2	185	248	2215	274	1	0
2.09E-06	2.09E+00	0	186	245	2326	309	2	0
2.26E-06	2.26E+00	1	169	213	2544	332	3	0
2.44E-06	2.44E+00	3	168	215	2837	400	2	0
2.64E-06	2.64E+00	0	153	192	2971	414	1	0
2.85E-06	2.85E+00	0	160	210	3069	480	3	1
3.08E-06	3.08E+00	0	165	221	3307	497	0	1
3.33E-06	3.33E+00	0	143	208	3615	564	3	1
3.59E-06	3.59E+00	0	170	239	3905	628	5	0
3.88E-06	3.88E+00	0	157	227	4145	705	6	0
4.19E-06	4.19E+00	0	155	236	4559	802	3	0
4.53E-06	4.53E+00	0	156	240	4743	854	6	1
4.89E-06	4.89E+00	0	157	266	5338	1000	6	2
5.28E-06	5.28E+00	0	158	236	5914	1198	6	0
5.71E-06	5.71E+00	0	150	286	9807	1771	8	2
6.16E-06	6.16E+00	0	166	318	9745	1838	11	0
6.66E-06	6.66E+00	0	144	303	8740	1892	14	1
7.19E-06	7.19E+00	0	150	281	7375	1839	21	2
7.77E-06	7.77E+00	0	175	259	6809	1930	21	6
8.39E-06	8.39E+00	0	145	232	6372	2156	20	4
9.06E-06	9.06E+00	0	125	219	6516	2387	36	7
9.79E-06	9.79E+00	0	125	214	6407	2607	47	6
1.06E-05	1.06E+01	0	162	225	6588	2940	54	9
1.14E-05	1.14E+01	0	136	206	7273	3436	72	12
1.23E-05	1.23E+01	0	169	215	7490	3792	82	30
1.33E-05	1.33E+01	0	163	218	7243	4106	100	18

1.44E-05	1.44E+01	0	195	213	7229	4340	128	34
1.55E-05	1.55E+01	0	176	181	7168	4681	194	42
1.68E-05	1.68E+01	0	234	195	7224	5128	200	60
1.81E-05	1.81E+01	0	250	215	7378	5663	262	87
1.96E-05	1.96E+01	0	328	211	7309	6154	372	96
2.12E-05	2.12E+01	0	354	203	7448	6592	475	114
2.29E-05	2.29E+01	0	391	206	7291	7148	555	184
2.47E-05	2.47E+01	0	495	227	7348	7702	647	232
2.67E-05	2.67E+01	0	507	223	7484	8136	820	325
2.88E-05	2.88E+01	0	494	234	7433	8963	1076	386
3.11E-05	3.11E+01	0	471	249	7394	9455	1208	516
3.36E-05	3.36E+01	0	450	249	7493	9973	1496	664
3.63E-05	3.63E+01	0	348	221	7430	10557	1810	837
3.92E-05	3.92E+01	0	305	224	7420	11068	2126	1055
4.24E-05	4.24E+01	0	273	211	7524	11760	2480	1253
4.58E-05	4.58E+01	0	245	228	7452	12314	2898	1671
4.94E-05	4.94E+01	0	231	199	7376	12790	3284	2019
5.34E-05	5.34E+01	0	204	182	7252	13680	3786	2367
5.77E-05	5.77E+01	0	195	207	7195	14088	4278	2767
6.23E-05	6.23E+01	0	201	168	7350	14667	4727	3244
6.73E-05	6.73E+01	0	167	166	7316	15622	5260	3824
7.27E-05	7.27E+01	0	142	191	7295	16033	5609	4346
7.85E-05	7.85E+01	0	153	164	7308	16837	6310	4946
8.48E-05	8.48E+01	0	134	189	7289	17530	6908	5308
9.16E-05	9.16E+01	0	134	171	7143	18311	7231	6017
9.90E-05	9.90E+01	0	131	162	7389	19208	7895	6600
1.07E-04	1.07E+02	0	104	167	7283	19622	8465	6986
1.15E-04	1.15E+02	0	112	163	7369	20137	8999	7704
1.25E-04	1.25E+02	0	121	175	7082	20467	9735	8195
1.35E-04	1.35E+02	0	105	150	7031	20360	10283	8640
1.46E-04	1.46E+02	0	105	173	7061	20595	11034	9382
1.57E-04	1.57E+02	0	82	172	7114	20468	12105	9936
1.70E-04	1.70E+02	0	90	177	6940	20280	13140	10636
1.83E-04	1.83E+02	0	96	198	6930	19909	14091	11272
1.98E-04	1.98E+02	0	92	191	6775	19130	15311	12000
2.14E-04	2.14E+02	0	87	205	6740	18817	16853	13113
2.31E-04	2.31E+02	0	102	185	6687	18398	17866	14413
2.50E-04	2.50E+02	0	90	230	6747	17989	19433	15591
2.70E-04	2.70E+02	0	71	196	6543	17399	20478	17012
2.91E-04	2.91E+02	0	94	171	6524	17095	21850	18656

3.15E-04	3.15E+02	0	78	201	6461	16548	23069	20000
3.40E-04	3.40E+02	0	88	179	6230	15938	24402	21629
3.67E-04	3.67E+02	0	75	165	6350	15652	26077	22603
3.97E-04	3.97E+02	0	61	166	6218	15102	27029	24385
4.29E-04	4.29E+02	0	67	149	6107	14526	28564	26118
4.63E-04	4.63E+02	0	74	160	6098	14268	29597	27658
5.00E-04	5.00E+02	0	71	180	5930	13676	29441	29184
5.40E-04	5.40E+02	0	69	169	5750	13379	29304	30643
5.83E-04	5.83E+02	0	54	176	5641	12961	28266	31368
6.30E-04	6.30E+02	0	60	184	5545	12451	26909	31276
6.81E-04	6.81E+02	0	53	171	5319	11970	25545	30648
7.35E-04	7.35E+02	0	52	167	5453	11689	24542	28992
7.94E-04	7.94E+02	0	68	217	5318	11233	23437	27639
8.58E-04	8.58E+02	0	42	207	5098	10763	22534	26536
9.27E-04	9.27E+02	0	60	171	5010	10254	21088	24911
1.00E-03	1.00E+03	0	50	189	4942	10141	20289	23969
1.08E-03	1.08E+03	0	60	200	4596	9495	19321	22733
1.17E-03	1.17E+03	0	80	208	4747	9229	18180	21896
1.26E-03	1.26E+03	0	70	205	4474	8724	17322	20615
1.36E-03	1.36E+03	0	58	190	4363	8497	16370	19464
1.47E-03	1.47E+03	0	40	185	4330	7985	15616	18398
1.59E-03	1.59E+03	0	54	183	4088	7744	14900	17705
1.72E-03	1.72E+03	0	55	189	4020	7355	13892	16482
1.86E-03	1.86E+03	0	49	187	3933	7099	13303	15563
2.00E-03	2.00E+03	0	57	159	3663	6681	12561	14614
2.16E-03	2.16E+03	1	38	168	3734	6407	12059	13934
2.34E-03	2.34E+03	0	27	140	3397	6044	11193	13175
2.53E-03	2.53E+03	0	23	193	3491	5814	10600	12275
2.73E-03	2.73E+03	0	18	194	3104	5504	9895	11293
2.95E-03	2.95E+03	0	22	188	3205	5315	9439	10800
3.18E-03	3.18E+03	0	22	178	3089	4887	8772	10064
3.44E-03	3.44E+03	0	16	202	2677	4760	8267	9447
3.71E-03	3.71E+03	0	22	208	2921	4476	7681	8887
4.01E-03	4.01E+03	0	25	205	2603	4212	7275	8106
4.33E-03	4.33E+03	0	21	169	2287	4149	6905	7714
4.68E-03	4.68E+03	0	23	110	2800	3607	6362	6945
5.06E-03	5.06E+03	0	22	137	2011	3778	5929	6554
5.46E-03	5.46E+03	0	22	130	2266	3221	5555	6165
5.90E-03	5.90E+03	0	20	170	2275	3371	5222	5618
6.37E-03	6.37E+03	0	18	202	1840	2785	4751	5126

6.88E-03	6.88E+03	0	12	212	1775	3111	4544	4755
7.44E-03	7.44E+03	0	13	224	2292	2431	4173	4487
8.03E-03	8.03E+03	0	15	163	1169	2631	3753	3914
8.68E-03	8.68E+03	0	14	178	1702	2379	3814	3851
9.37E-03	9.37E+03	0	15	186	1928	1986	3001	3425
1.01E-02	1.01E+04	0	11	186	1063	2399	3358	3134
1.09E-02	1.09E+04	0	4	177	1466	1681	2595	2860
1.18E-02	1.18E+04	0	4	146	1350	1931	2935	2698
1.28E-02	1.28E+04	0	4	99	1410	1962	2036	2399
1.38E-02	1.38E+04	0	4	90	1044	1309	2571	2233
1.49E-02	1.49E+04	0	4	128	680	1442	1791	1888
1.61E-02	1.61E+04	0	5	123	1691	1740	1855	2205
1.74E-02	1.74E+04	0	4	160	724	1102	2060	1427
1.88E-02	1.88E+04	0	4	70	710	971	1250	1446
2.03E-02	2.03E+04	0	8	97	1051	1764	1666	1685
2.19E-02	2.19E+04	0	5	133	736	685	1315	864
2.36E-02	2.36E+04	0	12	165	881	757	887	1415
2.55E-02	2.55E+04	0	9	227	733	1162	1344	1160
2.76E-02	2.76E+04	0	53	271	319	994	1170	913
2.98E-02	2.98E+04	0	43	139	694	777	827	686
3.22E-02	3.22E+04	0	21	183	813	437	728	719
3.48E-02	3.48E+04	0	21	122	881	692	752	1319
3.76E-02	3.76E+04	0	21	104	70	1140	1171	67
4.06E-02	4.06E+04	0	19	79	245	496	75	737
4.38E-02	4.38E+04	0	19	4	564	120	738	455
4.73E-02	4.73E+04	0	24	2	512	688	479	956
5.11E-02	5.11E+04	0	22	6	737	442	902	140
5.52E-02	5.52E+04	0	28	4	158	733	138	308
5.97E-02	5.97E+04	0	8	7	92	273	280	458
6.44E-02	6.44E+04	0	4	9	647	95	471	24
6.96E-02	6.96E+04	0	4	250	27	645	39	754
7.52E-02	7.52E+04	0	8	424	68	31	731	371
8.12E-02	8.12E+04	0	4	90	692	125	368	185
8.77E-02	8.77E+04	0	10	8	218	655	152	217
9.48E-02	9.48E+04	0	6	37	197	355	266	0
1.02E-01	1.02E+05	0	4	340	322	329	0	0
1.11E-01	1.11E+05	0	8	3	8	27	9	24
1.19E-01	1.19E+05	0	5	0	12	8	19	729
1.29E-01	1.29E+05	0	7	0	10	12	516	43
1.39E-01	1.39E+05	0	8	4	36	38	253	39

1.51E-01	1.51E+05	0	7	0	520	543	23	349
1.63E-01	1.63E+05	0	8	0	210	191	364	0
1.76E-01	1.76E+05	0	8	4	31	44	0	0
1.90E-01	1.90E+05	0	110	2	341	332	0	0
2.05E-01	2.05E+05	0	72	2	0	0	0	0
2.21E-01	2.21E+05	0	55	4	4	0	0	0
2.39E-01	2.39E+05	0	20	17	0	4	4	10
2.58E-01	2.58E+05	0	6	312	4	0	6	386
2.79E-01	2.79E+05	0	6	55	4	8	386	0
3.01E-01	3.01E+05	0	8	0	4	7	0	4
3.25E-01	3.25E+05	0	8	0	22	290	4	0
3.52E-01	3.52E+05	0	8	0	362	91	0	0
3.80E-01	3.80E+05	0	10	4	0	0	0	0
4.10E-01	4.10E+05	0	10	0	0	0	0	0
4.43E-01	4.43E+05	0	9	0	0	0	0	368
4.79E-01	4.79E+05	0	13	4	4	0	16	28
5.17E-01	5.17E+05	0	14	12	0	4	380	0
5.58E-01	5.58E+05	0	16	203	4	17	0	0
6.03E-01	6.03E+05	0	25	72	37	375	0	0
6.52E-01	6.52E+05	0	11	42	351	0	0	0
7.04E-01	7.04E+05	0	0	32	0	0	0	0
7.60E-01	7.60E+05	0	0	27	0	0	0	0
8.21E-01	8.21E+05	0	0	0	0	0	0	0
8.87E-01	8.87E+05	0	0	0	0	0	0	0
9.58E-01	9.58E+05	0	0	0	0	0	0	0
1.04E+00	1.04E+06	0	0	0	0	0	0	0
1.12E+00	1.12E+06	0	0	0	0	0	0	0
1.21E+00	1.21E+06	0	0	0	0	0	0	0
1.30E+00	1.30E+06	0	0	0	0	0	0	0
1.41E+00	1.41E+06	0	0	0	0	0	0	0
1.52E+00	1.52E+06	0	0	0	0	0	0	0
1.64E+00	1.64E+06	1	0	0	0	0	0	0
1.78E+00	1.78E+06	0	0	0	0	0	0	0
1.92E+00	1.92E+06	0	0	0	0	0	0	0
2.07E+00	2.07E+06	11	0	0	0	0	0	0
2.24E+00	2.24E+06	17	0	0	0	0	0	0
2.42E+00	2.42E+06	0	4	0	0	0	0	0
2.61E+00	2.61E+06	0	3	0	0	0	0	0
2.82E+00	2.82E+06	0	4	0	0	0	0	0
3.05E+00	3.05E+06	0	4	0	0	0	0	0

3.29E+00	3.29E+06	0	4	0	0	0	0	0
3.56E+00	3.56E+06	0	4	0	0	0	0	0
3.84E+00	3.84E+06	0	5	0	0	0	0	1
4.15E+00	4.15E+06	0	6	0	0	0	1	99
4.48E+00	4.48E+06	0	9	0	0	0	99	0
4.84E+00	4.84E+06	0	1	0	1	1	0	0
5.23E+00	5.23E+06	0	1	1	0	99	0	0
5.65E+00	5.65E+06	0	0	0	99	0	0	0
6.10E+00	6.10E+06	0	3	1	0	0	0	0
6.59E+00	6.59E+06	0	42	49	0	0	0	0
7.12E+00	7.12E+06	0	10	49	0	0	0	0
# Targets Hit --->		2609	37607	53097	670527	995517	999997	1000000

Table B3. Dose (Gy) deposited in voxels inside the mesh cube by ions of equal velocity (600 MeV n^{-1}). FLUKA data is scaled as GeV-cm^{-3} and described in the 'Bin' column. Un-hit voxels appear in the first row for each ion. The number of hit voxels is summed and listed at the bottom of the table.

Dose (Gy)	Bin	Be-8 Voxels hit	C-12 Voxels hit	O-16 Voxels hit	Mg-24 Voxels hit	Si-28 Voxels hit	Ca-40 Voxels hit	Ti-48 Voxels hit
1.60E-12	1.00E-06	59278	16314	5231	469	137	1	0
1.72E-12	1.07E-06	2	2	0	0	0	0	0
1.84E-12	1.15E-06	0	0	0	0	0	0	0
1.97E-12	1.23E-06	0	0	0	0	0	0	0
2.11E-12	1.32E-06	0	1	0	0	0	0	0
2.26E-12	1.41E-06	1	0	0	0	0	0	0
2.42E-12	1.51E-06	0	0	0	0	0	0	0
2.60E-12	1.62E-06	0	2	0	0	0	0	0
2.78E-12	1.74E-06	0	1	0	0	0	0	0
2.98E-12	1.86E-06	0	1	0	0	0	0	0
3.20E-12	2.00E-06	1	0	0	0	0	0	0
3.43E-12	2.14E-06	1	0	0	0	0	0	0
3.67E-12	2.29E-06	2	0	0	0	0	0	0
3.93E-12	2.45E-06	0	0	0	0	0	0	0
4.21E-12	2.63E-06	1	0	0	0	0	0	0
4.52E-12	2.82E-06	1	0	1	0	0	0	0
4.84E-12	3.02E-06	0	0	0	0	0	0	0
5.18E-12	3.24E-06	1	0	2	0	0	0	0
5.56E-12	3.47E-06	1	1	0	0	0	0	0
5.95E-12	3.72E-06	4	2	0	0	0	0	0
6.38E-12	3.98E-06	1	0	0	0	0	0	0
6.83E-12	4.27E-06	2	0	1	0	0	0	0
7.32E-12	4.57E-06	1	0	1	0	0	0	0
7.85E-12	4.90E-06	6	1	0	0	0	0	0
8.41E-12	5.25E-06	3	2	0	0	0	0	0
9.01E-12	5.62E-06	0	0	0	0	0	0	0
9.65E-12	6.03E-06	2	0	0	0	0	0	0
1.03E-11	6.46E-06	0	0	0	0	0	0	0
1.11E-11	6.92E-06	5	2	1	0	0	0	0
1.19E-11	7.41E-06	6	0	0	0	0	0	0
1.27E-11	7.94E-06	3	0	1	0	0	0	0
1.36E-11	8.51E-06	2	0	1	0	0	0	0
1.46E-11	9.12E-06	4	0	0	0	0	0	0
1.57E-11	9.77E-06	2	1	0	0	0	0	0

1.68E-11	1.05E-05	4	1	0	0	0	0	0
1.80E-11	1.12E-05	6	3	0	0	0	0	0
1.93E-11	1.20E-05	7	0	0	0	0	0	0
2.06E-11	1.29E-05	3	2	0	0	0	0	0
2.21E-11	1.38E-05	7	2	0	1	0	0	0
2.37E-11	1.48E-05	8	3	2	0	0	0	0
2.54E-11	1.58E-05	10	2	1	0	0	0	0
2.72E-11	1.70E-05	11	6	1	0	0	0	0
2.92E-11	1.82E-05	8	1	2	0	0	0	0
3.12E-11	1.95E-05	11	4	1	0	1	0	0
3.35E-11	2.09E-05	7	2	1	0	0	0	0
3.59E-11	2.24E-05	9	1	0	0	0	0	0
3.84E-11	2.40E-05	5	2	1	0	0	0	0
4.12E-11	2.57E-05	15	5	4	0	0	0	0
4.41E-11	2.75E-05	8	7	4	0	0	0	0
4.73E-11	2.95E-05	7	2	2	1	0	0	0
5.07E-11	3.16E-05	10	4	2	0	0	0	0
5.43E-11	3.39E-05	14	10	2	0	0	0	0
5.82E-11	3.63E-05	14	5	1	0	0	0	0
6.23E-11	3.89E-05	16	3	2	0	0	0	0
6.68E-11	4.17E-05	22	2	3	0	0	0	0
7.16E-11	4.47E-05	18	1	2	0	0	0	0
7.67E-11	4.79E-05	12	11	4	0	0	0	0
8.22E-11	5.13E-05	21	9	1	0	1	0	0
8.80E-11	5.50E-05	22	7	3	0	0	0	0
9.43E-11	5.89E-05	25	4	6	0	0	0	0
1.01E-10	6.31E-05	36	13	2	0	0	0	0
1.08E-10	6.76E-05	23	13	3	0	0	0	0
1.16E-10	7.24E-05	25	11	2	2	0	0	0
1.24E-10	7.76E-05	24	8	2	0	0	0	0
1.33E-10	8.32E-05	30	7	8	0	0	0	0
1.43E-10	8.91E-05	29	7	6	1	0	0	0
1.53E-10	9.55E-05	42	15	3	0	0	0	0
1.64E-10	1.02E-04	36	18	10	0	0	0	0
1.76E-10	1.10E-04	33	21	6	0	0	0	0
1.88E-10	1.17E-04	55	7	9	0	0	0	0
2.02E-10	1.26E-04	54	21	6	0	0	0	0
2.16E-10	1.35E-04	55	24	7	1	0	0	0
2.32E-10	1.45E-04	51	23	4	2	2	0	0
2.48E-10	1.55E-04	60	22	7	1	0	0	0

2.66E-10	1.66E-04	74	25	5	2	0	0	0
2.85E-10	1.78E-04	68	11	7	0	0	0	0
3.05E-10	1.91E-04	83	30	6	1	1	0	0
3.27E-10	2.04E-04	70	28	14	1	0	0	0
3.51E-10	2.19E-04	89	30	11	3	2	0	0
3.76E-10	2.34E-04	90	25	12	2	0	0	0
4.02E-10	2.51E-04	94	35	9	3	2	0	0
4.31E-10	2.69E-04	100	30	16	3	1	0	0
4.62E-10	2.88E-04	128	46	11	1	1	0	0
4.95E-10	3.09E-04	116	38	17	3	1	0	0
5.31E-10	3.31E-04	139	46	23	0	2	0	0
5.68E-10	3.55E-04	136	51	29	2	1	0	0
6.09E-10	3.80E-04	129	48	14	2	0	0	0
6.53E-10	4.07E-04	135	60	26	3	1	0	0
6.99E-10	4.37E-04	163	74	22	3	2	0	0
7.49E-10	4.68E-04	196	72	33	3	1	0	0
8.03E-10	5.01E-04	181	77	30	3	3	0	0
8.60E-10	5.37E-04	188	81	48	5	3	0	0
9.22E-10	5.75E-04	251	83	35	3	0	0	0
9.88E-10	6.17E-04	252	93	36	4	0	0	0
1.06E-09	6.61E-04	283	110	32	5	1	0	0
1.13E-09	7.08E-04	241	112	46	8	5	0	0
1.22E-09	7.59E-04	312	118	53	6	1	0	0
1.30E-09	8.13E-04	299	131	57	6	2	0	0
1.40E-09	8.71E-04	352	126	52	7	0	0	0
1.50E-09	9.33E-04	354	133	50	16	1	0	0
1.60E-09	1.00E-03	369	136	56	8	4	0	0
1.72E-09	1.07E-03	438	172	70	10	1	0	0
1.84E-09	1.15E-03	443	169	67	6	2	0	0
1.97E-09	1.23E-03	566	185	68	5	6	0	0
2.11E-09	1.32E-03	500	186	62	8	5	1	0
2.26E-09	1.41E-03	569	221	94	12	5	0	0
2.42E-09	1.51E-03	639	217	102	17	8	0	0
2.60E-09	1.62E-03	640	268	92	17	7	0	0
2.78E-09	1.74E-03	701	272	98	14	7	0	0
2.98E-09	1.86E-03	713	273	119	14	7	1	0
3.20E-09	2.00E-03	780	314	108	14	9	0	0
3.43E-09	2.14E-03	851	309	135	34	5	0	0
3.67E-09	2.29E-03	943	358	121	21	12	1	0
3.93E-09	2.45E-03	995	349	178	24	8	0	0

4.21E-09	2.63E-03	1073	370	152	22	14	0	0
4.52E-09	2.82E-03	1126	458	192	27	10	0	0
4.84E-09	3.02E-03	1213	505	216	40	16	0	0
5.18E-09	3.24E-03	1313	502	189	39	16	1	0
5.56E-09	3.47E-03	1421	566	234	35	7	0	0
5.95E-09	3.72E-03	1562	578	239	56	9	1	1
6.38E-09	3.98E-03	1695	645	271	50	19	1	0
6.83E-09	4.27E-03	1710	685	282	50	18	3	0
7.32E-09	4.57E-03	1946	769	296	54	22	2	0
7.85E-09	4.90E-03	2100	822	356	68	23	1	0
8.41E-09	5.25E-03	2210	825	392	75	16	4	1
9.01E-09	5.62E-03	2386	893	364	68	25	0	1
9.65E-09	6.03E-03	2644	985	446	85	26	1	0
1.03E-08	6.46E-03	2820	1067	470	90	30	1	0
1.11E-08	6.92E-03	3219	1196	541	94	43	3	1
1.19E-08	7.41E-03	3516	1303	568	99	43	3	3
1.27E-08	7.94E-03	3799	1513	661	124	50	2	1
1.36E-08	8.51E-03	4268	1655	711	137	48	3	1
1.46E-08	9.12E-03	4817	1756	799	155	53	1	0
1.57E-08	9.77E-03	5179	2072	865	140	70	5	1
1.68E-08	1.05E-02	5416	2234	968	175	76	0	0
1.80E-08	1.12E-02	5965	2397	1053	197	104	2	1
1.93E-08	1.20E-02	6061	2574	1140	218	94	2	3
2.06E-08	1.29E-02	6449	2785	1278	231	113	7	1
2.21E-08	1.38E-02	6856	2910	1326	262	120	7	0
2.37E-08	1.48E-02	7368	3111	1461	298	143	10	1
2.54E-08	1.58E-02	7705	3267	1533	316	169	13	4
2.72E-08	1.70E-02	8174	3595	1586	363	191	7	7
2.92E-08	1.82E-02	8526	3728	1796	417	189	9	9
3.12E-08	1.95E-02	9097	4183	1928	482	207	16	7
3.35E-08	2.09E-02	9495	4498	2113	473	255	17	11
3.59E-08	2.24E-02	10074	4784	2278	569	304	22	6
3.84E-08	2.40E-02	10605	5175	2528	603	305	23	10
4.12E-08	2.57E-02	11129	5421	2710	656	367	28	12
4.41E-08	2.75E-02	11912	5950	2854	782	403	42	17
4.73E-08	2.95E-02	12432	6221	3123	848	456	44	19
5.07E-08	3.16E-02	12980	6844	3364	952	492	53	22
5.43E-08	3.39E-02	13520	7330	3777	1076	557	57	33
5.82E-08	3.63E-02	13993	7799	3928	1201	635	62	33
6.23E-08	3.89E-02	14767	8423	4398	1294	732	87	34

6.68E-08	4.17E-02	15218	8943	4615	1406	770	110	46
7.16E-08	4.47E-02	15783	9471	5068	1582	919	100	52
7.67E-08	4.79E-02	16309	10084	5519	1755	970	134	64
8.22E-08	5.13E-02	16598	10891	5859	1974	1167	177	98
8.80E-08	5.50E-02	17185	11666	6271	2138	1296	185	101
9.43E-08	5.89E-02	17265	12277	6966	2318	1344	251	132
1.01E-07	6.31E-02	18019	13205	7451	2511	1580	284	140
1.08E-07	6.76E-02	17941	13916	7929	2792	1732	313	179
1.16E-07	7.24E-02	18387	14655	8586	3008	1834	365	199
1.24E-07	7.76E-02	18672	15475	9260	3305	2069	465	260
1.33E-07	8.32E-02	18766	16014	9908	3635	2398	552	284
1.43E-07	8.91E-02	18729	17039	10734	3993	2607	618	345
1.53E-07	9.55E-02	18785	17647	11493	4352	2733	736	386
1.64E-07	1.02E-01	18598	18446	12261	4739	3052	753	508
1.76E-07	1.10E-01	18496	19079	13297	5080	3369	961	604
1.88E-07	1.17E-01	18533	19874	13983	5651	3804	1096	694
2.02E-07	1.26E-01	18320	20359	15332	6228	4081	1229	822
2.16E-07	1.35E-01	17955	20744	16057	6671	4479	1405	934
2.32E-07	1.45E-01	17769	21137	17269	7288	4910	1643	1120
2.48E-07	1.55E-01	17198	21705	18312	7927	5397	1925	1281
2.66E-07	1.66E-01	16757	22059	18941	8724	5847	2059	1451
2.85E-07	1.78E-01	15894	21919	20201	9463	6485	2420	1681
3.05E-07	1.91E-01	15642	22028	21289	10264	7028	2593	1800
3.27E-07	2.04E-01	15088	21839	21515	11280	7788	3057	2219
3.51E-07	2.19E-01	14167	21289	22297	12062	8338	3194	2352
3.76E-07	2.34E-01	13842	21183	23108	13092	9070	3599	2655
4.02E-07	2.51E-01	13102	20496	23060	14043	10027	4010	3087
4.31E-07	2.69E-01	12452	19596	23357	15164	10823	4432	3216
4.62E-07	2.88E-01	11770	19156	23225	16423	11755	4838	3704
4.95E-07	3.09E-01	11228	18375	23177	17183	12783	5268	4121
5.31E-07	3.31E-01	10604	17679	22984	18731	13814	5920	4635
5.68E-07	3.55E-01	10315	16978	22912	20002	14822	6338	5066
6.09E-07	3.80E-01	9492	16224	22194	20882	16168	6788	5412
6.53E-07	4.07E-01	8973	15782	21484	22171	17144	7363	5945
6.99E-07	4.37E-01	8657	14838	20746	22760	18391	8213	6428
7.49E-07	4.68E-01	8207	14195	19998	23938	19434	9068	7011
8.03E-07	5.01E-01	7915	13393	19184	24639	20502	10064	7836
8.60E-07	5.37E-01	7537	12873	18403	25141	21681	10877	8279
9.22E-07	5.75E-01	7078	12487	17701	25388	22981	11679	8991
9.88E-07	6.17E-01	6688	11749	17175	25352	24332	12857	9943

1.06E-06	6.61E-01	6287	11201	16437	24694	24840	13759	11050
1.13E-06	7.08E-01	5989	10536	15403	24528	25472	14929	12061
1.22E-06	7.59E-01	5666	10087	14809	23754	25766	15957	13112
1.30E-06	8.13E-01	5281	9582	14253	23049	25675	17173	14158
1.40E-06	8.71E-01	5043	9042	13376	22126	25672	18614	15391
1.50E-06	9.33E-01	4746	8699	12751	21279	25122	19762	16375
1.60E-06	1.00E+00	4405	8123	12323	20582	24157	20878	17433
1.72E-06	1.07E+00	4287	7742	11727	19681	23731	21754	18799
1.84E-06	1.15E+00	3906	7193	10950	18944	22431	22910	20066
1.97E-06	1.23E+00	3590	7044	10748	17987	21726	24384	21163
2.11E-06	1.32E+00	3371	6509	10042	17190	21258	25432	22148
2.26E-06	1.41E+00	3243	6212	9656	16443	19962	26012	23299
2.42E-06	1.51E+00	3037	5894	8944	15931	19009	26236	24685
2.60E-06	1.62E+00	2790	5521	8643	15123	18376	26436	25594
2.78E-06	1.74E+00	2716	5316	8211	14251	17288	26233	26556
2.98E-06	1.86E+00	2497	4812	7816	13640	16611	25268	26802
3.20E-06	2.00E+00	2389	4605	7276	13094	15823	24549	26587
3.43E-06	2.14E+00	2252	4425	6811	12416	15393	23372	26174
3.67E-06	2.29E+00	2090	4168	6626	11771	14485	23043	25227
3.93E-06	2.45E+00	1935	3845	6215	11308	14027	21854	24327
4.21E-06	2.63E+00	1865	3619	5936	10913	13251	20738	23466
4.52E-06	2.82E+00	1702	3449	5460	10092	12665	20041	22493
4.84E-06	3.02E+00	1592	3264	5200	9811	12021	19505	21348
5.18E-06	3.24E+00	1525	3031	4867	9230	11526	18476	20624
5.56E-06	3.47E+00	1331	2774	4465	8880	11013	17514	19832
5.95E-06	3.72E+00	1329	2778	4364	8288	10462	17003	18930
6.38E-06	3.98E+00	1217	2564	4022	8085	9905	16311	18336
6.83E-06	4.27E+00	1194	2308	3898	7490	9502	15425	17451
7.32E-06	4.57E+00	1139	2238	3712	7095	8895	14635	16814
7.85E-06	4.90E+00	1024	2143	3524	6711	8575	13917	16046
8.41E-06	5.25E+00	985	2012	3289	6368	8081	13527	15091
9.01E-06	5.62E+00	966	1938	3136	5915	7807	12820	14451
9.65E-06	6.03E+00	887	1764	2852	5740	7208	12269	13942
1.03E-05	6.46E+00	782	1574	2686	5369	6707	11624	13229
1.11E-05	6.92E+00	666	1616	2570	5159	6566	11000	12633
1.19E-05	7.41E+00	638	1439	2394	4814	6213	10519	12103
1.27E-05	7.94E+00	618	1342	2293	4461	5750	9961	11419
1.36E-05	8.51E+00	723	1180	2103	4292	5452	9287	10943
1.46E-05	9.12E+00	568	1200	1903	4021	5134	9028	10339
1.57E-05	9.77E+00	401	1178	1801	3851	4875	8414	9970

1.68E-05	1.05E+01	366	930	1788	3550	4572	8049	9237
1.80E-05	1.12E+01	438	830	1605	3395	4362	7839	8800
1.93E-05	1.20E+01	454	900	1516	3158	4159	7348	8640
2.06E-05	1.29E+01	514	930	1462	2997	3824	6924	7958
2.21E-05	1.38E+01	389	777	1415	2746	3650	6534	7688
2.37E-05	1.48E+01	249	717	1130	2594	3391	6269	7105
2.54E-05	1.58E+01	284	552	1082	2530	3248	5896	6740
2.72E-05	1.70E+01	314	555	1247	2306	2972	5610	6460
2.92E-05	1.82E+01	216	661	1162	2100	2863	5165	6143
3.12E-05	1.95E+01	114	827	714	2189	2713	4925	5841
3.35E-05	2.09E+01	280	465	813	1845	2458	4786	5345
3.59E-05	2.24E+01	365	229	1000	1666	2437	4390	5237
3.84E-05	2.40E+01	269	371	864	1935	2140	4179	4869
4.12E-05	2.57E+01	235	409	754	1402	2200	3870	4619
4.41E-05	2.75E+01	242	511	522	1385	2082	3755	4387
4.73E-05	2.95E+01	110	589	502	1476	1548	3385	4167
5.07E-05	3.16E+01	39	296	590	1467	1907	3367	3747
5.43E-05	3.39E+01	28	131	911	1011	1648	3030	3681
5.82E-05	3.63E+01	11	309	597	984	1368	2926	3336
6.23E-05	3.89E+01	22	339	156	1422	1383	2768	3368
6.68E-05	4.17E+01	179	98	285	887	1590	2395	2905
7.16E-05	4.47E+01	374	78	428	682	1126	2595	2961
7.67E-05	4.79E+01	158	395	468	912	824	2095	2593
8.22E-05	5.13E+01	67	361	664	923	1397	2077	2470
8.80E-05	5.50E+01	198	280	386	873	1177	2281	2542
9.43E-05	5.89E+01	131	216	78	694	678	1464	2045
1.01E-04	6.31E+01	30	197	165	411	717	1937	2081
1.08E-04	6.76E+01	21	47	496	581	1036	1849	2263
1.16E-04	7.24E+01	3	10	127	494	856	1192	1377
1.24E-04	7.76E+01	3	4	34	1190	779	1424	1985
1.33E-04	8.32E+01	1	11	259	287	545	1625	1674
1.43E-04	8.91E+01	0	15	470	80	446	1257	1355
1.53E-04	9.55E+01	0	324	320	479	466	872	1278
1.64E-04	1.02E+02	6	390	161	326	1007	1114	1731
1.76E-04	1.10E+02	47	50	270	515	754	1553	1072
1.88E-04	1.17E+02	256	76	48	682	54	587	765
2.02E-04	1.26E+02	74	285	6	256	165	612	1416
2.16E-04	1.35E+02	11	24	3	31	599	1162	1310
2.32E-04	1.45E+02	1	3	8	311	333	818	643
2.48E-04	1.55E+02	1	5	8	439	752	787	585

2.66E-04	1.66E+02	0	0	119	24	424	679	1135
2.85E-04	1.78E+02	3	0	615	27	39	309	898
3.05E-04	1.91E+02	1	0	42	509	60	633	769
3.27E-04	2.04E+02	0	0	12	288	666	680	542
3.51E-04	2.19E+02	2	1	321	326	53	1137	367
3.76E-04	2.34E+02	65	7	54	146	26	47	512
4.02E-04	2.51E+02	289	143	1	251	104	65	903
4.31E-04	2.69E+02	37	234	3	1	667	690	892
4.62E-04	2.88E+02	2	11	1	7	295	175	38
4.95E-04	3.09E+02	1	0	0	1	97	690	93
5.31E-04	3.31E+02	0	0	0	9	362	617	685
5.68E-04	3.55E+02	0	0	0	10	9	83	291
6.09E-04	3.80E+02	0	4	0	372	1	32	801
6.53E-04	4.07E+02	0	0	6	400	7	605	419
6.99E-04	4.37E+02	0	0	19	3	7	143	23
7.49E-04	4.68E+02	0	0	366	33	9	23	41
8.03E-04	5.01E+02	0	5	5	353	30	31	713
8.60E-04	5.37E+02	0	264	0	0	735	731	19
9.22E-04	5.75E+02	0	127	0	0	11	102	27
9.88E-04	6.17E+02	0	0	0	4	8	306	55
1.06E-03	6.61E+02	0	0	3	0	352	296	724
1.13E-03	7.08E+02	0	0	1	0	28	75	283
1.22E-03	7.59E+02	0	0	0	0	0	0	108
1.30E-03	8.13E+02	0	0	0	0	3	8	364
1.40E-03	8.71E+02	0	0	1	0	1	4	3
1.50E-03	9.33E+02	0	0	54	8	0	7	0
1.60E-03	1.00E+03	0	0	341	132	0	14	8
1.72E-03	1.07E+03	0	0	0	256	0	740	8
1.84E-03	1.15E+03	0	0	0	0	0	27	8
1.97E-03	1.23E+03	0	0	0	0	8	4	22
2.11E-03	1.32E+03	0	0	0	0	4	161	750
2.26E-03	1.41E+03	0	0	0	0	384	223	4
2.42E-03	1.51E+03	0	0	0	4	0	0	5
2.60E-03	1.62E+03	0	0	0	0	0	2	376
2.78E-03	1.74E+03	0	0	0	0	0	2	7
2.98E-03	1.86E+03	0	0	0	0	0	0	0
3.20E-03	2.00E+03	0	0	0	4	0	0	4
3.43E-03	2.14E+03	0	0	0	324	4	0	0
3.67E-03	2.29E+03	0	0	0	68	0	0	0
3.93E-03	2.45E+03	0	0	0	0	0	2	0

4.21E-03	2.63E+03	0	0	0	0	0	6	0
4.52E-03	2.82E+03	0	0	0	0	12	383	0
4.84E-03	3.02E+03	0	0	0	0	384	5	7
5.18E-03	3.24E+03	0	0	0	0	0	0	5
5.56E-03	3.47E+03	0	0	0	0	0	0	384
5.95E-03	3.72E+03	0	0	0	0	0	0	0
6.38E-03	3.98E+03	0	0	0	0	0	0	0
6.83E-03	4.27E+03	0	0	0	0	0	4	0
7.32E-03	4.57E+03	0	0	0	0	0	0	0
7.85E-03	4.90E+03	0	0	0	0	0	0	0
8.41E-03	5.25E+03	0	0	0	0	0	0	4
9.01E-03	5.62E+03	0	0	0	0	0	8	0
9.65E-03	6.03E+03	0	0	0	0	0	386	0
1.03E-02	6.46E+03	0	0	0	0	0	2	0
1.11E-02	6.92E+03	0	0	0	0	0	0	8
1.19E-02	7.41E+03	0	0	0	0	0	0	388
1.27E-02	7.94E+03	0	0	0	0	0	0	0
1.36E-02	8.51E+03	0	0	0	0	0	0	0
1.46E-02	9.12E+03	0	0	0	0	0	0	0
1.57E-02	9.77E+03	0	0	0	0	0	0	0
1.68E-02	1.05E+04	0	0	0	0	0	0	0
1.80E-02	1.12E+04	0	0	0	0	0	0	0
1.93E-02	1.20E+04	0	0	0	0	0	0	0
2.06E-02	1.29E+04	0	0	0	0	0	0	0
2.21E-02	1.38E+04	0	0	0	0	0	0	0
2.37E-02	1.48E+04	0	0	0	0	0	0	0
2.54E-02	1.58E+04	0	0	0	0	0	0	0
2.72E-02	1.70E+04	0	0	0	0	0	0	0
2.92E-02	1.82E+04	0	0	0	0	0	0	0
3.12E-02	1.95E+04	0	0	0	0	0	0	0
3.35E-02	2.09E+04	0	0	0	0	0	0	0
3.59E-02	2.24E+04	0	0	0	0	0	0	0
3.84E-02	2.40E+04	0	0	0	0	0	0	0
4.12E-02	2.57E+04	0	0	0	0	0	0	0
4.41E-02	2.75E+04	0	0	0	0	0	0	0
4.73E-02	2.95E+04	0	0	0	0	0	0	0
5.07E-02	3.16E+04	0	0	0	0	0	0	0
5.43E-02	3.39E+04	100	0	0	0	0	0	0
5.82E-02	3.63E+04	0	0	0	0	0	0	0
6.23E-02	3.89E+04	0	0	0	0	0	0	0

6.68E-02	4.17E+04	0	0	0	0	0	0	0
7.16E-02	4.47E+04	0	0	0	0	0	0	0
7.67E-02	4.79E+04	0	0	0	0	0	0	0
8.22E-02	5.13E+04	0	0	0	0	0	0	0
8.80E-02	5.50E+04	0	0	0	0	0	0	0
9.43E-02	5.89E+04	0	0	0	0	0	0	0
1.01E-01	6.31E+04	0	0	0	0	0	0	0
1.08E-01	6.76E+04	0	0	0	0	0	0	0
1.16E-01	7.24E+04	0	0	0	0	0	0	0
1.24E-01	7.76E+04	0	100	0	0	0	0	0
1.33E-01	8.32E+04	0	0	0	0	0	0	0
1.43E-01	8.91E+04	0	0	0	0	0	0	0
1.53E-01	9.55E+04	0	0	0	0	0	0	0
1.64E-01	1.02E+05	0	0	0	0	0	0	0
1.76E-01	1.10E+05	0	0	0	0	0	0	0
1.88E-01	1.17E+05	0	0	0	0	0	0	0
2.02E-01	1.26E+05	0	0	0	0	0	0	0
2.16E-01	1.35E+05	0	0	100	0	0	0	0
2.32E-01	1.45E+05	0	0	0	0	0	0	0
2.48E-01	1.55E+05	0	0	0	0	0	0	0
2.66E-01	1.66E+05	0	0	0	0	0	0	0
2.85E-01	1.78E+05	0	0	0	0	0	0	0
3.05E-01	1.91E+05	0	0	0	0	0	0	0
3.27E-01	2.04E+05	0	0	0	0	0	0	0
3.51E-01	2.19E+05	0	0	0	0	0	0	0
3.76E-01	2.34E+05	0	0	0	0	0	0	0
4.02E-01	2.51E+05	0	0	0	0	0	0	0
4.31E-01	2.69E+05	0	0	0	0	0	0	0
4.62E-01	2.88E+05	0	0	0	0	0	0	0
4.95E-01	3.09E+05	0	0	0	100	0	0	0
5.31E-01	3.31E+05	0	0	0	0	0	0	0
5.68E-01	3.55E+05	0	0	0	0	0	0	0
6.09E-01	3.80E+05	0	0	0	0	0	0	0
6.53E-01	4.07E+05	0	0	0	0	100	0	0
6.99E-01	4.37E+05	0	0	0	0	0	0	0
7.49E-01	4.68E+05	0	0	0	0	0	0	0
8.03E-01	5.01E+05	0	0	0	0	0	0	0
8.60E-01	5.37E+05	0	0	0	0	0	0	0
9.22E-01	5.75E+05	0	0	0	0	0	0	0
9.88E-01	6.17E+05	0	0	0	0	0	0	0

1.06E+00	6.61E+05	0	0	0	0	0	0	0
1.13E+00	7.08E+05	0	0	0	0	0	0	0
1.22E+00	7.59E+05	0	0	0	0	0	0	0
1.30E+00	8.13E+05	0	0	0	0	0	0	0
1.40E+00	8.71E+05	0	0	0	0	0	100	0
1.50E+00	9.33E+05	0	0	0	0	0	0	0
1.60E+00	1.00E+06	0	0	0	0	0	0	3
1.72E+00	1.07E+06	0	0	0	0	0	0	97
1.84E+00	1.15E+06	0	0	0	0	0	0	0
# Targets Hit ---->		940722	983686	994769	999531	999863	999999	1000000

Table B4. Electron fluence (electrons / 1000 nm^2) in voxels inside the mesh cube geometry by ions of equal velocity (600 MeV n^{-1}). FLUKA data is scaled as electrons-cm^{-2} and described in the 'Bin' column. Un-hit voxels appear in the first row for each ion. The number of hit voxels is summed and listed at the bottom of the table.

Electron Fluence	Bin	Be-8 Voxels hit	C-12 Voxels hit	O-16 Voxels hit	Mg-24 Voxels hit	Si-28 Voxels hit	Ca-40 Voxels hit	Ti-48 Voxels hit
1.00E-10	1.00E-04	60402	16515	5309	476	140	2	0
1.07E-10	1.07E-04	0	0	0	0	0	0	0
1.15E-10	1.15E-04	0	0	0	0	0	0	0
1.23E-10	1.23E-04	0	0	0	0	0	0	0
1.32E-10	1.32E-04	0	0	0	0	0	0	0
1.41E-10	1.41E-04	0	0	0	0	0	0	0
1.51E-10	1.51E-04	0	1	0	0	0	0	0
1.62E-10	1.62E-04	0	0	0	0	0	0	0
1.74E-10	1.74E-04	1	0	0	0	0	0	0
1.86E-10	1.86E-04	1	0	0	0	0	0	0
2.00E-10	2.00E-04	0	0	0	0	0	0	0
2.14E-10	2.14E-04	0	0	0	0	0	0	0
2.29E-10	2.29E-04	0	0	0	0	0	0	0
2.45E-10	2.45E-04	0	0	0	0	1	0	0
2.63E-10	2.63E-04	0	0	0	0	0	0	0
2.82E-10	2.82E-04	0	0	0	0	0	0	0
3.02E-10	3.02E-04	0	0	0	0	0	0	0
3.24E-10	3.24E-04	0	0	0	0	0	0	0
3.47E-10	3.47E-04	0	0	1	0	0	0	0
3.72E-10	3.72E-04	0	0	0	0	0	0	0
3.98E-10	3.98E-04	0	0	0	0	0	0	0
4.27E-10	4.27E-04	0	0	0	0	0	0	0
4.57E-10	4.57E-04	1	1	0	0	0	0	0
4.90E-10	4.90E-04	3	0	0	0	0	0	0
5.25E-10	5.25E-04	1	0	1	0	0	0	0
5.62E-10	5.62E-04	1	0	1	0	0	0	0
6.03E-10	6.03E-04	0	3	0	0	0	0	0
6.46E-10	6.46E-04	2	1	0	0	0	0	0
6.92E-10	6.92E-04	0	0	0	0	0	0	0
7.41E-10	7.41E-04	0	1	0	0	0	0	0
7.94E-10	7.94E-04	0	1	0	0	0	0	0
8.51E-10	8.51E-04	0	1	0	0	0	0	0
9.12E-10	9.12E-04	3	0	1	0	0	0	0
9.77E-10	9.77E-04	1	0	0	0	0	0	0

1.05E-09	1.05E-03	0	2	0	0	0	0	0
1.12E-09	1.12E-03	1	0	0	0	0	0	0
1.20E-09	1.20E-03	1	0	0	0	0	0	0
1.29E-09	1.29E-03	1	1	0	0	0	0	0
1.38E-09	1.38E-03	1	0	0	0	0	0	0
1.48E-09	1.48E-03	0	2	1	0	0	0	0
1.58E-09	1.58E-03	1	0	1	0	0	0	0
1.70E-09	1.70E-03	0	0	0	0	0	0	0
1.82E-09	1.82E-03	1	1	0	0	0	0	0
1.95E-09	1.95E-03	3	1	0	0	0	0	0
2.09E-09	2.09E-03	1	0	2	0	0	0	0
2.24E-09	2.24E-03	6	1	1	0	0	0	0
2.40E-09	2.40E-03	4	0	0	0	0	0	0
2.57E-09	2.57E-03	2	1	1	0	0	0	0
2.75E-09	2.75E-03	2	0	0	0	0	0	0
2.95E-09	2.95E-03	3	0	1	0	0	0	0
3.16E-09	3.16E-03	3	0	0	0	0	0	0
3.39E-09	3.39E-03	3	0	1	0	0	0	0
3.63E-09	3.63E-03	4	1	1	0	0	0	0
3.89E-09	3.89E-03	7	1	0	0	0	0	0
4.17E-09	4.17E-03	5	2	0	0	0	0	0
4.47E-09	4.47E-03	3	1	1	0	0	0	0
4.79E-09	4.79E-03	4	3	1	0	0	0	0
5.13E-09	5.13E-03	2	4	0	0	0	0	0
5.50E-09	5.50E-03	8	0	0	0	0	0	0
5.89E-09	5.89E-03	6	1	2	0	0	0	0
6.31E-09	6.31E-03	9	4	1	0	0	0	0
6.76E-09	6.76E-03	9	1	0	0	0	0	0
7.24E-09	7.24E-03	13	1	0	0	0	0	0
7.76E-09	7.76E-03	8	3	2	0	0	0	0
8.32E-09	8.32E-03	13	3	3	0	1	0	0
8.91E-09	8.91E-03	8	2	1	0	0	0	0
9.55E-09	9.55E-03	11	6	1	0	0	0	0
1.02E-08	1.02E-02	18	11	2	0	0	0	0
1.10E-08	1.10E-02	21	7	3	0	0	0	0
1.17E-08	1.17E-02	17	7	2	1	0	0	0
1.26E-08	1.26E-02	17	6	3	0	0	0	0
1.35E-08	1.35E-02	15	5	3	0	0	0	0
1.45E-08	1.45E-02	11	7	2	0	0	0	0
1.55E-08	1.55E-02	16	3	1	0	0	0	0

1.66E-08	1.66E-02	24	11	2	1	0	0	0
1.78E-08	1.78E-02	29	5	3	0	0	0	0
1.91E-08	1.91E-02	21	10	5	1	0	0	0
2.04E-08	2.04E-02	14	5	2	1	0	0	0
2.19E-08	2.19E-02	24	8	3	1	1	0	0
2.34E-08	2.34E-02	26	9	0	0	0	0	0
2.51E-08	2.51E-02	27	13	4	0	0	0	0
2.69E-08	2.69E-02	21	8	5	0	0	0	0
2.88E-08	2.88E-02	34	7	7	0	0	0	0
3.09E-08	3.09E-02	45	12	3	0	0	0	0
3.31E-08	3.31E-02	40	11	7	0	0	0	0
3.55E-08	3.55E-02	33	17	9	0	1	0	0
3.80E-08	3.80E-02	49	15	5	0	0	0	0
4.07E-08	4.07E-02	52	20	2	0	1	0	0
4.37E-08	4.37E-02	51	11	11	0	0	0	0
4.68E-08	4.68E-02	48	22	6	3	0	0	0
5.01E-08	5.01E-02	45	21	8	0	0	0	0
5.37E-08	5.37E-02	56	17	8	0	0	0	0
5.75E-08	5.75E-02	60	26	6	0	0	0	0
6.17E-08	6.17E-02	76	29	7	1	0	0	0
6.61E-08	6.61E-02	44	32	11	0	1	0	0
7.08E-08	7.08E-02	73	24	5	2	1	0	0
7.59E-08	7.59E-02	84	25	8	2	0	0	0
8.13E-08	8.13E-02	88	31	13	1	0	0	0
8.71E-08	8.71E-02	86	38	8	3	1	0	0
9.33E-08	9.33E-02	93	34	23	1	2	0	0
1.00E-07	1.00E-01	96	25	19	0	1	0	0
1.07E-07	1.07E-01	139	33	10	4	2	0	0
1.15E-07	1.15E-01	128	38	17	3	0	0	0
1.23E-07	1.23E-01	132	45	21	2	0	0	0
1.32E-07	1.32E-01	123	50	25	1	1	0	0
1.41E-07	1.41E-01	139	46	14	2	1	0	0
1.51E-07	1.51E-01	153	50	30	1	0	0	0
1.62E-07	1.62E-01	169	56	22	1	1	0	0
1.74E-07	1.74E-01	188	64	22	4	0	0	0
1.86E-07	1.86E-01	183	83	37	2	1	0	0
2.00E-07	2.00E-01	187	76	36	2	2	0	0
2.14E-07	2.14E-01	189	85	30	8	5	0	0
2.29E-07	2.29E-01	216	94	26	4	2	0	0
2.45E-07	2.45E-01	227	112	41	10	3	0	0

2.63E-07	2.63E-01	253	100	53	9	1	0	0
2.82E-07	2.82E-01	274	126	42	4	3	0	0
3.02E-07	3.02E-01	300	111	51	3	0	0	0
3.24E-07	3.24E-01	307	100	46	10	1	0	0
3.47E-07	3.47E-01	342	129	47	6	3	0	0
3.72E-07	3.72E-01	362	125	72	6	3	0	0
3.98E-07	3.98E-01	366	153	70	5	1	0	0
4.27E-07	4.27E-01	422	168	61	1	4	0	0
4.57E-07	4.57E-01	466	166	63	16	5	0	0
4.90E-07	4.90E-01	454	194	80	10	5	0	0
5.25E-07	5.25E-01	544	177	67	13	7	0	0
5.62E-07	5.62E-01	561	218	91	11	4	0	0
6.03E-07	6.03E-01	593	243	92	12	3	0	0
6.46E-07	6.46E-01	625	253	85	12	4	1	0
6.92E-07	6.92E-01	696	256	127	15	3	0	0
7.41E-07	7.41E-01	732	267	134	17	9	0	0
7.94E-07	7.94E-01	797	292	124	22	10	0	0
8.51E-07	8.51E-01	823	331	156	24	4	0	0
9.12E-07	9.12E-01	917	357	148	25	11	0	0
9.77E-07	9.77E-01	994	382	127	22	12	1	0
1.05E-06	1.05E+00	1062	435	186	26	7	0	0
1.12E-06	1.12E+00	1209	462	190	27	10	2	0
1.20E-06	1.20E+00	1234	459	189	34	13	1	0
1.29E-06	1.29E+00	1322	540	219	38	6	0	0
1.38E-06	1.38E+00	1451	594	224	44	11	1	1
1.48E-06	1.48E+00	1561	614	274	45	13	0	1
1.58E-06	1.58E+00	1707	640	314	49	23	1	0
1.70E-06	1.70E+00	1728	788	309	59	17	2	0
1.82E-06	1.82E+00	1963	785	371	69	21	1	0
1.95E-06	1.95E+00	2099	875	403	76	26	1	0
2.09E-06	2.09E+00	2355	918	445	75	32	1	1
2.24E-06	2.24E+00	2536	979	430	73	28	0	0
2.40E-06	2.40E+00	2683	1054	444	93	29	1	1
2.57E-06	2.57E+00	2947	1210	551	91	41	0	1
2.75E-06	2.75E+00	3201	1331	590	90	34	2	1
2.95E-06	2.95E+00	3246	1425	680	120	46	2	0
3.16E-06	3.16E+00	3649	1579	703	136	36	2	0
3.39E-06	3.39E+00	3987	1643	770	130	63	1	0
3.63E-06	3.63E+00	4531	1791	868	150	54	5	0
3.89E-06	3.89E+00	4870	2022	961	172	80	5	2

4.17E-06	4.17E+00	5306	2240	996	191	83	0	1
4.47E-06	4.47E+00	5830	2483	1149	215	104	3	1
4.79E-06	4.79E+00	6145	2791	1292	229	105	7	2
5.13E-06	5.13E+00	7696	3286	1543	277	137	7	2
5.50E-06	5.50E+00	12384	5251	2416	443	203	10	2
5.89E-06	5.89E+00	12710	5527	2513	492	220	13	5
6.31E-06	6.31E+00	11940	5403	2448	531	229	9	6
6.76E-06	6.76E+00	11363	5093	2576	553	241	12	5
7.24E-06	7.24E+00	11145	5237	2688	609	263	16	11
7.76E-06	7.76E+00	11379	5462	2818	687	330	19	4
8.32E-06	8.32E+00	11726	5956	2973	788	369	23	16
8.91E-06	8.91E+00	12383	6264	3345	865	428	30	8
9.55E-06	9.55E+00	13391	6923	3660	1027	537	37	8
1.02E-05	1.02E+01	14214	7401	4013	1060	567	53	21
1.10E-05	1.10E+01	16496	8458	4635	1275	658	55	25
1.17E-05	1.17E+01	17660	9316	5198	1464	773	50	31
1.26E-05	1.26E+01	18093	9777	5255	1643	859	80	35
1.35E-05	1.35E+01	18136	9962	5625	1892	995	114	43
1.45E-05	1.45E+01	18573	10868	6196	2170	1198	136	52
1.55E-05	1.55E+01	19567	11619	6669	2337	1329	164	55
1.66E-05	1.66E+01	20407	12606	7273	2685	1540	184	103
1.78E-05	1.78E+01	20773	13451	7815	2972	1702	238	126
1.91E-05	1.91E+01	21104	14316	8249	3311	1934	288	130
2.04E-05	2.04E+01	21694	14970	8659	3549	2248	323	170
2.19E-05	2.19E+01	21771	15977	9535	3892	2500	462	222
2.34E-05	2.34E+01	22148	16948	10213	4456	2821	528	278
2.51E-05	2.51E+01	21945	17902	10702	4718	3128	624	334
2.69E-05	2.69E+01	22249	18738	11738	5024	3488	741	442
2.88E-05	2.88E+01	21568	19552	12364	5556	3716	916	523
3.09E-05	3.09E+01	21475	20565	13153	6025	4220	1111	615
3.31E-05	3.31E+01	20754	21090	14095	6429	4485	1417	771
3.55E-05	3.55E+01	20019	21857	14994	6934	4989	1527	948
3.80E-05	3.80E+01	19432	22485	16078	7338	5353	1759	1139
4.07E-05	4.07E+01	18663	23305	16662	7843	5906	2128	1419
4.37E-05	4.37E+01	17770	23539	18014	8442	6161	2394	1584
4.68E-05	4.68E+01	17455	23682	18985	8819	6683	2723	1813
5.01E-05	5.01E+01	16451	23768	20132	9378	7374	3095	2092
5.37E-05	5.37E+01	15805	23402	21044	10120	7612	3524	2420
5.75E-05	5.75E+01	15130	23255	21911	10961	8182	3834	2825
6.17E-05	6.17E+01	13896	22613	22845	11835	8807	4151	3190

6.61E-05	6.61E+01	13515	21932	23696	12607	9413	4673	3545
7.08E-05	7.08E+01	12768	21242	23947	13706	9972	5024	3894
7.59E-05	7.59E+01	12080	20651	24460	14462	10698	5402	4382
8.13E-05	8.13E+01	11735	19638	24494	15630	11430	5850	4797
8.71E-05	8.71E+01	11029	18752	24593	16579	12281	6335	5254
9.33E-05	9.33E+01	10236	18108	24419	17668	13091	6714	5576
1.00E-04	1.00E+02	9859	17004	23814	18681	14128	7102	5996
1.07E-04	1.07E+02	9375	16614	23057	19914	15241	7325	6340
1.15E-04	1.15E+02	8720	15552	22322	20973	16069	8031	6761
1.23E-04	1.23E+02	8409	15050	21467	22301	17236	8606	7214
1.32E-04	1.32E+02	7753	14146	20592	22869	18400	9280	7642
1.41E-04	1.41E+02	7439	13680	19833	24081	19133	9763	8272
1.51E-04	1.51E+02	7010	13064	18796	24781	20436	10568	8651
1.62E-04	1.62E+02	6640	12329	17758	25405	21411	11081	9346
1.74E-04	1.74E+02	6206	11730	17327	25500	22566	12043	9841
1.86E-04	1.86E+02	5809	11084	16455	25620	23499	13096	10617
2.00E-04	2.00E+02	5558	10530	15671	25227	24530	13910	11361
2.14E-04	2.14E+02	5138	10109	15053	24644	25373	15056	12187
2.29E-04	2.29E+02	4981	9518	14381	23957	25916	16052	13327
2.45E-04	2.45E+02	4516	9080	13470	23004	26006	17097	14057
2.63E-04	2.63E+02	4309	8423	13168	22071	25745	18319	15455
2.82E-04	2.82E+02	3961	7920	12410	20897	25299	19125	16052
3.02E-04	3.02E+02	3754	7700	11704	20303	24614	20194	17536
3.24E-04	3.24E+02	3571	7162	11086	19513	23422	21068	18347
3.47E-04	3.47E+02	3311	6931	10601	18592	22390	21973	19533
3.72E-04	3.72E+02	3034	6467	10069	17567	21556	23219	20218
3.98E-04	3.98E+02	2877	5877	9626	16842	20790	24590	21198
4.27E-04	4.27E+02	2724	5667	9157	16449	19371	25922	22579
4.57E-04	4.57E+02	2438	5282	8761	15437	18955	26086	23686
4.90E-04	4.90E+02	2413	5183	8273	14583	18081	26568	24850
5.25E-04	5.25E+02	2144	4685	7712	14160	17205	26218	25537
5.62E-04	5.62E+02	1920	4494	7408	13378	16372	25272	26349
6.03E-04	6.03E+02	1857	4135	6893	12714	15684	24310	26776
6.46E-04	6.46E+02	1693	3966	6452	12356	14960	23616	26111
6.92E-04	6.92E+02	1631	3673	6339	11654	14440	22484	25270
7.41E-04	7.41E+02	1457	3436	5699	11009	13532	21653	24336
7.94E-04	7.94E+02	1325	3181	5494	10371	13180	20912	23352
8.51E-04	8.51E+02	1312	2972	5023	9959	12506	19872	22358
9.12E-04	9.12E+02	1123	2847	4651	9508	11882	19200	21450
9.77E-04	9.77E+02	1031	2553	4549	9025	11397	18264	20550

1.05E-03	1.05E+03	1044	2394	4278	8447	10772	17486	19587
1.12E-03	1.12E+03	969	2298	3945	8070	10303	16938	18988
1.20E-03	1.20E+03	763	2079	3834	7654	9696	15844	18225
1.29E-03	1.29E+03	692	1978	3485	7207	9181	15224	17242
1.38E-03	1.38E+03	749	1801	3263	6796	8641	14689	16548
1.48E-03	1.48E+03	847	1678	3042	6391	8191	13974	15843
1.58E-03	1.58E+03	528	1687	2857	6021	7878	13279	15177
1.70E-03	1.70E+03	358	1336	2684	5712	7345	12638	14486
1.82E-03	1.82E+03	478	1323	2437	5345	6957	12023	13778
1.95E-03	1.95E+03	626	1381	2409	5034	6573	11406	13076
2.09E-03	2.09E+03	608	955	2008	4644	6196	10828	12538
2.24E-03	2.24E+03	278	1040	2059	4468	5816	10240	11840
2.40E-03	2.40E+03	270	1079	1839	4172	5498	9852	11365
2.57E-03	2.57E+03	402	950	1654	3916	5201	9253	10768
2.75E-03	2.75E+03	121	748	1715	3670	4876	8827	10147
2.95E-03	2.95E+03	266	601	1436	3405	4582	8308	9734
3.16E-03	3.16E+03	490	763	1167	3243	4327	8025	9166
3.39E-03	3.39E+03	334	993	1546	2839	4027	7524	8805
3.63E-03	3.63E+03	290	322	1070	2937	3716	7132	8400
3.89E-03	3.89E+03	142	351	884	2525	3557	6672	7784
4.17E-03	4.17E+03	4	545	1161	2470	3221	6312	7358
4.47E-03	4.47E+03	4	655	977	2352	3097	5987	6961
4.79E-03	4.79E+03	14	618	803	1869	2817	5643	6593
5.13E-03	5.13E+03	171	129	584	2235	2849	5275	6242
5.50E-03	5.50E+03	563	341	686	1640	2354	4999	5899
5.89E-03	5.89E+03	53	389	1109	1614	2535	4683	5524
6.31E-03	6.31E+03	206	43	486	1827	1929	4348	5157
6.76E-03	6.76E+03	170	336	194	1229	2160	4208	4889
7.24E-03	7.24E+03	2	498	586	1184	1913	3717	4626
7.76E-03	7.76E+03	0	312	561	1671	1606	3673	4273
8.32E-03	8.32E+03	0	310	744	822	1717	3281	4185
8.91E-03	8.91E+03	0	60	229	985	1576	3365	3680
9.55E-03	9.55E+03	1	1	136	1109	1031	2681	3630
1.02E-02	1.02E+04	3	11	599	1019	1668	2981	3117
1.10E-02	1.10E+04	85	15	48	693	1090	2430	3306
1.17E-02	1.17E+04	305	273	118	600	808	2444	2718
1.26E-02	1.26E+04	4	497	639	606	1252	2209	2910
1.35E-02	1.35E+04	2	12	366	1344	1002	1948	2327
1.45E-02	1.45E+04	0	324	224	146	873	2239	2526
1.55E-02	1.55E+04	0	51	181	293	477	1509	1969

1.66E-02	1.66E+04	0	0	0	556	676	1586	2118
1.78E-02	1.78E+04	0	0	8	667	1113	1838	2047
1.91E-02	1.91E+04	11	0	10	714	656	1146	1621
2.04E-02	2.04E+04	383	0	60	65	85	1300	1596
2.19E-02	2.19E+04	2	4	708	275	674	1581	1689
2.34E-02	2.34E+04	0	3	17	475	416	762	997
2.51E-02	2.51E+04	0	217	192	29	831	1102	1621
2.69E-02	2.69E+04	0	172	189	225	308	1010	1178
2.88E-02	2.88E+04	0	4	0	572	55	994	800
3.09E-02	3.09E+04	0	0	0	358	686	593	1310
3.31E-02	3.31E+04	0	0	0	339	36	714	1012
3.55E-02	3.55E+04	0	0	0	31	50	651	880
3.80E-02	3.80E+04	0	0	0	0	711	1196	430
4.07E-02	4.07E+04	0	0	4	11	332	52	739
4.37E-02	4.37E+04	0	24	20	14	141	455	955
4.68E-02	4.68E+04	0	372	372	136	303	442	816
5.01E-02	5.01E+04	0	0	4	633	0	902	71
5.37E-02	5.37E+04	0	0	0	11	0	463	703
5.75E-02	5.75E+04	0	0	0	372	14	35	332
6.17E-02	6.17E+04	0	0	0	7	27	499	874
6.61E-02	6.61E+04	0	0	0	0	745	243	339
7.08E-02	7.08E+04	0	0	0	0	15	36	39
7.59E-02	7.59E+04	0	0	6	0	35	494	712
8.13E-02	8.13E+04	0	0	389	0	348	346	23
8.71E-02	8.71E+04	0	0	1	2	0	319	37
9.33E-02	9.33E+04	0	0	0	4	0	357	740
1.00E-01	1.00E+05	0	0	0	150	0	0	290
1.07E-01	1.07E+05	0	0	0	240	0	0	132
1.15E-01	1.15E+05	0	0	0	4	0	12	344
1.23E-01	1.23E+05	0	0	0	0	4	18	0
1.32E-01	1.32E+05	0	0	0	0	8	437	0
1.41E-01	1.41E+05	0	0	0	0	384	329	12
1.51E-01	1.51E+05	0	0	0	0	1	13	25
1.62E-01	1.62E+05	0	0	0	0	3	375	751
1.74E-01	1.74E+05	1	0	0	9	0	0	9
1.86E-01	1.86E+05	99	0	0	387	0	0	22
2.00E-01	2.00E+05	0	0	0	0	0	0	365
2.14E-01	2.14E+05	0	0	0	0	0	0	0
2.29E-01	2.29E+05	0	0	0	0	4	0	0
2.45E-01	2.45E+05	0	0	0	0	391	4	0

2.63E-01	2.63E+05	0	0	0	0	1	6	0
2.82E-01	2.82E+05	0	0	0	0	0	386	0
3.02E-01	3.02E+05	0	0	0	0	0	0	4
3.24E-01	3.24E+05	0	0	0	0	0	4	8
3.47E-01	3.47E+05	0	0	0	0	0	0	384
3.72E-01	3.72E+05	0	0	0	0	0	0	0
3.98E-01	3.98E+05	0	1	0	0	0	0	4
4.27E-01	4.27E+05	0	99	0	0	0	0	0
4.57E-01	4.57E+05	0	0	0	0	0	0	0
4.90E-01	4.90E+05	0	0	0	0	0	17	0
5.25E-01	5.25E+05	0	0	0	0	0	379	0
5.62E-01	5.62E+05	0	0	0	0	0	0	4
6.03E-01	6.03E+05	0	0	0	0	0	0	388
6.46E-01	6.46E+05	0	0	0	0	0	0	4
6.92E-01	6.92E+05	0	0	1	0	0	0	0
7.41E-01	7.41E+05	0	0	99	0	0	0	0
7.94E-01	7.94E+05	0	0	0	0	0	0	0
8.51E-01	8.51E+05	0	0	0	0	0	0	0
9.12E-01	9.12E+05	0	0	0	0	0	0	0
9.77E-01	9.77E+05	0	0	0	0	0	0	0
1.05E+00	1.05E+06	0	0	0	0	0	0	0
1.12E+00	1.12E+06	0	0	0	0	0	0	0
1.20E+00	1.20E+06	0	0	0	0	0	0	0
1.29E+00	1.29E+06	0	0	0	0	0	0	0
1.38E+00	1.38E+06	0	0	0	0	0	0	0
1.48E+00	1.48E+06	0	0	0	0	0	0	0
1.58E+00	1.58E+06	0	0	0	1	0	0	0
1.70E+00	1.70E+06	0	0	0	99	0	0	0
1.82E+00	1.82E+06	0	0	0	0	0	0	0
1.95E+00	1.95E+06	0	0	0	0	0	0	0
2.09E+00	2.09E+06	0	0	0	0	1	0	0
2.24E+00	2.24E+06	0	0	0	0	90	0	0
2.40E+00	2.40E+06	0	0	0	0	9	0	0
2.57E+00	2.57E+06	0	0	0	0	0	0	0
2.75E+00	2.75E+06	0	0	0	0	0	0	0
2.95E+00	2.95E+06	0	0	0	0	0	0	0
3.16E+00	3.16E+06	0	0	0	0	0	0	0
3.39E+00	3.39E+06	0	0	0	0	0	0	0
3.63E+00	3.63E+06	0	0	0	0	0	0	0
3.89E+00	3.89E+06	0	0	0	0	0	0	0

4.17E+00	4.17E+06	0	0	0	0	0	0	0
4.47E+00	4.47E+06	0	0	0	0	0	1	0
4.79E+00	4.79E+06	0	0	0	0	0	99	0
5.13E+00	5.13E+06	0	0	0	0	0	0	1
5.50E+00	5.50E+06	0	0	0	0	0	0	9
5.89E+00	5.89E+06	0	0	0	0	0	0	90
# Targets hit ---->		939598	983485	994691	999524	999860	999998	1000000

Table B5. Dose (Gy) deposited in voxels inside the cylinder mesh geometry by ions of equal stopping power (100 keV um^{-1}). FLUKA data is scaled as GeV-cm^{-3} and described in the 'Bin' column. Un-hit voxels appear in the first row for each ion. The number of hit voxels is summed and listed at the bottom of the table.

Dose (Gy)	Bin	Be-8 Voxels hit	C-12 Voxels hit	O-16 Voxels hit	Mg-24 Voxels hit	Si-28 Voxels hit	Ca-40 Voxels hit	Ti-48 Voxels hit
1.60E-09	1.00E-02	43923	0	0	0	0	0	0
1.72E-09	1.07E-02	0	0	0	0	0	0	0
1.85E-09	1.15E-02	0	0	0	0	0	0	0
1.99E-09	1.24E-02	0	0	0	0	0	0	0
2.13E-09	1.33E-02	0	0	0	0	0	0	0
2.29E-09	1.43E-02	0	0	0	0	0	0	0
2.46E-09	1.54E-02	0	0	0	0	0	0	0
2.65E-09	1.65E-02	0	0	0	0	0	0	0
2.84E-09	1.77E-02	0	0	0	0	0	0	0
3.05E-09	1.91E-02	2	0	0	0	0	0	0
3.28E-09	2.05E-02	0	0	0	0	0	0	0
3.53E-09	2.20E-02	0	0	0	0	0	0	0
3.79E-09	2.36E-02	0	0	0	0	0	0	0
4.07E-09	2.54E-02	1	0	0	0	0	0	0
4.37E-09	2.73E-02	0	0	0	0	0	0	0
4.70E-09	2.93E-02	0	0	0	0	0	0	0
5.05E-09	3.15E-02	0	0	0	0	0	0	0
5.42E-09	3.38E-02	0	0	0	0	0	0	0
5.82E-09	3.64E-02	0	0	0	0	0	0	0
6.26E-09	3.91E-02	0	0	0	0	0	0	0
6.72E-09	4.20E-02	1	0	0	0	0	0	0
7.22E-09	4.51E-02	0	0	0	0	0	0	0
7.76E-09	4.84E-02	0	0	0	0	0	0	0
8.34E-09	5.20E-02	1	0	0	0	0	0	0
8.96E-09	5.59E-02	1	0	0	0	0	0	0
9.62E-09	6.01E-02	1	0	0	0	0	0	0
1.03E-08	6.45E-02	0	0	0	0	0	0	0
1.11E-08	6.93E-02	0	0	0	0	0	0	0
1.19E-08	7.45E-02	0	0	0	0	0	0	0
1.28E-08	8.00E-02	0	0	0	0	0	0	0
1.38E-08	8.59E-02	3	0	0	0	0	0	0
1.48E-08	9.23E-02	1	0	0	0	0	0	0
1.59E-08	9.92E-02	1	0	0	0	0	0	0
1.71E-08	1.07E-01	1	0	0	0	0	0	0

1.83E-08	1.15E-01	2	0	0	0	0	0	0
1.97E-08	1.23E-01	1	0	0	0	0	0	0
2.12E-08	1.32E-01	2	0	0	0	0	0	0
2.27E-08	1.42E-01	1	0	0	0	0	0	0
2.44E-08	1.53E-01	2	0	0	0	0	0	0
2.63E-08	1.64E-01	2	0	0	0	0	0	0
2.82E-08	1.76E-01	1	0	0	0	0	0	0
3.03E-08	1.89E-01	0	0	0	0	0	0	0
3.26E-08	2.03E-01	1	0	0	0	0	0	0
3.50E-08	2.18E-01	3	0	0	0	0	0	0
3.76E-08	2.35E-01	6	0	0	0	0	0	0
4.04E-08	2.52E-01	3	0	0	0	0	0	0
4.34E-08	2.71E-01	0	0	0	0	0	0	0
4.66E-08	2.91E-01	4	0	0	0	0	0	0
5.01E-08	3.12E-01	3	0	0	0	0	0	0
5.38E-08	3.36E-01	6	0	0	0	0	0	0
5.78E-08	3.61E-01	2	0	0	0	0	0	0
6.21E-08	3.87E-01	8	0	0	0	0	0	0
6.67E-08	4.16E-01	6	0	0	0	0	0	0
7.16E-08	4.47E-01	3	0	0	0	0	0	0
7.70E-08	4.80E-01	7	0	0	0	0	0	0
8.27E-08	5.16E-01	8	0	0	0	0	0	0
8.88E-08	5.55E-01	5	0	0	0	0	0	0
9.54E-08	5.96E-01	7	0	0	0	0	0	0
1.03E-07	6.40E-01	7	0	0	0	0	0	0
1.10E-07	6.88E-01	10	0	0	0	0	0	0
1.18E-07	7.39E-01	11	0	0	0	0	0	0
1.27E-07	7.94E-01	8	0	0	0	0	0	0
1.37E-07	8.53E-01	16	0	0	0	0	0	0
1.47E-07	9.16E-01	15	0	0	0	0	0	0
1.58E-07	9.84E-01	9	0	0	0	0	0	0
1.69E-07	1.06E+00	11	0	0	0	0	0	0
1.82E-07	1.14E+00	16	0	0	0	0	0	0
1.96E-07	1.22E+00	19	0	0	0	0	0	0
2.10E-07	1.31E+00	16	0	0	0	0	0	0
2.26E-07	1.41E+00	19	0	0	0	0	0	0
2.42E-07	1.51E+00	20	0	0	0	0	0	0
2.60E-07	1.63E+00	20	0	0	0	0	0	0
2.80E-07	1.75E+00	20	0	0	0	0	0	0
3.01E-07	1.88E+00	14	0	0	0	0	0	0

3.23E-07	2.02E+00	34	0	0	0	0	0	0
3.47E-07	2.17E+00	20	0	0	0	0	0	0
3.73E-07	2.33E+00	24	0	0	0	0	0	0
4.00E-07	2.50E+00	32	0	0	0	0	0	0
4.30E-07	2.69E+00	36	0	0	0	0	0	0
4.62E-07	2.89E+00	33	0	0	0	0	0	0
4.97E-07	3.10E+00	33	0	0	0	0	0	0
5.34E-07	3.33E+00	38	0	0	0	0	0	0
5.73E-07	3.58E+00	38	0	0	0	0	0	0
6.16E-07	3.84E+00	35	0	0	0	0	0	0
6.62E-07	4.13E+00	41	0	0	0	0	0	0
7.11E-07	4.44E+00	50	0	0	0	0	0	0
7.64E-07	4.77E+00	53	0	0	0	0	0	0
8.20E-07	5.12E+00	72	0	0	0	0	0	0
8.81E-07	5.50E+00	50	0	0	0	0	0	0
9.47E-07	5.91E+00	55	0	0	0	0	0	0
1.02E-06	6.35E+00	77	0	0	0	0	0	0
1.09E-06	6.82E+00	88	0	0	0	0	0	0
1.17E-06	7.33E+00	81	0	0	0	0	0	0
1.26E-06	7.87E+00	95	0	0	0	0	0	0
1.36E-06	8.46E+00	95	0	0	0	0	0	0
1.46E-06	9.09E+00	98	0	0	0	0	0	0
1.56E-06	9.76E+00	114	0	0	0	0	0	0
1.68E-06	1.05E+01	124	0	0	0	0	0	0
1.81E-06	1.13E+01	143	0	0	0	0	0	0
1.94E-06	1.21E+01	154	0	0	0	0	0	0
2.08E-06	1.30E+01	165	0	0	0	0	0	0
2.24E-06	1.40E+01	172	0	0	0	0	0	0
2.41E-06	1.50E+01	180	0	0	0	0	0	0
2.58E-06	1.61E+01	203	0	0	0	0	0	0
2.78E-06	1.73E+01	231	0	0	0	0	0	0
2.98E-06	1.86E+01	223	0	0	0	0	0	0
3.20E-06	2.00E+01	241	0	0	0	0	0	0
3.44E-06	2.15E+01	276	0	0	0	0	0	0
3.70E-06	2.31E+01	317	0	0	0	0	0	0
3.97E-06	2.48E+01	329	0	0	0	0	0	0
4.27E-06	2.66E+01	367	0	0	0	0	0	0
4.59E-06	2.86E+01	362	0	0	0	0	0	0
4.93E-06	3.07E+01	447	0	0	0	0	0	0
5.29E-06	3.30E+01	479	0	0	0	0	0	0

5.69E-06	3.55E+01	549	0	0	0	0	0	0
6.11E-06	3.81E+01	532	0	0	0	0	0	0
6.56E-06	4.10E+01	630	0	0	0	0	0	0
7.05E-06	4.40E+01	735	0	0	0	0	0	0
7.58E-06	4.73E+01	779	0	0	0	0	0	0
8.14E-06	5.08E+01	790	0	0	0	0	0	0
8.74E-06	5.46E+01	897	0	0	0	0	0	0
9.39E-06	5.86E+01	1045	0	0	0	0	0	0
1.01E-05	6.30E+01	1211	0	0	0	0	0	0
1.08E-05	6.77E+01	1233	0	0	0	0	0	0
1.16E-05	7.27E+01	1282	0	0	0	0	0	0
1.25E-05	7.81E+01	1447	0	0	0	0	0	0
1.34E-05	8.39E+01	1393	0	0	0	0	0	0
1.44E-05	9.01E+01	1585	0	0	0	0	0	0
1.55E-05	9.69E+01	1423	0	0	0	0	0	0
1.67E-05	1.04E+02	1526	0	0	0	0	0	0
1.79E-05	1.12E+02	1687	0	0	0	0	0	0
1.92E-05	1.20E+02	1688	0	0	0	0	0	0
2.07E-05	1.29E+02	1663	0	0	0	0	0	0
2.22E-05	1.39E+02	1755	0	0	0	0	0	0
2.39E-05	1.49E+02	1854	0	0	0	0	0	0
2.56E-05	1.60E+02	1886	0	0	0	0	0	0
2.75E-05	1.72E+02	1902	0	0	0	0	0	0
2.96E-05	1.85E+02	1942	0	0	0	0	0	0
3.18E-05	1.98E+02	1981	0	0	0	0	0	0
3.41E-05	2.13E+02	1972	0	0	0	0	0	0
3.67E-05	2.29E+02	1965	0	0	0	0	0	0
3.94E-05	2.46E+02	2068	0	0	0	0	0	0
4.23E-05	2.64E+02	2034	0	0	0	0	0	0
4.55E-05	2.84E+02	2128	0	0	0	0	0	0
4.89E-05	3.05E+02	2133	0	0	0	0	0	0
5.25E-05	3.28E+02	2173	0	0	0	0	0	0
5.64E-05	3.52E+02	2198	0	0	0	0	0	0
6.06E-05	3.78E+02	2248	0	0	0	0	0	0
6.51E-05	4.06E+02	2338	0	0	0	0	0	0
6.99E-05	4.37E+02	2281	0	0	0	0	0	0
7.51E-05	4.69E+02	2405	0	0	0	0	0	0
8.07E-05	5.04E+02	2349	0	0	0	0	0	0
8.67E-05	5.41E+02	2323	0	0	0	0	0	0
9.32E-05	5.82E+02	2447	0	0	0	0	0	0

1.00E-04	6.25E+02	2328	0	0	0	0	0	0
1.08E-04	6.71E+02	2479	0	0	0	0	0	0
1.16E-04	7.21E+02	2467	0	0	0	0	0	0
1.24E-04	7.75E+02	2440	0	0	0	0	0	0
1.33E-04	8.32E+02	2503	0	0	0	0	0	0
1.43E-04	8.94E+02	2423	0	0	0	0	0	0
1.54E-04	9.61E+02	2514	0	0	0	0	0	0
1.65E-04	1.03E+03	2449	5	0	0	0	0	0
1.78E-04	1.11E+03	2539	2	0	0	0	0	0
1.91E-04	1.19E+03	2481	4	0	0	0	0	0
2.05E-04	1.28E+03	2408	14	0	0	0	0	0
2.20E-04	1.38E+03	2454	13	0	0	0	0	0
2.37E-04	1.48E+03	2511	24	0	0	0	0	0
2.54E-04	1.59E+03	2573	43	0	0	0	0	0
2.73E-04	1.71E+03	2627	77	0	0	0	0	0
2.94E-04	1.83E+03	2738	99	0	0	0	0	0
3.15E-04	1.97E+03	2853	139	1	0	0	0	0
3.39E-04	2.11E+03	2907	182	3	0	0	0	0
3.64E-04	2.27E+03	2967	247	6	0	0	0	0
3.91E-04	2.44E+03	2946	321	11	0	0	0	0
4.20E-04	2.62E+03	3050	346	31	0	0	0	0
4.51E-04	2.82E+03	3075	459	39	1	0	0	0
4.85E-04	3.03E+03	3162	583	74	4	1	0	1
5.21E-04	3.25E+03	3139	630	129	2	1	0	1
5.60E-04	3.49E+03	3202	802	164	6	0	1	4
6.01E-04	3.75E+03	3283	897	255	27	8	2	2
6.46E-04	4.03E+03	3190	1068	329	37	20	5	10
6.94E-04	4.33E+03	3151	1167	429	57	41	12	17
7.45E-04	4.65E+03	3222	1216	534	112	69	23	48
8.01E-04	5.00E+03	3250	1375	622	159	81	44	63
8.60E-04	5.37E+03	3227	1526	759	258	135	70	112
9.24E-04	5.77E+03	3317	1648	893	311	222	125	171
9.93E-04	6.20E+03	3302	1732	1045	454	267	186	296
1.07E-03	6.66E+03	3495	1917	1183	590	401	278	345
1.15E-03	7.15E+03	3335	1978	1422	706	557	360	483
1.23E-03	7.69E+03	3529	2279	1589	830	686	534	655
1.32E-03	8.26E+03	3425	2329	1690	1084	839	704	776
1.42E-03	8.87E+03	3426	2669	1812	1234	1071	849	894
1.53E-03	9.53E+03	3508	2838	2006	1414	1286	1045	1209
1.64E-03	1.02E+04	3507	3100	2305	1680	1524	1308	1517

1.76E-03	1.10E+04	3443	3220	2495	1885	1779	1554	1825
1.89E-03	1.18E+04	3543	3686	2735	2208	2045	1856	2221
2.03E-03	1.27E+04	3530	3840	3040	2386	2179	2254	2822
2.19E-03	1.36E+04	3591	4209	3205	2722	2501	2584	3457
2.35E-03	1.47E+04	3592	4655	3576	3058	2872	3241	4851
2.52E-03	1.57E+04	3543	5239	3960	3373	3417	4301	6972
2.71E-03	1.69E+04	3573	6101	4477	4000	4118	6100	9458
2.91E-03	1.82E+04	3664	6957	5086	5018	5446	8485	11616
3.13E-03	1.95E+04	3572	7959	6067	6498	7203	10948	13088
3.36E-03	2.10E+04	3577	8574	7293	8532	9323	12714	13463
3.61E-03	2.25E+04	3607	9354	8817	10517	11377	13432	13698
3.88E-03	2.42E+04	3686	9577	10088	11866	12548	13490	13258
4.17E-03	2.60E+04	3635	9478	10610	12558	12931	13270	13209
4.48E-03	2.79E+04	3656	9253	11153	12401	13042	13003	12564
4.81E-03	3.00E+04	3705	9339	11007	11890	12623	12581	12093
5.17E-03	3.23E+04	3570	9266	10613	11895	12533	12236	11568
5.55E-03	3.46E+04	3704	8999	10450	11978	11967	12007	11349
5.96E-03	3.72E+04	3599	9140	10407	11552	11549	11643	10984
6.41E-03	4.00E+04	3525	8741	10073	11321	11305	11144	10838
6.88E-03	4.30E+04	3586	8474	10034	11020	11071	10715	10554
7.40E-03	4.62E+04	3614	8337	9583	10606	10667	10388	10260
7.95E-03	4.96E+04	3663	8143	9317	10126	10367	10221	9719
8.54E-03	5.33E+04	3629	8054	9171	10032	9994	9927	9528
9.17E-03	5.72E+04	3454	7875	8983	9563	9697	9708	9151
9.85E-03	6.15E+04	3543	7538	8911	9480	9517	9264	9006
1.06E-02	6.61E+04	3550	7575	8886	9179	9186	9000	8787
1.14E-02	7.10E+04	3672	7612	8550	8904	9019	8655	8479
1.22E-02	7.63E+04	3477	7302	8606	8761	8466	8545	8170
1.31E-02	8.19E+04	3460	7084	8105	8557	8518	8207	7702
1.41E-02	8.80E+04	3474	7155	7813	8225	8228	7902	7517
1.51E-02	9.46E+04	3290	7060	7705	7892	7891	7576	7357
1.63E-02	1.02E+05	3468	6657	7341	7773	7808	7278	7170
1.75E-02	1.09E+05	3345	6666	7404	7605	7501	7150	6806
1.88E-02	1.17E+05	3484	6508	7214	7212	7115	7053	6637
2.02E-02	1.26E+05	3243	6424	6951	6886	6922	6828	6322
2.17E-02	1.35E+05	3326	5964	6767	6684	6731	6523	6191
2.33E-02	1.45E+05	3265	5907	6600	6464	6479	6200	6002
2.50E-02	1.56E+05	3222	5982	6296	6367	6289	5908	5796
2.69E-02	1.68E+05	3140	5842	6440	6162	6077	5701	5651
2.89E-02	1.80E+05	3155	5683	5984	6100	5766	5524	5293

3.10E-02	1.94E+05	3082	5491	5985	5714	5684	5430	5133
3.33E-02	2.08E+05	2936	5258	5624	5767	5471	5294	5003
3.58E-02	2.24E+05	3056	5159	5499	5255	5313	5093	4821
3.85E-02	2.40E+05	2836	5048	5367	5183	5269	4807	4802
4.13E-02	2.58E+05	2948	5058	5274	5073	5095	4747	4534
4.44E-02	2.77E+05	2928	4872	4978	4983	4736	4547	4301
4.77E-02	2.98E+05	2825	4775	4931	4557	4600	4550	4228
5.13E-02	3.20E+05	2862	4631	4771	4571	4581	4290	4101
5.51E-02	3.44E+05	2665	4552	4615	4535	4352	4126	3961
5.92E-02	3.69E+05	2647	4421	4380	4404	4188	3996	3873
6.36E-02	3.97E+05	2725	4195	4237	4184	3994	3940	3710
6.83E-02	4.26E+05	2559	4141	4219	4059	4048	3741	3500
7.34E-02	4.58E+05	2505	4025	3965	3829	3807	3580	3366
7.88E-02	4.92E+05	2483	3824	3922	3616	3739	3467	3383
8.47E-02	5.29E+05	2406	3769	3835	3675	3537	3465	3139
9.10E-02	5.68E+05	2365	3716	3740	3432	3457	3288	3170
9.77E-02	6.10E+05	2367	3596	3508	3422	3389	3092	2971
1.05E-01	6.55E+05	2263	3509	3450	3276	3223	2998	2946
1.13E-01	7.04E+05	2201	3385	3387	3091	2978	2875	2769
1.21E-01	7.56E+05	2153	3327	3261	3077	3005	2819	2745
1.30E-01	8.13E+05	2142	3094	3114	3036	2841	2720	2693
1.40E-01	8.73E+05	2019	3090	2998	2929	2791	2646	2551
1.50E-01	9.38E+05	2083	3008	2992	2692	2786	2619	2412
1.61E-01	1.01E+06	1918	2882	2822	2710	2614	2509	2343
1.73E-01	1.08E+06	2001	2804	2737	2604	2507	2408	2331
1.86E-01	1.16E+06	1871	2651	2697	2467	2462	2309	2188
2.00E-01	1.25E+06	1855	2674	2494	2401	2345	2235	2082
2.15E-01	1.34E+06	1734	2588	2486	2283	2285	2133	2022
2.31E-01	1.44E+06	1807	2510	2404	2230	2188	2059	1966
2.48E-01	1.55E+06	1659	2384	2323	2178	2162	2045	1924
2.67E-01	1.66E+06	1662	2342	2262	2075	2069	1852	1844
2.87E-01	1.79E+06	1653	2176	2187	2067	1967	1892	1784
3.08E-01	1.92E+06	1566	2222	2134	1942	1953	1774	1710
3.31E-01	2.06E+06	1583	2119	1971	1946	1871	1699	1657
3.55E-01	2.22E+06	1451	1990	1911	1813	1751	1693	1576
3.82E-01	2.38E+06	1422	1959	1878	1717	1682	1563	1532
4.10E-01	2.56E+06	1396	1901	1784	1658	1689	1529	1415
4.41E-01	2.75E+06	1355	1875	1788	1639	1560	1563	1505
4.73E-01	2.95E+06	1354	1819	1631	1546	1544	1444	1365
5.09E-01	3.17E+06	1255	1727	1648	1585	1487	1365	1381

5.46E-01	3.41E+06	1252	1645	1555	1457	1470	1387	1274
5.87E-01	3.66E+06	1251	1615	1569	1447	1416	1295	1300
6.31E-01	3.94E+06	1202	1509	1472	1356	1331	1289	1229
6.77E-01	4.23E+06	1179	1488	1435	1290	1259	1226	1169
7.28E-01	4.54E+06	1147	1451	1362	1310	1266	1186	1116
7.82E-01	4.88E+06	1092	1414	1339	1241	1246	1164	1066
8.40E-01	5.24E+06	1061	1348	1265	1203	1163	1062	1047
9.02E-01	5.63E+06	1003	1333	1208	1131	1150	1103	1026
9.70E-01	6.05E+06	1057	1267	1248	1125	1089	1024	982
1.04E+00	6.50E+06	963	1203	1105	1088	1058	978	959
1.12E+00	6.98E+06	937	1192	1117	1060	1042	969	905
1.20E+00	7.50E+06	886	1119	1083	999	1018	939	871
1.29E+00	8.06E+06	893	1114	1064	982	939	886	865
1.39E+00	8.66E+06	839	1111	1013	914	917	846	831
1.49E+00	9.31E+06	847	1012	996	926	888	859	779
1.60E+00	1.00E+07	828	997	921	877	822	803	755
1.72E+00	1.07E+07	795	980	940	880	854	772	797
1.85E+00	1.15E+07	736	924	867	803	822	744	663
1.99E+00	1.24E+07	715	867	889	767	781	725	695
2.13E+00	1.33E+07	697	886	780	764	726	752	702
2.29E+00	1.43E+07	733	869	725	787	683	646	590
2.46E+00	1.54E+07	651	814	779	661	761	614	638
2.65E+00	1.65E+07	621	723	806	658	685	738	705
2.84E+00	1.77E+07	715	720	666	751	547	524	441
3.05E+00	1.91E+07	463	771	633	597	745	611	703
3.28E+00	2.05E+07	698	796	779	588	542	634	437
3.52E+00	2.20E+07	542	538	590	760	559	456	643
3.79E+00	2.36E+07	511	684	555	388	704	682	378
4.07E+00	2.54E+07	668	789	788	721	379	314	634
4.37E+00	2.73E+07	344	431	357	425	752	752	252
4.70E+00	2.93E+07	689	714	754	616	268	204	716
5.04E+00	3.15E+07	283	579	400	443	762	662	136
5.42E+00	3.38E+07	634	440	612	549	170	311	742
5.82E+00	3.63E+07	316	740	439	309	780	419	197
6.26E+00	3.90E+07	435	271	559	691	145	560	382
6.72E+00	4.19E+07	542	805	329	95	615	114	601
7.22E+00	4.51E+07	121	172	659	824	362	793	42
7.76E+00	4.84E+07	780	715	110	93	206	105	711
8.33E+00	5.20E+07	108	261	834	547	749	347	254
8.95E+00	5.59E+07	362	438	70	438	48	636	83

9.62E+00	6.00E+07	610	552	619	55	559	18	777
1.03E+01	6.45E+07	28	89	371	826	431	544	139
1.11E+01	6.93E+07	466	864	53	126	16	444	19
1.19E+01	7.44E+07	509	47	861	91	729	5	631
1.28E+01	8.00E+07	12	342	83	869	255	268	348
1.38E+01	8.59E+07	275	648	154	35	4	721	2
1.48E+01	9.23E+07	699	11	818	23	523	11	227
1.59E+01	9.92E+07	17	536	25	807	472	32	751
1.71E+01	1.07E+08	37	451	26	169	2	797	20
1.83E+01	1.14E+08	799	4	859	1	131	168	32
1.97E+01	1.23E+08	155	219	113	320	836	2	816
2.12E+01	1.32E+08	2	768	1	673	29	453	150
2.27E+01	1.42E+08	186	10	381	5	3	543	0
2.44E+01	1.52E+08	791	14	615	43	457	0	0
2.62E+01	1.64E+08	17	865	2	920	539	0	1
2.82E+01	1.76E+08	2	116	55	34	0	1	12
3.03E+01	1.89E+08	2	2	907	0	1	4	796
3.25E+01	2.03E+08	43	336	33	1	0	366	191
3.50E+01	2.18E+08	861	658	2	2	28	627	0
3.76E+01	2.34E+08	89	1	0	31	902	2	1
4.04E+01	2.52E+08	1	1	1	912	69	1	145
4.34E+01	2.71E+08	1	1	45	54	0	9	838
4.66E+01	2.91E+08	1	3	930	1	1	851	15
5.00E+01	3.12E+08	413	533	23	1	5	138	0
5.38E+01	3.36E+08	582	461	0	239	818	0	1
5.78E+01	3.61E+08	1	1	1	756	175	1	0
6.21E+01	3.87E+08	0	1	268	3	1	0	176
6.67E+01	4.16E+08	1	4	730	0	0	9	816
7.16E+01	4.47E+08	19	824	0	0	0	884	7
7.70E+01	4.80E+08	809	169	0	1	2	106	0
8.27E+01	5.16E+08	169	0	0	282	724	0	0
8.88E+01	5.54E+08	0	0	2	716	273	0	0
9.54E+01	5.96E+08	1	1	293	0	0	0	0
1.03E+02	6.40E+08	0	17	694	0	0	0	0
1.10E+02	6.87E+08	0	516	10	0	0	0	0
1.18E+02	7.39E+08	0	393	0	0	0	0	0
1.27E+02	7.93E+08	0	72	0	0	0	0	0
1.37E+02	8.52E+08	0	0	0	0	0	0	0
1.47E+02	9.16E+08	0	0	0	0	0	0	88
1.58E+02	9.84E+08	0	0	0	0	0	5	903

1.69E+02	1.06E+09	2	0	0	1	1	820	9
1.82E+02	1.14E+09	631	1	1	0	14	175	0
1.95E+02	1.22E+09	367	0	0	214	961	0	210
2.10E+02	1.31E+09	0	0	1	785	24	0	790
2.26E+02	1.41E+09	0	0	448	0	0	995	0
2.42E+02	1.51E+09	64	240	550	0	22	5	0
2.60E+02	1.63E+09	858	713	0	427	978	0	0
2.80E+02	1.75E+09	77	46	1	573	0	0	0
3.01E+02	1.88E+09	0	1	485	0	0	0	0
3.23E+02	2.02E+09	0	5	514	0	0	0	0
3.47E+02	2.17E+09		983	0	0	0	0	0
3.73E+02	2.33E+09		11	0	0	0	0	0
# Targets hit ---->		456077	500000	500000	500000	500000	500000	500000

Table B6. Electron fluence (electrons / 1000 nm^2) in voxels inside the mesh cylinder by ions of equal stopping power (100 keV um^{-1}). FLUKA data is scaled as electrons-cm^{-2} and described in the 'Bin' column. Un-hit voxels appear in the first row for each ion. The number of hit voxels is summed and listed at the bottom of the table.

Electron fluence	Bin	Be-8 Voxels hit	C-12 Voxels hit	O-16 Voxels hit	Mg-24 Voxels hit	Si-28 Voxels hit	Ca-40 Voxels hit	Ti-48 Voxels hit
1.00E-12	1.00E+00	43928	0	0	0	0	0	0
1.08E-12	1.08E+00	0	0	0	0	0	0	0
1.17E-12	1.17E+00	0	0	0	0	0	0	0
1.27E-12	1.27E+00	0	0	0	0	0	0	0
1.38E-12	1.38E+00	1	0	0	0	0	0	0
1.49E-12	1.49E+00	1	0	0	0	0	0	0
1.62E-12	1.62E+00	0	0	0	0	0	0	0
1.76E-12	1.76E+00	2	0	0	0	0	0	0
1.90E-12	1.90E+00	3	0	0	0	0	0	0
2.06E-12	2.06E+00	0	0	0	0	0	0	0
2.23E-12	2.23E+00	1	0	0	0	0	0	0
2.42E-12	2.42E+00	1	0	0	0	0	0	0
2.62E-12	2.62E+00	1	0	0	0	0	0	0
2.84E-12	2.84E+00	0	0	0	0	0	0	0
3.08E-12	3.08E+00	3	0	0	0	0	0	0
3.34E-12	3.34E+00	1	0	0	0	0	0	0
3.62E-12	3.62E+00	1	0	0	0	0	0	0
3.92E-12	3.92E+00	2	0	0	0	0	0	0
4.25E-12	4.25E+00	3	0	0	0	0	0	0
4.61E-12	4.61E+00	3	0	0	0	0	0	0
4.99E-12	4.99E+00	3	0	0	0	0	0	0
5.41E-12	5.41E+00	3	0	0	0	0	0	0
5.87E-12	5.87E+00	2	0	0	0	0	0	0
6.36E-12	6.36E+00	2	0	0	0	0	0	0
6.89E-12	6.89E+00	4	0	0	0	0	0	0
7.47E-12	7.47E+00	6	0	0	0	0	0	0
8.09E-12	8.09E+00	6	0	0	0	0	0	0
8.77E-12	8.77E+00	3	0	0	0	0	0	0
9.50E-12	9.50E+00	5	0	0	0	0	0	0
1.03E-11	1.03E+01	5	0	0	0	0	0	0
1.12E-11	1.12E+01	4	0	0	0	0	0	0
1.21E-11	1.21E+01	9	0	0	0	0	0	0
1.31E-11	1.31E+01	3	0	0	0	0	0	0
1.42E-11	1.42E+01	8	0	0	0	0	0	0

1.54E-11	1.54E+01	9	0	0	0	0	0	0
1.67E-11	1.67E+01	10	0	0	0	0	0	0
1.81E-11	1.81E+01	7	0	0	0	0	0	0
1.96E-11	1.96E+01	15	0	0	0	0	0	0
2.12E-11	2.12E+01	19	0	0	0	0	0	0
2.30E-11	2.30E+01	11	0	0	0	0	0	0
2.49E-11	2.49E+01	16	0	0	0	0	0	0
2.70E-11	2.70E+01	21	0	0	0	0	0	0
2.93E-11	2.93E+01	23	0	0	0	0	0	0
3.17E-11	3.17E+01	17	0	0	0	0	0	0
3.44E-11	3.44E+01	16	0	0	0	0	0	0
3.73E-11	3.73E+01	20	0	0	0	0	0	0
4.04E-11	4.04E+01	18	0	0	0	0	0	0
4.38E-11	4.38E+01	32	0	0	0	0	0	0
4.75E-11	4.75E+01	18	0	0	0	0	0	0
5.14E-11	5.14E+01	33	0	0	0	0	0	0
5.57E-11	5.57E+01	23	0	0	0	0	0	0
6.04E-11	6.04E+01	29	0	0	0	0	0	0
6.55E-11	6.55E+01	33	0	0	0	0	0	0
7.10E-11	7.10E+01	30	0	0	0	0	0	0
7.69E-11	7.69E+01	31	0	0	0	0	0	0
8.33E-11	8.33E+01	39	0	0	0	0	0	0
9.03E-11	9.03E+01	40	0	0	0	0	0	0
9.79E-11	9.79E+01	42	0	0	0	0	0	0
1.06E-10	1.06E+02	40	0	0	0	0	0	0
1.15E-10	1.15E+02	58	0	0	0	0	0	0
1.25E-10	1.25E+02	52	0	0	0	0	0	0
1.35E-10	1.35E+02	66	0	0	0	0	0	0
1.46E-10	1.46E+02	81	0	0	0	0	0	0
1.59E-10	1.59E+02	83	0	0	0	0	0	0
1.72E-10	1.72E+02	88	0	0	0	0	0	0
1.86E-10	1.86E+02	96	0	0	0	0	0	0
2.02E-10	2.02E+02	107	0	0	0	0	0	0
2.19E-10	2.19E+02	115	0	0	0	0	0	0
2.37E-10	2.37E+02	112	0	0	0	0	0	0
2.57E-10	2.57E+02	153	0	0	0	0	0	0
2.78E-10	2.78E+02	149	0	0	0	0	0	0
3.02E-10	3.02E+02	175	0	0	0	0	0	0
3.27E-10	3.27E+02	155	0	0	0	0	0	0
3.54E-10	3.54E+02	192	0	0	0	0	0	0

3.84E-10	3.84E+02	171	0	0	0	0	0	0
4.16E-10	4.16E+02	200	0	0	0	0	0	0
4.51E-10	4.51E+02	241	0	0	0	0	0	0
4.89E-10	4.89E+02	259	0	0	0	0	0	0
5.30E-10	5.30E+02	288	0	0	0	0	0	0
5.74E-10	5.74E+02	315	0	0	0	0	0	0
6.22E-10	6.22E+02	343	0	0	0	0	0	0
6.74E-10	6.74E+02	342	0	0	0	0	0	0
7.31E-10	7.31E+02	375	0	0	0	0	0	0
7.92E-10	7.92E+02	417	0	0	0	0	0	0
8.58E-10	8.58E+02	475	0	0	0	0	0	0
9.30E-10	9.30E+02	521	0	0	0	0	0	0
1.01E-09	1.01E+03	528	0	0	0	0	0	0
1.09E-09	1.09E+03	624	0	0	0	0	0	0
1.18E-09	1.18E+03	693	0	0	0	0	0	0
1.28E-09	1.28E+03	723	0	0	0	0	0	0
1.39E-09	1.39E+03	809	0	0	0	0	0	0
1.51E-09	1.51E+03	869	0	0	0	0	0	0
1.63E-09	1.63E+03	1017	0	0	0	0	0	0
1.77E-09	1.77E+03	1521	0	0	0	0	0	0
1.92E-09	1.92E+03	2893	0	0	0	0	0	0
2.08E-09	2.08E+03	3536	0	0	0	0	0	0
2.25E-09	2.25E+03	3312	0	0	0	0	0	0
2.44E-09	2.44E+03	2697	0	0	0	0	0	0
2.65E-09	2.65E+03	2330	0	0	0	0	0	0
2.87E-09	2.87E+03	1980	0	0	0	0	0	0
3.11E-09	3.11E+03	1853	0	0	0	0	0	0
3.37E-09	3.37E+03	1886	0	0	0	0	0	0
3.65E-09	3.65E+03	1931	0	0	0	0	0	0
3.95E-09	3.95E+03	2240	0	0	0	0	0	0
4.29E-09	4.29E+03	2652	0	0	0	0	0	0
4.65E-09	4.65E+03	2818	0	0	0	0	0	0
5.03E-09	5.03E+03	2562	0	0	0	0	0	0
5.46E-09	5.46E+03	2447	0	0	0	0	0	0
5.91E-09	5.91E+03	2430	0	0	0	0	0	0
6.41E-09	6.41E+03	2493	0	0	0	0	0	0
6.94E-09	6.94E+03	2654	0	0	0	0	0	0
7.53E-09	7.53E+03	2694	0	0	0	0	0	0
8.16E-09	8.16E+03	2603	0	0	0	0	0	0
8.84E-09	8.84E+03	2677	0	0	0	0	0	0

9.58E-09	9.58E+03	2702	0	0	0	0	0	0
1.04E-08	1.04E+04	2713	0	0	0	0	0	0
1.13E-08	1.13E+04	2745	0	0	0	0	0	0
1.22E-08	1.22E+04	2856	0	0	0	0	0	0
1.32E-08	1.32E+04	2787	0	0	0	0	0	0
1.43E-08	1.43E+04	2962	0	0	0	0	0	0
1.55E-08	1.55E+04	2873	0	0	0	0	0	0
1.68E-08	1.68E+04	2925	0	0	0	0	0	0
1.82E-08	1.82E+04	3002	0	0	0	0	0	0
1.98E-08	1.98E+04	3015	0	0	0	0	0	0
2.14E-08	2.14E+04	3075	0	0	0	0	0	0
2.32E-08	2.32E+04	3102	0	0	0	0	0	0
2.51E-08	2.51E+04	3060	0	0	0	0	0	0
2.72E-08	2.72E+04	3181	0	0	0	0	0	0
2.95E-08	2.95E+04	3264	0	0	0	0	0	0
3.20E-08	3.20E+04	3203	0	0	0	0	0	0
3.47E-08	3.47E+04	3207	0	0	0	0	0	0
3.76E-08	3.76E+04	3118	0	0	0	0	0	0
4.07E-08	4.07E+04	3155	0	0	0	0	0	0
4.41E-08	4.41E+04	3083	2	0	0	0	0	0
4.78E-08	4.78E+04	3237	4	0	0	0	0	0
5.18E-08	5.18E+04	3250	8	0	0	0	0	0
5.62E-08	5.62E+04	3240	15	0	0	0	0	0
6.09E-08	6.09E+04	3294	35	0	0	0	0	0
6.60E-08	6.60E+04	3422	79	0	0	0	0	0
7.15E-08	7.15E+04	3474	110	0	0	0	0	0
7.75E-08	7.75E+04	3421	187	0	0	0	0	0
8.40E-08	8.40E+04	3556	265	1	0	0	0	0
9.10E-08	9.10E+04	3523	374	1	0	0	0	0
9.86E-08	9.86E+04	3793	485	1	0	0	0	0
1.07E-07	1.07E+05	3621	657	14	0	0	0	0
1.16E-07	1.16E+05	3513	810	23	0	0	0	0
1.26E-07	1.26E+05	3578	1026	81	0	0	0	0
1.36E-07	1.36E+05	3599	1158	144	0	0	0	0
1.47E-07	1.47E+05	3629	1450	245	1	0	0	0
1.60E-07	1.60E+05	3764	1710	379	0	1	0	0
1.73E-07	1.73E+05	3734	1873	539	11	0	0	1
1.88E-07	1.88E+05	3824	1911	825	38	0	0	1
2.03E-07	2.03E+05	3873	2167	940	96	24	0	7
2.20E-07	2.20E+05	3681	2289	1097	183	59	3	10

2.39E-07	2.39E+05	3651	2316	1331	299	115	33	33
2.59E-07	2.59E+05	3787	2568	1515	413	200	55	63
2.81E-07	2.81E+05	3778	2653	1809	566	323	125	130
3.04E-07	3.04E+05	3842	2862	1818	759	531	186	241
3.30E-07	3.30E+05	3937	3200	1979	1096	690	303	382
3.57E-07	3.57E+05	3988	3383	2113	1223	855	510	542
3.87E-07	3.87E+05	4001	3737	2479	1406	1100	608	741
4.19E-07	4.19E+05	3930	3602	2896	1686	1283	821	911
4.55E-07	4.55E+05	3958	3896	2929	1873	1521	1081	1050
4.93E-07	4.93E+05	4027	4227	2949	2151	1821	1284	1145
5.34E-07	5.34E+05	3881	4507	3316	2334	2139	1429	1423
5.79E-07	5.79E+05	3860	4939	3561	2552	2307	1762	1664
6.27E-07	6.27E+05	4084	5611	3813	2781	2351	2061	2009
6.80E-07	6.80E+05	4045	6282	4111	2970	2664	2091	2263
7.37E-07	7.37E+05	3876	6885	4362	3350	3028	2372	2655
7.98E-07	7.98E+05	3777	7947	4612	3416	3247	2749	3085
8.65E-07	8.65E+05	3940	9126	5081	3702	3461	3275	3505
9.37E-07	9.37E+05	3924	10484	5868	4254	3974	3801	4087
1.02E-06	1.02E+06	3993	11055	6593	4789	4490	4333	5356
1.10E-06	1.10E+06	3949	11126	7504	5567	5227	5396	8651
1.19E-06	1.19E+06	3764	10467	8928	6578	6273	8323	16827
1.29E-06	1.29E+06	3879	10365	10901	8400	8559	15235	19387
1.40E-06	1.40E+06	4029	10388	12508	11615	13073	19054	18655
1.52E-06	1.52E+06	3841	10147	12484	15214	16787	18623	18728
1.65E-06	1.65E+06	3843	9808	12176	15809	16783	17759	17642
1.78E-06	1.78E+06	3836	9356	11900	15460	16772	17183	16974
1.93E-06	1.93E+06	3747	9440	11823	14771	15666	17376	15891
2.10E-06	2.10E+06	3817	9115	11703	15388	15838	16124	15451
2.27E-06	2.27E+06	3575	9148	11797	14285	15125	15374	15121
2.46E-06	2.46E+06	3867	8920	11208	14050	14135	14790	14153
2.67E-06	2.67E+06	3719	8685	10828	13504	14138	14131	13783
2.89E-06	2.89E+06	3643	8515	10918	13013	13418	13353	13090
3.13E-06	3.13E+06	3652	8261	10642	12716	13067	13132	12388
3.39E-06	3.39E+06	3659	8300	10429	12117	12237	12466	12059
3.68E-06	3.68E+06	3544	7917	10194	11784	12148	11986	11647
3.99E-06	3.99E+06	3396	7871	9977	11521	11536	11455	10932
4.32E-06	4.32E+06	3493	7660	9560	10961	11328	10871	10276
4.68E-06	4.68E+06	3390	7563	9329	10696	10662	10371	10022
5.07E-06	5.07E+06	3241	7364	9048	10288	10291	9925	9401
5.50E-06	5.50E+06	3326	6963	9126	9741	9804	9655	9108

5.96E-06	5.96E+06	3272	7002	8563	9166	9327	8992	8671
6.46E-06	6.46E+06	3143	6903	8184	9018	8936	8513	8276
7.00E-06	7.00E+06	3157	6620	8189	8448	8582	8316	7788
7.59E-06	7.59E+06	3088	6512	7827	8261	8044	7736	7420
8.22E-06	8.22E+06	3009	6315	7675	7946	7870	7522	7088
8.91E-06	8.91E+06	2954	6251	7266	7487	7391	7075	6814
9.65E-06	9.65E+06	2811	5990	7118	7191	7152	6722	6306
1.05E-05	1.05E+07	2818	5850	6776	6885	6973	6496	6146
1.13E-05	1.13E+07	2788	5826	6578	6600	6505	6206	5905
1.23E-05	1.23E+07	2757	5565	6297	6273	6274	5861	5603
1.33E-05	1.33E+07	2635	5423	6030	6165	5851	5650	5278
1.44E-05	1.44E+07	2597	5231	5810	5810	5732	5355	5056
1.56E-05	1.56E+07	2504	5016	5535	5540	5420	5076	4773
1.70E-05	1.70E+07	2438	4947	5410	5187	5213	4855	4614
1.84E-05	1.84E+07	2453	4758	5197	5033	4855	4604	4379
1.99E-05	1.99E+07	2288	4615	4903	4768	4713	4381	4120
2.16E-05	2.16E+07	2263	4518	4743	4580	4453	4213	4018
2.34E-05	2.34E+07	2264	4219	4610	4404	4189	3981	3778
2.53E-05	2.53E+07	2205	4213	4321	4166	4096	3778	3581
2.75E-05	2.75E+07	2082	3901	4227	4022	3954	3607	3432
2.98E-05	2.98E+07	2103	3882	3973	3803	3643	3493	3245
3.23E-05	3.23E+07	1977	3667	3848	3605	3543	3334	3118
3.50E-05	3.50E+07	2013	3568	3639	3417	3374	3085	2924
3.79E-05	3.79E+07	1905	3456	3482	3287	3191	2989	2821
4.11E-05	4.11E+07	1827	3284	3373	3130	3060	2821	2657
4.45E-05	4.45E+07	1822	3210	3170	3007	2930	2673	2541
4.82E-05	4.82E+07	1760	3067	3089	2819	2726	2540	2398
5.23E-05	5.23E+07	1644	2885	2894	2738	2682	2458	2319
5.66E-05	5.66E+07	1699	2810	2799	2604	2467	2291	2164
6.14E-05	6.14E+07	1569	2696	2622	2406	2371	2190	2072
6.65E-05	6.65E+07	1560	2574	2535	2367	2288	2092	1940
7.21E-05	7.21E+07	1487	2491	2402	2187	2150	1959	1890
7.81E-05	7.81E+07	1518	2365	2286	2101	2035	1899	1805
8.47E-05	8.47E+07	1353	2255	2196	2028	1966	1800	1692
9.18E-05	9.18E+07	1418	2157	2097	1908	1860	1725	1662
9.94E-05	9.94E+07	1301	2087	1997	1783	1745	1600	1452
1.08E-04	1.08E+08	1264	1955	1887	1727	1708	1628	1547
1.17E-04	1.17E+08	1315	1897	1753	1696	1633	1389	1318
1.27E-04	1.27E+08	1149	1801	1750	1500	1447	1484	1292
1.37E-04	1.37E+08	1085	1708	1633	1581	1560	1247	1382

1.49E-04	1.49E+08	1051	1666	1510	1293	1238	1226	1200
1.61E-04	1.61E+08	1084	1527	1599	1506	1365	1348	1070
1.75E-04	1.75E+08	1024	1546	1274	1220	1387	1198	1019
1.89E-04	1.89E+08	1029	1389	1505	1091	1116	1110	1008
2.05E-04	2.05E+08	950	1416	1211	1168	1023	1030	978
2.22E-04	2.22E+08	835	1185	1106	1192	1006	1005	984
2.41E-04	2.41E+08	865	1311	1154	1126	1013	983	987
2.61E-04	2.61E+08	888	1275	1239	1039	968	939	963
2.83E-04	2.83E+08	932	1123	1098	909	977	780	758
3.07E-04	3.07E+08	929	1005	1014	786	986	502	403
3.32E-04	3.32E+08	669	977	938	745	991	809	872
3.60E-04	3.60E+08	443	990	774	899	887	985	979
3.90E-04	3.90E+08	883	968	693	988	353	757	171
4.23E-04	4.23E+08	875	963	878	926	756	249	843
4.58E-04	4.58E+08	173	927	969	213	989	992	853
4.97E-04	4.97E+08	903	612	967	852	334	294	147
5.38E-04	5.38E+08	391	518	235	960	669	705	973
5.83E-04	5.83E+08	606	916	784	47	958	737	27
6.32E-04	6.32E+08	668	950	983	983	42	260	988
6.85E-04	6.85E+08	320	135	34	100	991	834	9
7.42E-04	7.42E+08	641	886	966	898	6	164	953
8.05E-04	8.05E+08	339	811	211	153	992	576	45
8.72E-04	8.72E+08	260	188	786	844	3	422	280
9.45E-04	9.45E+08	725	974	300	37	992	15	718
1.02E-03	1.02E+09	33	19	694	960	5	983	1
1.11E-03	1.11E+09	956	974	105	4	657	1	784
1.20E-03	1.20E+09	8	16	891	990	339	198	213
1.30E-03	1.30E+09	59	956	6	5	2	799	2
1.41E-03	1.41E+09	926	33	990	6	970	2	103
1.53E-03	1.53E+09	5	218	2	992	28	1	895
1.66E-03	1.66E+09	17	771	11	0	0	997	0
1.80E-03	1.80E+09	967	7	985	2	355	0	0
1.95E-03	1.95E+09	7	828	1	992	643	1	23
2.11E-03	2.11E+09	3	162	3	4	0	0	977
2.29E-03	2.29E+09	14	4	995	2	1	998	0
2.48E-03	2.48E+09	967	80	0	1	214	1	0
2.69E-03	2.69E+09	14	913	1	961	785	0	0
2.91E-03	2.91E+09	0	1	1	36	0	0	302
3.16E-03	3.16E+09	2	2	993	0	0	4	697
3.42E-03	3.42E+09	12	25	3	0	0	994	0

3.71E-03	3.71E+09	981	970	0	1	638	1	0
4.02E-03	4.02E+09	2	1	1	998	361	0	0
4.35E-03	4.35E+09	0	0	1	0	0	0	0
4.72E-03	4.72E+09	0	2	997	0	0	0	1
5.11E-03	5.11E+09	1	242	0	0	0	1	0
5.54E-03	5.54E+09	0	755	1	1	1	0	977
6.01E-03	6.01E+09	1	0	0	0	0	525	22
6.51E-03	6.51E+09	183	0	0	0	0	474	0
7.05E-03	7.05E+09	814	0	0	6	999	0	0
7.65E-03	7.65E+09	0	0	0	993	0	0	0
8.29E-03	8.29E+09	0	0	57	0	0	0	0
8.98E-03	8.98E+09	0	1	942	0	0	0	0
9.73E-03	9.73E+09	0	794	0	0	0	0	0
1.05E-02	1.05E+10	0	204	0	0	0	0	0
1.14E-02	1.14E+10	0	0	0	0	0	0	0
1.24E-02	1.24E+10	0	0	0	0	0	0	0
1.34E-02	1.34E+10	0	0	0	0	0	0	0
1.45E-02	1.45E+10	1	0	0	0	0	0	0
1.58E-02	1.58E+10	0	0	0	0	0	0	0
1.71E-02	1.71E+10	0	0	0	0	0	0	974
1.85E-02	1.85E+10	0	0	0	0	0	538	26
2.01E-02	2.01E+10	5	0	0	0	0	462	0
2.17E-02	2.17E+10	994	0	0	13	997	0	0
2.36E-02	2.36E+10	0	1	1	987	3	0	0
2.55E-02	2.55E+10	0	0	343	0	0	0	0
2.77E-02	2.77E+10	0	197	656	0	0	0	0
3.00E-02	3.00E+10	0	802	0	0	0	0	0
3.25E-02	3.25E+10		0	0	0	0	0	0
# Targets hit ---->		456072	500000	500000	500000	500000	500000	500000

Table B7. Dose per electron fluence (Gy / electrons-1000 nm^3) in voxels inside the cylinder mesh geometry by ions of equal stopping power (100 keV um^{-1}). FLUKA data are presented as (GeV/cm^3 per electron/cm^2) in the 'Bin' column. Un-hit voxels appear in the first row for each ion. The number of hit voxels is summed and listed at the bottom of the table.

Dose / Electron	Bin	Be-8 Voxels hit	C-12 Voxels hit	O-16 Voxels hit	Mg-24 Voxels hit	Si-28 Voxels hit	Ca-40 Voxels hit	Ti-48 Voxels hit
1.60E+02	1.00E-03	0	0	0	0	0	0	0
1.65E+02	1.03E-03	0	0	0	0	0	0	0
1.69E+02	1.06E-03	0	0	0	0	0	0	0
1.74E+02	1.09E-03	0	0	0	0	0	0	0
1.79E+02	1.12E-03	0	0	0	0	0	0	0
1.84E+02	1.15E-03	0	0	0	0	0	0	0
1.89E+02	1.18E-03	0	0	0	0	0	0	0
1.94E+02	1.21E-03	0	0	0	0	0	0	0
1.99E+02	1.24E-03	0	0	0	0	0	0	0
2.05E+02	1.28E-03	0	0	0	0	0	0	0
2.11E+02	1.32E-03	0	0	0	0	0	0	0
2.17E+02	1.35E-03	0	0	0	0	0	0	0
2.23E+02	1.39E-03	0	0	0	0	0	0	0
2.29E+02	1.43E-03	0	0	0	0	0	0	0
2.35E+02	1.47E-03	0	0	0	0	0	0	0
2.42E+02	1.51E-03	0	0	0	0	0	0	0
2.48E+02	1.55E-03	0	0	0	0	0	0	0
2.55E+02	1.59E-03	0	0	0	0	0	0	0
2.62E+02	1.64E-03	0	0	0	0	0	0	0
2.70E+02	1.68E-03	0	0	0	0	0	0	0
2.77E+02	1.73E-03	0	0	0	0	0	0	0
2.85E+02	1.78E-03	0	0	0	0	0	0	0
2.93E+02	1.83E-03	0	0	0	0	0	0	0
3.01E+02	1.88E-03	0	0	0	0	0	0	0
3.09E+02	1.93E-03	0	0	0	0	0	0	0
3.18E+02	1.98E-03	0	0	0	0	0	0	0
3.27E+02	2.04E-03	0	0	0	0	0	0	0
3.36E+02	2.09E-03	0	0	0	0	0	0	0
3.45E+02	2.15E-03	0	0	0	0	0	0	0
3.55E+02	2.21E-03	0	0	0	0	0	0	0
3.64E+02	2.27E-03	0	0	0	0	0	0	0
3.74E+02	2.34E-03	0	0	0	0	0	0	0
3.85E+02	2.40E-03	0	0	0	0	0	0	0

3.96E+02	2.47E-03	0	0	0	0	0	0	0
4.07E+02	2.54E-03	0	0	0	0	0	0	0
4.18E+02	2.61E-03	0	0	0	0	0	0	0
4.29E+02	2.68E-03	0	0	0	0	0	0	0
4.41E+02	2.75E-03	0	0	0	0	0	0	0
4.54E+02	2.83E-03	0	0	0	0	0	0	0
4.66E+02	2.91E-03	0	0	0	0	0	0	0
4.79E+02	2.99E-03	0	0	0	0	0	0	0
4.92E+02	3.07E-03	0	0	0	0	0	0	0
5.06E+02	3.16E-03	0	0	0	0	0	0	0
5.20E+02	3.25E-03	0	0	0	0	0	0	0
5.35E+02	3.34E-03	0	0	0	0	0	0	0
5.49E+02	3.43E-03	0	0	0	0	0	0	0
5.65E+02	3.52E-03	0	0	0	0	0	0	0
5.80E+02	3.62E-03	0	0	0	0	0	0	0
5.97E+02	3.72E-03	0	0	0	0	0	0	0
6.13E+02	3.83E-03	0	0	0	0	0	0	0
6.30E+02	3.93E-03	0	0	0	0	0	0	0
6.48E+02	4.04E-03	0	0	0	0	0	0	0
6.66E+02	4.15E-03	0	0	0	0	0	0	0
6.84E+02	4.27E-03	0	0	0	0	0	0	0
7.03E+02	4.39E-03	0	0	0	0	0	0	0
7.23E+02	4.51E-03	0	0	0	0	0	0	0
7.43E+02	4.64E-03	0	0	0	0	0	0	0
7.63E+02	4.76E-03	0	0	0	0	0	0	0
7.84E+02	4.90E-03	0	0	0	0	0	0	0
8.06E+02	5.03E-03	0	0	0	0	0	0	0
8.29E+02	5.17E-03	0	0	0	0	0	0	0
8.52E+02	5.32E-03	0	0	0	0	0	0	0
8.75E+02	5.46E-03	0	0	0	0	0	0	0
9.00E+02	5.61E-03	0	0	0	0	0	0	0
9.25E+02	5.77E-03	0	0	0	0	0	0	0
9.50E+02	5.93E-03	0	0	0	0	0	0	0
9.77E+02	6.10E-03	0	0	0	0	0	0	0
1.00E+03	6.26E-03	0	0	0	0	0	0	0
1.03E+03	6.44E-03	0	0	0	0	0	0	0
1.06E+03	6.62E-03	0	0	0	0	0	0	0
1.09E+03	6.80E-03	5	0	0	0	0	0	0
1.12E+03	6.99E-03	1	0	0	0	0	0	0
1.15E+03	7.18E-03	0	0	0	0	0	0	0

1.18E+03	7.38E-03	0	0	0	0	0	0	0
1.22E+03	7.59E-03	0	0	0	0	0	0	0
1.25E+03	7.80E-03	8	0	0	0	0	0	0
1.28E+03	8.02E-03	5	0	0	0	0	0	0
1.32E+03	8.24E-03	3	0	0	0	0	0	0
1.36E+03	8.47E-03	0	0	0	0	0	0	0
1.39E+03	8.70E-03	5	0	0	0	0	0	0
1.43E+03	8.94E-03	21	0	0	0	0	0	0
1.47E+03	9.19E-03	17	0	0	0	0	0	0
1.51E+03	9.45E-03	2	0	0	0	0	0	0
1.56E+03	9.71E-03	1	0	0	0	0	0	0
1.60E+03	9.98E-03	1	0	0	0	0	0	0
1.64E+03	1.03E-02	1	0	0	0	0	0	0
1.69E+03	1.05E-02	1	0	0	0	0	0	0
1.74E+03	1.08E-02	30	0	0	0	0	0	0
1.78E+03	1.11E-02	21	0	0	0	0	0	4
1.83E+03	1.14E-02	6	0	0	0	0	1	3
1.88E+03	1.18E-02	58	0	0	0	0	7	41
1.94E+03	1.21E-02	41	0	0	1	4	49	114
1.99E+03	1.24E-02	34	0	0	4	30	212	400
2.05E+03	1.28E-02	11	0	0	50	131	578	1041
2.10E+03	1.31E-02	15	0	0	179	366	1319	2061
2.16E+03	1.35E-02	72	0	0	534	994	2442	3294
2.22E+03	1.39E-02	40	0	1	1143	1767	3974	4966
2.28E+03	1.42E-02	105	0	9	2212	3292	5676	7099
2.35E+03	1.46E-02	49	0	60	3600	4992	7810	9088
2.41E+03	1.50E-02	90	0	145	5324	6836	9894	11136
2.48E+03	1.55E-02	76	0	465	7212	9121	12260	13139
2.55E+03	1.59E-02	78	0	1083	9756	11311	14123	14989
2.62E+03	1.63E-02	239	1	2138	11795	13467	15916	16511
2.69E+03	1.68E-02	168	0	3639	13853	15274	17341	17614
2.76E+03	1.73E-02	86	0	5830	15761	17011	18421	18372
2.84E+03	1.77E-02	158	2	8238	17346	18293	19030	18717
2.92E+03	1.82E-02	190	26	10984	18268	19128	19153	19045
3.00E+03	1.87E-02	232	130	13752	19099	19843	19559	18939
3.09E+03	1.93E-02	185	457	16197	19576	19707	19413	18546
3.17E+03	1.98E-02	226	1113	18473	19970	19644	18528	18086
3.26E+03	2.03E-02	273	2386	19868	19698	19280	18130	17421
3.35E+03	2.09E-02	314	4334	21154	19503	18622	17076	16582
3.44E+03	2.15E-02	322	7075	21807	18691	18081	16293	15698

3.54E+03	2.21E-02	353	10665	22465	17842	16981	15529	14975
3.64E+03	2.27E-02	357	14529	22027	16812	16057	14572	14043
3.74E+03	2.33E-02	368	19160	21883	16438	15426	13813	13285
3.84E+03	2.40E-02	628	23206	21021	15678	14456	12672	12057
3.95E+03	2.46E-02	589	26432	20212	14427	13530	12116	11590
4.06E+03	2.53E-02	797	28807	18928	13776	12878	11185	10871
4.17E+03	2.60E-02	883	29944	17819	12957	12069	10392	10184
4.29E+03	2.67E-02	930	29233	16219	12050	10882	9660	9585
4.40E+03	2.75E-02	1188	27545	15017	11262	10359	9243	8903
4.53E+03	2.83E-02	1370	25765	14216	10286	9545	8523	8301
4.65E+03	2.90E-02	1297	23377	13121	9596	8934	7948	7719
4.78E+03	2.98E-02	1605	20990	12376	8868	8181	7413	7250
4.91E+03	3.07E-02	1841	19046	11373	8221	7650	6980	6511
5.05E+03	3.15E-02	2132	17074	10541	7489	6967	6540	6161
5.19E+03	3.24E-02	2389	15604	9734	7012	6442	6008	5849
5.34E+03	3.33E-02	2999	13980	8750	6424	5941	5536	5487
5.48E+03	3.42E-02	3477	12740	8108	5797	5538	5136	5226
5.64E+03	3.52E-02	4080	11592	7191	5438	5343	4984	5043
5.79E+03	3.62E-02	5049	10582	6636	4975	4746	4671	4692
5.95E+03	3.72E-02	6328	9765	6086	4537	4546	4248	4139
6.12E+03	3.82E-02	7880	8552	5483	4262	4191	4045	3818
6.29E+03	3.92E-02	9774	7711	4972	3988	3885	3757	3528
6.46E+03	4.03E-02	11775	6876	4455	3694	3481	3463	3510
6.64E+03	4.15E-02	13726	6304	3944	3272	3292	3103	3232
6.83E+03	4.26E-02	16276	5519	3639	2985	2946	2900	2969
7.02E+03	4.38E-02	18922	4898	3323	2882	2887	2743	2735
7.21E+03	4.50E-02	22143	4472	3115	2678	2712	2635	2651
7.41E+03	4.63E-02	25058	4085	2860	2592	2514	2476	2466
7.62E+03	4.75E-02	27720	3578	2576	2296	2410	2376	2354
7.83E+03	4.89E-02	29202	3308	2473	2122	2145	2199	2225
8.05E+03	5.02E-02	28076	2911	2141	2115	2108	2115	2070
8.27E+03	5.16E-02	25667	2612	2128	1984	2035	1991	2023
8.50E+03	5.30E-02	21907	2494	1941	1828	1827	1842	1783
8.73E+03	5.45E-02	18293	2152	1787	1739	1759	1682	1659
8.98E+03	5.60E-02	15310	1916	1680	1676	1618	1589	1617
9.23E+03	5.76E-02	12989	1819	1540	1577	1459	1519	1560
9.48E+03	5.92E-02	10949	1607	1380	1388	1441	1443	1371
9.75E+03	6.08E-02	9529	1482	1308	1343	1352	1345	1306
1.00E+04	6.25E-02	8372	1395	1261	1244	1253	1261	1244
1.03E+04	6.43E-02	7215	1275	1207	1182	1195	1195	1199

1.06E+04	6.60E-02	6350	1214	1071	1103	1089	1137	1160
1.09E+04	6.79E-02	5668	1139	1073	1049	1075	1047	989
1.12E+04	6.98E-02	5115	1037	984	1043	955	1046	1020
1.15E+04	7.17E-02	4598	978	912	899	950	906	984
1.18E+04	7.37E-02	4254	1470	1662	1556	1615	1433	1427
1.21E+04	7.57E-02	4100	1043	1037	1180	1162	1287	1276
1.25E+04	7.78E-02	3664	906	732	769	759	819	772
1.28E+04	8.00E-02	3077	748	687	687	717	677	731
1.32E+04	8.22E-02	2752	751	701	713	671	703	709
1.35E+04	8.45E-02	2486	666	629	660	695	692	647
1.39E+04	8.68E-02	2279	609	655	646	612	634	635
1.43E+04	8.93E-02	2034	641	622	617	630	616	647
1.47E+04	9.17E-02	1921	605	645	608	654	669	617
1.51E+04	9.43E-02	1854	479	507	580	589	605	584
1.55E+04	9.69E-02	1587	414	371	487	479	501	501
1.60E+04	9.96E-02	1428	505	502	381	452	385	395
1.64E+04	1.02E-01	1338	445	432	528	492	481	489
1.69E+04	1.05E-01	1415	822	691	480	506	496	526
1.73E+04	1.08E-01	1410	724	906	882	651	789	791
1.78E+04	1.11E-01	1224	214	351	702	642	758	742
1.83E+04	1.14E-01	795	20	30	110	378	242	225
1.88E+04	1.17E-01	641	13	3	5	43	18	26
1.93E+04	1.21E-01	849	60	9	0	18	3	7
1.99E+04	1.24E-01	984	601	220	61	197	49	47
2.04E+04	1.27E-01	847	1075	1014	603	527	429	434
2.10E+04	1.31E-01	1371	592	921	1099	599	1104	1028
2.16E+04	1.35E-01	1136	280	476	789	578	848	922
2.22E+04	1.38E-01	494	212	299	400	604	487	473
2.28E+04	1.42E-01	366	156	69	48	429	79	92
2.34E+04	1.46E-01	304	65	1	2	52	5	4
2.41E+04	1.50E-01	294	73	3	0	0	0	1
2.47E+04	1.54E-01	271	100	0	1	2	0	0
2.54E+04	1.59E-01	275	110	4	1	1	2	2
2.61E+04	1.63E-01	268	147	104	3	2	2	1
2.68E+04	1.68E-01	399	254	326	65	4	30	36
2.76E+04	1.72E-01	684	269	446	514	216	362	351
2.84E+04	1.77E-01	561	31	120	401	591	523	509
2.91E+04	1.82E-01	297	0	2	20	187	82	99
3.00E+04	1.87E-01	170	1	1	0	1	0	3
3.08E+04	1.92E-01	179	2	1	0	0	0	0

3.16E+04	1.97E-01	189	0	0	0	0	1	0
3.25E+04	2.03E-01	174	1	0	0	0	0	1
3.34E+04	2.09E-01	153	0	1	1	1	0	0
3.44E+04	2.14E-01	126	0	1	0	0	0	0
3.53E+04	2.20E-01	122	0	0	0	0	0	0
3.63E+04	2.26E-01	130	2	0	0	0	0	0
3.73E+04	2.33E-01	96	0	0	0	0	0	0
3.83E+04	2.39E-01	102	0	0	0	0	0	0
3.94E+04	2.46E-01	109	0	0	0	0	0	0
4.05E+04	2.53E-01	106	0	0	0	0	0	0
4.16E+04	2.60E-01	100	0	0	0	0	0	0
4.28E+04	2.67E-01	85	0	0	0	0	0	0
4.40E+04	2.74E-01	89	0	0	0	0	0	0
4.52E+04	2.82E-01	66	0	0	0	0	0	0
4.64E+04	2.90E-01	78	0	0	0	0	0	0
4.77E+04	2.98E-01	81	0	0	0	0	0	0
4.90E+04	3.06E-01	65	0	0	0	0	0	0
5.04E+04	3.15E-01	64	0	0	0	0	0	0
5.18E+04	3.23E-01	49	0	0	0	0	0	0
5.32E+04	3.32E-01	46	0	0	0	0	0	0
5.47E+04	3.42E-01	54	0	0	0	0	0	0
5.62E+04	3.51E-01	52	0	0	0	0	0	0
5.78E+04	3.61E-01	61	0	0	0	0	0	0
5.94E+04	3.71E-01	55	0	0	0	0	0	0
6.11E+04	3.81E-01	51	0	0	0	0	0	0
6.27E+04	3.92E-01	54	0	0	0	0	0	0
6.45E+04	4.03E-01	49	0	0	0	0	0	0
6.63E+04	4.14E-01	49	0	0	0	0	0	0
6.81E+04	4.25E-01	41	0	0	0	0	0	0
7.00E+04	4.37E-01	41	0	0	0	0	0	0
7.20E+04	4.49E-01	40	0	0	0	0	0	0
7.40E+04	4.62E-01	40	0	0	0	0	0	0
7.60E+04	4.74E-01	33	0	0	0	0	0	0
7.81E+04	4.88E-01	49	0	0	0	0	0	0
8.03E+04	5.01E-01	30	0	0	0	0	0	0
8.25E+04	5.15E-01	33	0	0	0	0	0	0
8.48E+04	5.29E-01	35	0	0	0	0	0	0
8.72E+04	5.44E-01	29	0	0	0	0	0	0
8.96E+04	5.59E-01	35	0	0	0	0	0	0
9.21E+04	5.75E-01	21	0	0	0	0	0	0

9.46E+04	5.91E-01	22	0	0	0	0	0	0
9.73E+04	6.07E-01	28	0	0	0	0	0	0
1.00E+05	6.24E-01	33	0	0	0	0	0	0
1.03E+05	6.41E-01	22	0	0	0	0	0	0
1.06E+05	6.59E-01	20	0	0	0	0	0	0
1.09E+05	6.77E-01	20	0	0	0	0	0	0
1.12E+05	6.96E-01	20	0	0	0	0	0	0
1.15E+05	7.15E-01	20	0	0	0	0	0	0
1.18E+05	7.35E-01	23	0	0	0	0	0	0
1.21E+05	7.56E-01	22	0	0	0	0	0	0
1.24E+05	7.77E-01	26	0	0	0	0	0	0
1.28E+05	7.98E-01	15	0	0	0	0	0	0
1.31E+05	8.20E-01	15	0	0	0	0	0	0
1.35E+05	8.43E-01	15	0	0	0	0	0	0
1.39E+05	8.67E-01	10	0	0	0	0	0	0
1.43E+05	8.91E-01	14	0	0	0	0	0	0
1.47E+05	9.15E-01	12	0	0	0	0	0	0
1.51E+05	9.41E-01	13	0	0	0	0	0	0
1.55E+05	9.67E-01	17	0	0	0	0	0	0
1.59E+05	9.94E-01	10	0	0	0	0	0	0
1.64E+05	1.02E+00	18	0	0	0	0	0	0
1.68E+05	1.05E+00	19	0	0	0	0	0	0
1.73E+05	1.08E+00	11	0	0	0	0	0	0
1.78E+05	1.11E+00	11	0	0	0	0	0	0
1.83E+05	1.14E+00	8	0	0	0	0	0	0
1.88E+05	1.17E+00	14	0	0	0	0	0	0
1.93E+05	1.20E+00	11	0	0	0	0	0	0
1.98E+05	1.24E+00	8	0	0	0	0	0	0
2.04E+05	1.27E+00	14	0	0	0	0	0	0
2.09E+05	1.31E+00	15	0	0	0	0	0	0
2.15E+05	1.34E+00	8	0	0	0	0	0	0
2.21E+05	1.38E+00	9	0	0	0	0	0	0
2.27E+05	1.42E+00	4	0	0	0	0	0	0
2.34E+05	1.46E+00	5	0	0	0	0	0	0
2.40E+05	1.50E+00	6	0	0	0	0	0	0
2.47E+05	1.54E+00	9	0	0	0	0	0	0
2.54E+05	1.58E+00	8	0	0	0	0	0	0
2.61E+05	1.63E+00	11	0	0	0	0	0	0
2.68E+05	1.67E+00	8	0	0	0	0	0	0
2.75E+05	1.72E+00	7	0	0	0	0	0	0

2.83E+05	1.77E+00	9	0	0	0	0	0	0
2.91E+05	1.82E+00	3	0	0	0	0	0	0
2.99E+05	1.87E+00	6	0	0	0	0	0	0
3.07E+05	1.92E+00	8	0	0	0	0	0	0
3.16E+05	1.97E+00	8	0	0	0	0	0	0
3.25E+05	2.03E+00	4	0	0	0	0	0	0
3.34E+05	2.08E+00	5	0	0	0	0	0	0
3.43E+05	2.14E+00	1	0	0	0	0	0	0
3.52E+05	2.20E+00	7	0	0	0	0	0	0
3.62E+05	2.26E+00	4	0	0	0	0	0	0
3.72E+05	2.32E+00	4	0	0	0	0	0	0
3.82E+05	2.39E+00	7	0	0	0	0	0	0
3.93E+05	2.45E+00	4	0	0	0	0	0	0
4.04E+05	2.52E+00	3	0	0	0	0	0	0
4.15E+05	2.59E+00	6	0	0	0	0	0	0
4.27E+05	2.66E+00	6	0	0	0	0	0	0
4.39E+05	2.74E+00	5	0	0	0	0	0	0
4.51E+05	2.81E+00	5	0	0	0	0	0	0
4.63E+05	2.89E+00	1	0	0	0	0	0	0
4.76E+05	2.97E+00	2	0	0	0	0	0	0
4.89E+05	3.05E+00	4	0	0	0	0	0	0
5.03E+05	3.14E+00	2	0	0	0	0	0	0
5.17E+05	3.23E+00	3	0	0	0	0	0	0
5.31E+05	3.32E+00	5	0	0	0	0	0	0
5.46E+05	3.41E+00	2	0	0	0	0	0	0
5.61E+05	3.50E+00	1	0	0	0	0	0	0
5.77E+05	3.60E+00	5	0	0	0	0	0	0
5.93E+05	3.70E+00	2	0	0	0	0	0	0
6.09E+05	3.80E+00	2	0	0	0	0	0	0
6.26E+05	3.91E+00	3	0	0	0	0	0	0
6.44E+05	4.02E+00	3	0	0	0	0	0	0
6.61E+05	4.13E+00	2	0	0	0	0	0	0
6.80E+05	4.24E+00	3	0	0	0	0	0	0
6.99E+05	4.36E+00	5	0	0	0	0	0	0
7.18E+05	4.48E+00	2	0	0	0	0	0	0
7.38E+05	4.61E+00	4	0	0	0	0	0	0
7.59E+05	4.73E+00	0	0	0	0	0	0	0
7.80E+05	4.87E+00	2	0	0	0	0	0	0
8.01E+05	5.00E+00	2	0	0	0	0	0	0
8.23E+05	5.14E+00	4	0	0	0	0	0	0

8.46E+05	5.28E+00	2	0	0	0	0	0	0
8.70E+05	5.43E+00	3	0	0	0	0	0	0
8.94E+05	5.58E+00	4	0	0	0	0	0	0
9.19E+05	5.73E+00	3	0	0	0	0	0	0
9.44E+05	5.89E+00	3	0	0	0	0	0	0
9.71E+05	6.06E+00	2	0	0	0	0	0	0
9.97E+05	6.23E+00	4	0	0	0	0	0	0
1.03E+06	6.40E+00	3	0	0	0	0	0	0
1.05E+06	6.58E+00	5	0	0	0	0	0	0
1.08E+06	6.76E+00	2	0	0	0	0	0	0
1.11E+06	6.95E+00	3	0	0	0	0	0	0
1.14E+06	7.14E+00	0	0	0	0	0	0	0
1.18E+06	7.34E+00	1	0	0	0	0	0	0
1.21E+06	7.54E+00	2	0	0	0	0	0	0
1.24E+06	7.75E+00	1	0	0	0	0	0	0
1.28E+06	7.97E+00	2	0	0	0	0	0	0
1.31E+06	8.19E+00	3	0	0	0	0	0	0
1.35E+06	8.41E+00	1	0	0	0	0	0	0
1.39E+06	8.65E+00	2	0	0	0	0	0	0
1.42E+06	8.89E+00	1	0	0	0	0	0	0
1.46E+06	9.13E+00	1	0	0	0	0	0	0
1.50E+06	9.39E+00	3	0	0	0	0	0	0
1.55E+06	9.65E+00	1	0	0	0	0	0	0
1.59E+06	9.92E+00	5	0	0	0	0	0	0
1.63E+06	1.02E+01	2	0	0	0	0	0	0
1.68E+06	1.05E+01	3	0	0	0	0	0	0
1.72E+06	1.08E+01	2	0	0	0	0	0	0
1.77E+06	1.11E+01	0	0	0	0	0	0	0
1.82E+06	1.14E+01	0	0	0	0	0	0	0
1.87E+06	1.17E+01	0	0	0	0	0	0	0
1.92E+06	1.20E+01	2	0	0	0	0	0	0
1.98E+06	1.23E+01	1	0	0	0	0	0	0
2.03E+06	1.27E+01	1	0	0	0	0	0	0
2.09E+06	1.30E+01	0	0	0	0	0	0	0
2.15E+06	1.34E+01	1	0	0	0	0	0	0
2.21E+06	1.38E+01	0	0	0	0	0	0	0
2.27E+06	1.42E+01	0	0	0	0	0	0	0
2.33E+06	1.46E+01	0	0	0	0	0	0	0
2.40E+06	1.50E+01	1	0	0	0	0	0	0
2.46E+06	1.54E+01	0	0	0	0	0	0	0

2.53E+06	1.58E+01	0	0	0	0	0	0	0
2.60E+06	1.62E+01	0	0	0	0	0	0	0
2.67E+06	1.67E+01	0	0	0	0	0	0	0
2.75E+06	1.72E+01	1	0	0	0	0	0	0
2.82E+06	1.76E+01	0	0	0	0	0	0	0
2.90E+06	1.81E+01	0	0	0	0	0	0	0
2.98E+06	1.86E+01	0	0	0	0	0	0	0
3.07E+06	1.91E+01	0	0	0	0	0	0	0
3.15E+06	1.97E+01	0	0	0	0	0	0	0
3.24E+06	2.02E+01	1	0	0	0	0	0	0
3.33E+06	2.08E+01	1	0	0	0	0	0	0
3.42E+06	2.14E+01	0	0	0	0	0	0	0
3.52E+06	2.19E+01	1	0	0	0	0	0	0
3.61E+06	2.26E+01	0	0	0	0	0	0	0
3.71E+06	2.32E+01	0	0	0	0	0	0	0
3.82E+06	2.38E+01	1	0	0	0	0	0	0
3.92E+06	2.45E+01	0	0	0	0	0	0	0
4.03E+06	2.52E+01	0	0	0	0	0	0	0
4.14E+06	2.59E+01	0	0	0	0	0	0	0
4.26E+06	2.66E+01	0	0	0	0	0	0	0
4.38E+06	2.73E+01	0	0	0	0	0	0	0
4.50E+06	2.81E+01	0	0	0	0	0	0	0
4.62E+06	2.89E+01	0	0	0	0	0	0	0
4.75E+06	2.97E+01	2	0	0	0	0	0	0
4.88E+06	3.05E+01	0	0	0	0	0	0	0
5.02E+06	3.13E+01	0	0	0	0	0	0	0
5.16E+06	3.22E+01	0	0	0	0	0	0	0
5.30E+06	3.31E+01	1	0	0	0	0	0	0
5.45E+06	3.40E+01	0	0	0	0	0	0	0
5.60E+06	3.50E+01	0	0	0	0	0	0	0
5.76E+06	3.59E+01	0	0	0	0	0	0	0
5.92E+06	3.69E+01	0	0	0	0	0	0	0
6.08E+06	3.79E+01	0	0	0	0	0	0	0
6.25E+06	3.90E+01	0	0	0	0	0	0	0
6.42E+06	4.01E+01	1	0	0	0	0	0	0
6.60E+06	4.12E+01	0	0	0	0	0	0	0
6.78E+06	4.23E+01	0	0	0	0	0	0	0
6.97E+06	4.35E+01	0	0	0	0	0	0	0
7.17E+06	4.47E+01	0	0	0	0	0	0	0
7.36E+06	4.60E+01	0	0	0	0	0	0	0

7.57E+06	4.72E+01	0	0	0	0	0	0	0
7.78E+06	4.86E+01	0	0	0	0	0	0	0
8.00E+06	4.99E+01	0	0	0	0	0	0	0
8.22E+06	5.13E+01	0	0	0	0	0	0	0
8.45E+06	5.27E+01	0	0	0	0	0	0	0
8.68E+06	5.42E+01	0	0	0	0	0	0	0
8.92E+06	5.57E+01	1	0	0	0	0	0	0
9.17E+06	5.72E+01	1	0	0	0	0	0	0
9.42E+06	5.88E+01	0	0	0	0	0	0	0
9.68E+06	6.04E+01	0	0	0	0	0	0	0
9.95E+06	6.21E+01	0	0	0	0	0	0	0
1.02E+07	6.39E+01	2	0	0	0	0	0	0
1.05E+07	6.56E+01	0	0	0	0	0	0	0
1.08E+07	6.74E+01	0	0	0	0	0	0	0
1.11E+07	6.93E+01	0	0	0	0	0	0	0
1.14E+07	7.12E+01	0	0	0	0	0	0	0
1.17E+07	7.32E+01	0	0	0	0	0	0	0
1.21E+07	7.53E+01	1	0	0	0	0	0	0
1.24E+07	7.73E+01	0	0	0	0	0	0	0
1.27E+07	7.95E+01	0	0	0	0	0	0	0
1.31E+07	8.17E+01	0	0	0	0	0	0	0
1.35E+07	8.40E+01	0	0	0	0	0	0	0
1.38E+07	8.63E+01	0	0	0	0	0	0	0
1.42E+07	8.87E+01	0	0	0	0	0	0	0
1.46E+07	9.12E+01	0	0	0	0	0	0	0
1.50E+07	9.37E+01	0	0	0	0	0	0	0
1.54E+07	9.63E+01	1	0	0	0	0	0	0
1.59E+07	9.90E+01	0	0	0	0	0	0	0
1.63E+07	1.02E+02	0	0	0	0	0	0	0
1.67E+07	1.05E+02	0	0	0	0	0	0	0
1.72E+07	1.07E+02	0	0	0	0	0	0	0
1.77E+07	1.10E+02	0	0	0	0	0	0	0
1.82E+07	1.13E+02	1	0	0	0	0	0	0
1.87E+07	1.17E+02	0	0	0	0	0	0	0
1.92E+07	1.20E+02	0	0	0	0	0	0	0
1.97E+07	1.23E+02	1	0	0	0	0	0	0
2.03E+07	1.27E+02	0	0	0	0	0	0	0
2.09E+07	1.30E+02	0	0	0	0	0	0	0
2.14E+07	1.34E+02	0	0	0	0	0	0	0
2.20E+07	1.37E+02	0	0	0	0	0	0	0

2.26E+07	1.41E+02	0	0	0	0	0	0	0
2.33E+07	1.45E+02	1	0	0	0	0	0	0
2.39E+07	1.49E+02	0	0	0	0	0	0	0
2.46E+07	1.53E+02	0	0	0	0	0	0	0
2.53E+07	1.58E+02	0	0	0	0	0	0	0
2.60E+07	1.62E+02	0	0	0	0	0	0	0
2.67E+07	1.67E+02	0	0	0	0	0	0	0
2.74E+07	1.71E+02	0	0	0	0	0	0	0
2.82E+07	1.76E+02	0	0	0	0	0	0	0
2.90E+07	1.81E+02	0	0	0	0	0	0	0
2.98E+07	1.86E+02	0	0	0	0	0	0	0
3.06E+07	1.91E+02	0	0	0	0	0	0	0
3.14E+07	1.96E+02	0	0	0	0	0	0	0
3.23E+07	2.02E+02	0	0	0	0	0	0	0
3.32E+07	2.07E+02	0	0	0	0	0	0	0
3.41E+07	2.13E+02	0	0	0	0	0	0	0
3.51E+07	2.19E+02	0	0	0	0	0	0	0
3.61E+07	2.25E+02	0	0	0	0	0	0	0
3.71E+07	2.31E+02	0	0	0	0	0	0	0
3.81E+07	2.38E+02	0	0	0	0	0	0	0
3.91E+07	2.44E+02	0	0	0	0	0	0	0
4.02E+07	2.51E+02	0	0	0	0	0	0	0
4.14E+07	2.58E+02	0	0	0	0	0	0	0
4.25E+07	2.65E+02	0	0	0	0	0	0	0
4.37E+07	2.73E+02	0	0	0	0	0	0	0
4.49E+07	2.80E+02	0	0	0	0	0	0	0
4.61E+07	2.88E+02	0	0	0	0	0	0	0
4.74E+07	2.96E+02	0	0	0	0	0	0	0
4.87E+07	3.04E+02	0	0	0	0	0	0	0
5.01E+07	3.13E+02	0	0	0	0	0	0	0
5.15E+07	3.21E+02	0	0	0	0	0	0	0
5.29E+07	3.30E+02	0	0	0	0	0	0	0
5.44E+07	3.39E+02	0	0	0	0	0	0	0
5.59E+07	3.49E+02	0	0	0	0	0	0	0
5.74E+07	3.59E+02	0	0	0	0	0	0	0
5.90E+07	3.68E+02	0	0	0	0	0	0	0
6.07E+07	3.79E+02	0	0	0	0	0	0	0
6.24E+07	3.89E+02	0	0	0	0	0	0	0
6.41E+07	4.00E+02	0	0	0	0	0	0	0
6.59E+07	4.11E+02	0	0	0	0	0	0	0

6.77E+07	4.23E+02	0	0	0	0	0	0	0
6.96E+07	4.34E+02	0	0	0	0	0	0	0
7.15E+07	4.46E+02	0	0	0	0	0	0	0
7.35E+07	4.59E+02	0	0	0	0	0	0	0
7.55E+07	4.71E+02	0	0	0	0	0	0	0
7.76E+07	4.85E+02	0	0	0	0	0	0	0
7.98E+07	4.98E+02	0	0	0	0	0	0	0
8.20E+07	5.12E+02	0	0	0	0	0	0	0
8.43E+07	5.26E+02	0	0	0	0	0	0	0
8.66E+07	5.41E+02	0	0	0	0	0	0	0
8.90E+07	5.56E+02	0	0	0	0	0	0	0
9.15E+07	5.71E+02	0	0	0	0	0	0	0
9.40E+07	5.87E+02	0	0	0	0	0	0	0
9.66E+07	6.03E+02	0	0	0	0	0	0	0
9.93E+07	6.20E+02	0	0	0	0	0	0	0
1.02E+08	6.37E+02	0	0	0	0	0	0	0
1.05E+08	6.55E+02	0	0	0	0	0	0	0
1.08E+08	6.73E+02	0	0	0	0	0	0	0
1.11E+08	6.92E+02	0	0	0	0	0	0	0
1.14E+08	7.11E+02	0	0	0	0	0	0	0
1.17E+08	7.31E+02	0	0	0	0	0	0	0
1.20E+08	7.51E+02	0	0	0	0	0	0	0
1.24E+08	7.72E+02	0	0	0	0	0	0	0
1.27E+08	7.93E+02	0	0	0	0	0	0	0
1.31E+08	8.15E+02	1	0	0	0	0	0	0
1.34E+08	8.38E+02	0	0	0	0	0	0	0
1.38E+08	8.61E+02	0	0	0	0	0	0	0
1.42E+08	8.85E+02	0	0	0	0	0	0	0
1.46E+08	9.10E+02	0	0	0	0	0	0	0
1.50E+08	9.35E+02	0	0	0	0	0	0	0
1.54E+08	9.61E+02	0	0	0	0	0	0	0
1.58E+08	9.88E+02	0	0	0	0	0	0	0
1.63E+08	1.02E+03	0	0	0	0	0	0	0
1.67E+08	1.04E+03	0	0	0	0	0	0	0
1.72E+08	1.07E+03	0	0	0	0	0	0	0
1.77E+08	1.10E+03	0	0	0	0	0	0	0
1.81E+08	1.13E+03	0	0	0	0	0	0	0
1.86E+08	1.16E+03	0	0	0	0	0	0	0
1.92E+08	1.20E+03	0	0	0	0	0	0	0
1.97E+08	1.23E+03	0	0	0	0	0	0	0

2.02E+08	1.26E+03	0	0	0	0	0	0	0
2.08E+08	1.30E+03	0	0	0	0	0	0	0
2.14E+08	1.33E+03	0	0	0	0	0	0	0
2.20E+08	1.37E+03	0	0	0	0	0	0	0
2.26E+08	1.41E+03	0	0	0	0	0	0	0
2.32E+08	1.45E+03	0	0	0	0	0	0	0
2.39E+08	1.49E+03	0	0	0	0	0	0	0
2.45E+08	1.53E+03	0	0	0	0	0	0	0
2.52E+08	1.57E+03	0	0	0	0	0	0	0
2.59E+08	1.62E+03	0	0	0	0	0	0	0
2.66E+08	1.66E+03	0	0	0	0	0	0	0
2.74E+08	1.71E+03	0	0	0	0	0	0	0
2.81E+08	1.76E+03	0	0	0	0	0	0	0
2.89E+08	1.80E+03	0	0	0	0	0	0	0
2.97E+08	1.85E+03	0	0	0	0	0	0	0
3.05E+08	1.91E+03	0	0	0	0	0	0	0
3.14E+08	1.96E+03	0	0	0	0	0	0	0
3.23E+08	2.01E+03	0	0	0	0	0	0	0
3.31E+08	2.07E+03	0	0	0	0	0	0	0
3.41E+08	2.13E+03	0	0	0	0	0	0	0
3.50E+08	2.19E+03	0	0	0	0	0	0	0
3.60E+08	2.25E+03	0	0	0	0	0	0	0
3.70E+08	2.31E+03	0	0	0	0	0	0	0
3.80E+08	2.37E+03	0	0	0	0	0	0	0
3.91E+08	2.44E+03	0	0	0	0	0	0	0
4.01E+08	2.51E+03	0	0	0	0	0	0	0
4.13E+08	2.58E+03	0	0	0	0	0	0	0
4.24E+08	2.65E+03	0	0	0	0	0	0	0
4.36E+08	2.72E+03	0	0	0	0	0	0	0
4.48E+08	2.80E+03	0	0	0	0	0	0	0
4.60E+08	2.87E+03	0	0	0	0	0	0	0
4.73E+08	2.95E+03	0	0	0	0	0	0	0
4.86E+08	3.04E+03	0	0	0	0	0	0	0
5.00E+08	3.12E+03	0	0	0	0	0	0	0
5.14E+08	3.21E+03	0	0	0	0	0	0	0
5.28E+08	3.30E+03	0	0	0	0	0	0	0
5.43E+08	3.39E+03	0	0	0	0	0	0	0
5.58E+08	3.48E+03	0	0	0	0	0	0	0
5.73E+08	3.58E+03	0	0	0	0	0	0	0
5.89E+08	3.68E+03	1	0	0	0	0	0	0

6.05E+08	3.78E+03	0	0	0	0	0	0	0
# Targets hit ---->		456079	500000	500000	500000	500000	500000	500000

VITA

Bradley William Cox received his Bachelor of Science degree in mechanical engineering from The University of Texas at Austin in 2003. He entered the nuclear engineering program at Texas A&M University in August 2007 to begin his graduate studies and completed his Ph.D. in nuclear engineering in 2011. In 2008, he was awarded the National Space Biomedical Research Institute's doctoral fellowship in the field of space life sciences. His research interests focus on the health effects following exposure to the space radiation environment during long-term space missions.

Brad may be reached through the Department of Nuclear Engineering, Texas A&M University, College Station, TX 77843. His email is cox.bradw@gmail.com.